

UV-Vis, MCD, and Computational Studies of the
Electronic Structures of Core-Modified Porphyrins and
Phthalocyanines

by

Dustin Eric Nevenen

A Thesis submitted to the Faculty of Graduate Studies of

The University of Manitoba

in partial fulfilment of the requirements of the degree of

MASTER OF SCIENCE

Department of Chemistry

University of Manitoba

Winnipeg

Copyright © 2018 by Dustin Eric Nevenen

©Dustin Eric Nevonen 2018

Acknowledgements

I would like to thank my advisor, Dr. Victor Nemykin, for giving me the opportunity to study under his wise supervision. I would also like to thank my examining committee members: Dr. David Herbert (Department of Chemistry, University of Manitoba) and Dr. Johan van Lierop (Department of Physics and Astronomy, University of Manitoba) for their contributions in the evaluation of my thesis and its defense. Lastly, I would also like to thank all members of Nemykin lab, past and present, for providing a welcoming and professional work atmosphere.

Chapter four reproduced with permission from Majeed, S. A.; Ghazal, B.; Nevenon, D. E.; Goff, P. C.; Blank, D. A.; Nemykin, V. N.; Makhseed, S. *Inorg. Chem.* **2017**, *56*, 11640-11653. Copyright 2017 American Chemical Society.

Chapter five reproduced with permission from Nevenon, D. N.; Makarova, E. M.; King, A.; Lukyanets, E. A.; Nemykin, V. N. *J. Porphyrins. Pthalocyanines.* **2018**, (Submitted, Manuscript ID: jpp180193). Copyright 2018 Journal of Porphyrins and Phthalocyanines.

Abstract

The electronic structures and optical properties of a large variety of core-modified porphyrins, phthalocyanines (Pcs), naphthalocyanines (Ncs), and anthracocyanines (Acs) were investigated using UV-vis and magnetic circular dichroism (MCD) methods. In some cases, electrochemistry and spectroelectrochemistry were used to further probe the electronic structures of these compounds. In addition, Density Functional Theory (DFT), and Time Dependent DFT (TDDFT) approaches were also employed to correlate experimental properties with the electronic structures of the target compounds. Several types of ligands (bulky, electron-withdrawing, and electron-donating) were incorporated onto the respective macrocyclic peripheries to determine trends and the best macrocycle-substituent combination for its suitable application. The most prominent applications of the molecules studied in this thesis are photochemotherapeutics for photodynamic cancer therapy (PDT), light-harvesting, and optical materials. Speaking directly to their PDT and near infra-red (NIR) solar cell applications, the compounds that had the strongest and furthest red-shifted absorptions in the NIR region of the optical absorption spectrum were macrocycles with greatly extended π -systems (the Ncs and Acs) which also featured bulky, electron-donating ligands.

Table of Contents

• Acknowledgements.....	3
• Abstract.....	4
• Table of Contents.....	5
• Chapter 1: Porphyrins, Phthalocyanines, Naphthalocyanines, and Anthracocyanines: Motivation and Methods.....	7
○ Introduction.....	7
○ Instrumental Techniques.....	9
▪ UV-Vis Spectroscopy.....	9
▪ Magnetic Circular Dichroism Spectroscopy.....	11
▪ Electrochemistry.....	20
▪ Spectroelectrochemistry.....	21
○ Computational Calculations.....	22
• Chapter 2: Systematic Studies of the Electronic Structures and MCD Spectra of Synthetic Oxochlorins, Dioxobacteriochlorins, and Dioxoisobacteriochlorins.....	24
○ Summary.....	24
○ Introduction.....	25
○ Experimental Details.....	33
▪ Synthesis and Instrumentation.....	33
▪ Computational Aspects.....	34
○ Results and Discussion.....	34
▪ UV-Vis and MCD Spectra.....	34
○ Conclusions.....	48
• Chapter 3: Simultaneous Prediction of the Energies of Q_x/Q_y -Bands and Intramolecular Charge-Transfer Transitions in Benzoannulated and Non-Peripherally Substituted Metal- Free Phthalocyanines and Their Analogues: No TDDFT Silver Bullet Yet.....	49
○ Summary.....	49
○ Introduction.....	50
○ Experimental Details.....	55
▪ Materials and Instrumentation.....	55
▪ Computational Aspects.....	55
○ Results and Discussion.....	58
▪ UV-Vis and MCD Spectra of Expanded and α -Substituted Pcs and Their Analogues.....	58
▪ TDDFT and ZINDO/S Calculations.....	66
▪ General Trends in Predicted Q-Band Energies.....	81
▪ General Trends in Predicted Q-Band Splitting.....	82
▪ Description of Interligand Charge Transfer Bands for the α -Substituted Systems.....	85
○ Conclusions.....	87
• Chapter 4: Evaluation of the Intramolecular Charge-Transfer Properties in Solvatochromic and Electrochromic Zinc Octa(carbozoyl)phthalocyanines.....	89
○ Summary.....	89

○ Introduction.....	90
○ Experimental Details.....	92
▪ Synthesis and Instrumentation.....	92
▪ Computational Aspects.....	93
○ Results and Discussion.....	94
▪ UV-Vis and MCD Spectra.....	94
▪ Redox Properties of Phthalocyanines Zn and Zn-tBu.....	98
▪ DFT and TDDFT Calculations.....	101
○ Conclusions.....	104
● Chapter 5: Elucidation of the Electronic Structure of Water-Soluble Quaternized <i>meso</i> -Tetrakis(3-pyridyl)bacteriochlorin Derivatives by Experimental and Theoretical Methods.....	105
○ Summary.....	105
Introduction.....	106
○ Experimental Details.....	110
▪ Synthesis and Instrumentation.....	110
▪ Computational Aspects.....	110
○ Results and Discussion.....	111
○ Conclusions.....	116
● Chapter 6: Summary of the Electronic Structures of Core-Modified Porphyrins and Phthalocyanines.....	117
● Bibliography.....	122

Chapter 1: Electronic Structures of the Metal-free Porphyrins, Phthalocyanines, Naphthalocyanines, and Anthracocyanines:

Motivation and Methods

Introduction

Porphyrins, phthalocyanines (Pcs), naphthalocyanines (Ncs), and anthracocyanines (Acs) (Fig. 1) are interesting and closely related classes of molecules that have superior light absorbing properties, especially in the near infra-red (NIR) region of the optical absorption spectrum. Their unique spectral characteristics, with specific regard to their intense absorptions in the NIR region, make them the most useful platforms for photochemotherapeutics¹, antimicrobial and antibacterial phototherapy², and optical materials³. In terms of phototherapy, these strong NIR absorptions occur at wavelengths that can penetrate tissue and these photo-excitabile molecules rapidly produce singlet oxygen in biological systems which is toxic to nearby cells. The phototherapeutic application of porphyrins and phthalocyanines is not confined to *in-situ* methods as they are sometimes used as topical antimicrobial or antibacterial treatments where the production of singlet oxygen following photoexcitation is again involved. When used in optical materials, their strong, high and low energy optical absorptions can make for a useful layer in solar cells, boosting efficiency. In addition to their optical properties, the stability and facile redox activity, which commonly occurs over the π -conjugated framework of porphyrins, Pcs, Ncs, and Acs make these molecules potentially useful as electron-transfer or atom-transfer catalysts⁴.

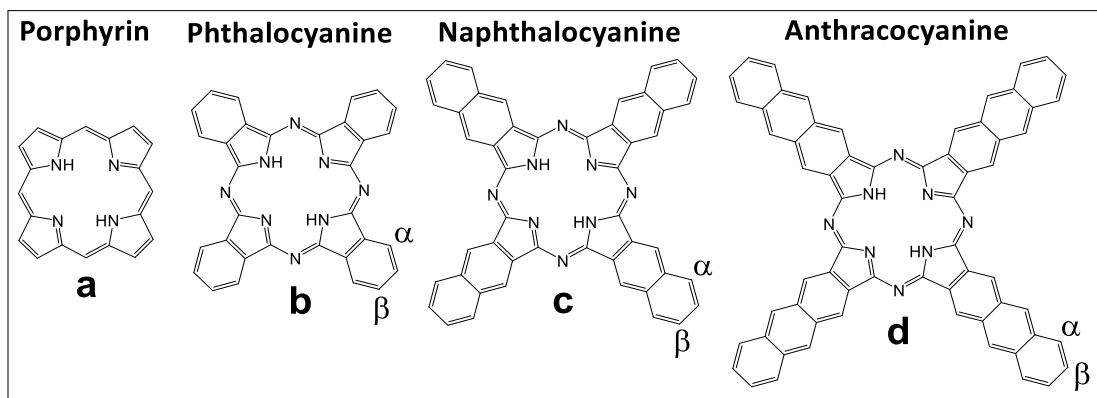


Figure 1. Structural diagram of the metal-free (a), (b), (c), and (d).

Shown in Fig. 1 are the structures of (a) unsubstituted metal-free porphyrin, (b) phthalocyanine, (c) naphthalocyanine, and (d) anthracocyanine. The similarities and differences of each of these molecules are clear to see as each contain the tetrapyrrolic macrocyclic core, consisting of two inner N-H bonds in its free-base form. Benzoannulation of the β -periphery of the pyrrole groups and incorporation of *meso*-nitrogen atoms in porphyrin results in a phthalocyanine and further benzoannulation of the exterior of Pc results in a naphthalocyanine, with one more benzoannulated extension resulting in an anthracocyanine. Addition of these benzene rings extends the conjugated π -system outwards and plays a significant role in shaping the electronic structures and optical properties of these macroheterocyclic molecules. In addition to extending the π -system of these molecules, substitution of the macrocyclic core by a variety of functional groups at non-peripheral α -positions and peripheral β -positions can enable a tunable approach when considering molecular design of porphyrin and phthalocyanine derivatives following the electronic structural analyses presented in later chapters of this thesis.

Historically, targeted molecule design of porphyrins, Pcs, Ncs, and Acs has typically been approached with a trial and error methodology. Only in recent years, theoretical approaches have been implemented in the design process in addition to numerical fitting and data manipulation to probe useful trends. In this body of work, a more systematic and modern theoretical approach is employed to analyze the electronic structures of core-modified porphyrins, Pcs, Ncs, and Acs to analyze how electron density changes throughout various states of excitation as well as where electron density is located just prior to and after electron promotion. Such studies on both unsubstituted and core-substituted molecular systems will provide this critical information so that the design process of future porphyrin, Pc, Nc, and Ac molecules can be more efficient since synthesis and isolation of complex molecules of these types can be very difficult, time-consuming, and expensive.

Instrumental Techniques

Analysis of the electronic structures of porphyrins, phthalocyanines, naphthalocyanines, and anthracocyanines was performed using a number of techniques. The variety of techniques such as UV-vis and magnetic circular dichroism (MCD) spectroscopies, DFT and TDDFT calculations, electrochemistry, and spectroelectrochemistry were used to probe the electronic structures of specific compounds in a multifaceted and comparative approach to prove that the experimental and computational methods employed agreed. A brief synopsis of the inner-workings of each technique used in this thesis are discussed below.

UV-Vis Spectroscopy

The characteristic spectral aspects of porphyrins, Pcs, Ncs, and Acs in regard to strong absorbances in the near infra-red (NIR) region of their optical absorption spectra are arguably the most important and studied feature of these molecule classes. The UV-vis spectrum is derived from the absorption of light by a molecule within a specified wavelength range. In a UV-vis spectrophotometer, specific wavelengths of light are directed through a solution of the sample under study, diluted with solvent. If the sample absorbs light at a certain wavelength, then some of the light of this wavelength won't reach the detector positioned behind the sample cell. This event is represented as an absorbance peak in the UV-vis spectrum. A schematic description is presented in Fig. 2.

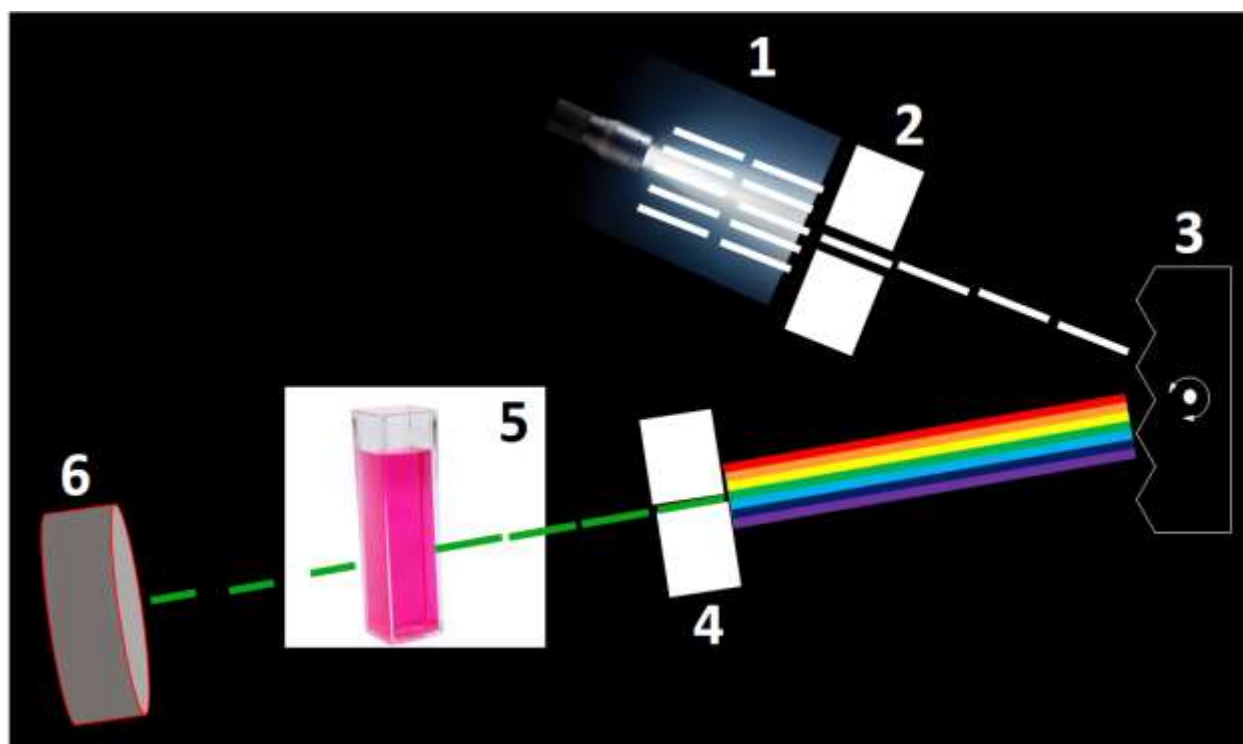


Figure 2. Figurative instrumental diagram of the UV-vis spectrophotometry process.

Shown in Fig. 2 is a figurative instrumental diagram of the UV-vis spectrophotometry process where each component is numbered for convenient reference. This spectrophotometric process starts at the light source (1) which is a xenon lamp that emits a bright, white light that contains scattered light which possesses all wavelengths of light within the visible spectrum. The entrance slit (2) consists of a monochromator which filters the wide wavelength range of light from the source and transmits a beam which contains a narrow band of light wavelengths. This beam of light then strikes the diffraction grating (3) which reflects the beam of white light into a beam of light containing all wavelengths of light within the optical window⁵. The diffraction grating rotates so that specific wavelengths of light reach the sample and comprise the UV-vis optical spectrum. This beam of coloured light then passes through an exit slit (4) which focuses and selects a narrow beam of light of a certain wavelength. When this beam is directed through a sample solution (5), some of the light is absorbed by the sample and some of the light passes through the sample solution. The light then reaches the detector (6) which measures two things. One aspect measured by the detector is transmittance, which is the amount of light that moves completely through the sample. The second aspect measured by the detector is absorbance, which is the amount of light absorbed by the sample.

Magnetic Circular Dichroism (MCD) Spectroscopy

The electronic structures of the diamagnetic porphyrins, phthalocyanines, naphthalocyanines, and anthracocyanines analyzed in this body of work all contain an overlapping π -framework which can result in complex and frequent electronic transitions upon

excitation. These electronic transitions are often overlapping and can appear as a single signal in other commonly employed relevant techniques such as UV-vis or electron paramagnetic resonance spectroscopy. To approach the prospect of elucidating complex electronic structures, magnetic circular dichroism is employed. MCD is a spectroscopic absorption technique that measures the differential absorption of left and right circularly polarized light by the sample in a magnetic field. A detailed instrumental and theoretical description follows.

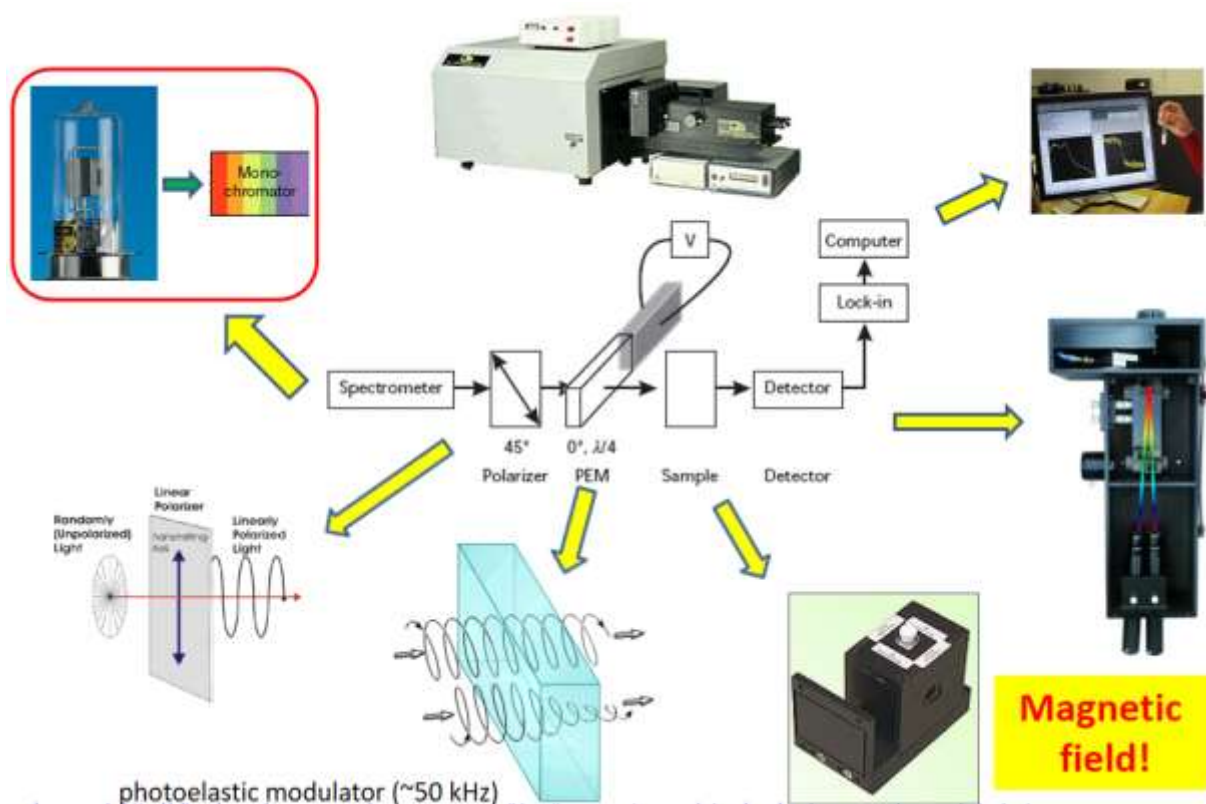


Figure 3. Instrumental overview of magnetic circular dichroism.

The instrumental overview⁶ of a typical magnetic circular dichroism apparatus is shown in Fig. 3. The process starts at the light source, a xenon lamp, which produces a broad array of wavelengths. This instrument could theoretically be modified to include a tungsten lamp which,

as a light source, could be used in part to detect NIR electronic transitions; however, for the purposes highlighted in this thesis, the xenon lamp provides a sufficient scanning range. This light then passes through a monochromator, which chops off portions of the beam to produce monochromatized light. This light then passes through a 45° polarizer which filters the randomly unpolarized light and only allows linearly polarized light to pass through. The light then passes through a photoelastic modulator which induces a 1/4 wavelength shift in the light, causing the photons in the light to move in a spiral in the right and left directions. The designation of left and right circularly polarized light occurs via pulses which convert between the two types on the timescale of about 50 kHz. The sample itself is diluted in solvent and placed into a quartz cuvette which itself is placed into a strong magnet which has holes on either side to allow the light to pass through. The magnet in the instrument used for this work has a field strength of 1.4 T. After passing through the sample, the light reaches the detector and the data is stored and processed in the computer using a specialized program.

In magnetic circular dichroism, the signals themselves are derived from the promotion of single electrons following photonic excitation. The perimeter model⁷⁻¹⁰ provides the best description of this idea which correlates chromophoric structures with their magnetic quantum numbers, optical absorption spectra, and molecular orbitals. A theoretical recreation of the perimeter model using benzene as an example is presented in Fig 4.

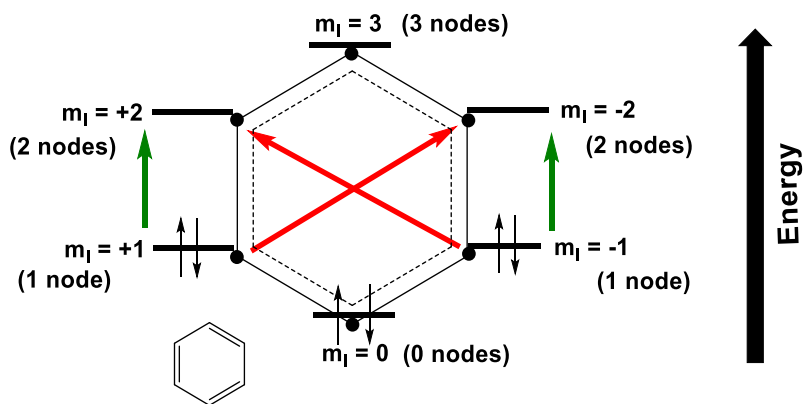
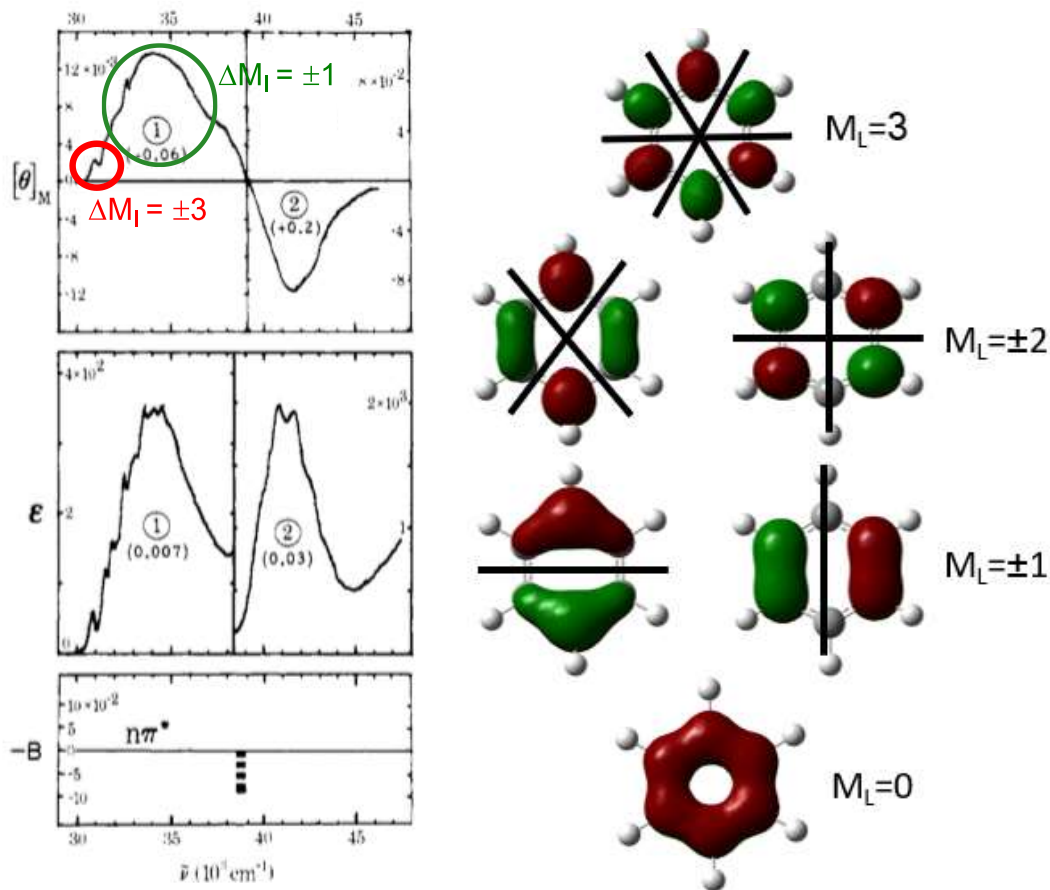


Figure 4. Perimeter model of benzene (lower) with absorption spectra¹¹ (upper left); (in absorption spectra: top = MCD, middle = UV-vis, bottom = calculated transitions) and molecular orbitals of benzene (upper right); figure partially adapted from reference 11.

Benzene contains six π -electrons, each of which correspond to a different magnetic quantum number (m_l) and these are represented by the six dots on the perimeter of the benzene ring in Fig. 4. In the ground state, each of the spins are paired for the $m_l = -1, 0,$ and $+1$ quantum numbers. When appropriately excited with light, these electrons are likely to undergo orbital promotion where one of the paired electrons will move to a higher energy molecular orbital (MO). The possible promotions are shown by the red and green arrows. In the case of the green arrows, these represent electron promotions where the $\Delta m_l = \pm 1$. These electronic transitions are allowed and are represented in the optical absorption spectrum as an intense peak. The red arrows show the other possibilities of electron promotion where the Δm_l value = ± 3 in the case of benzene. These possible transitions are forbidden and appear as discrete, weak signals in the optical absorption spectrum. The magnetic quantum numbers directly correlate with the number of nodal planes on the molecular orbitals of benzene as shown in the upper right of Fig. 4.

The most accurate and commonly used perimeter model descriptions for porphyrins are known as Gouterman's four-orbital model^{12,13} and Michl's perimeter model (Fig. 5).

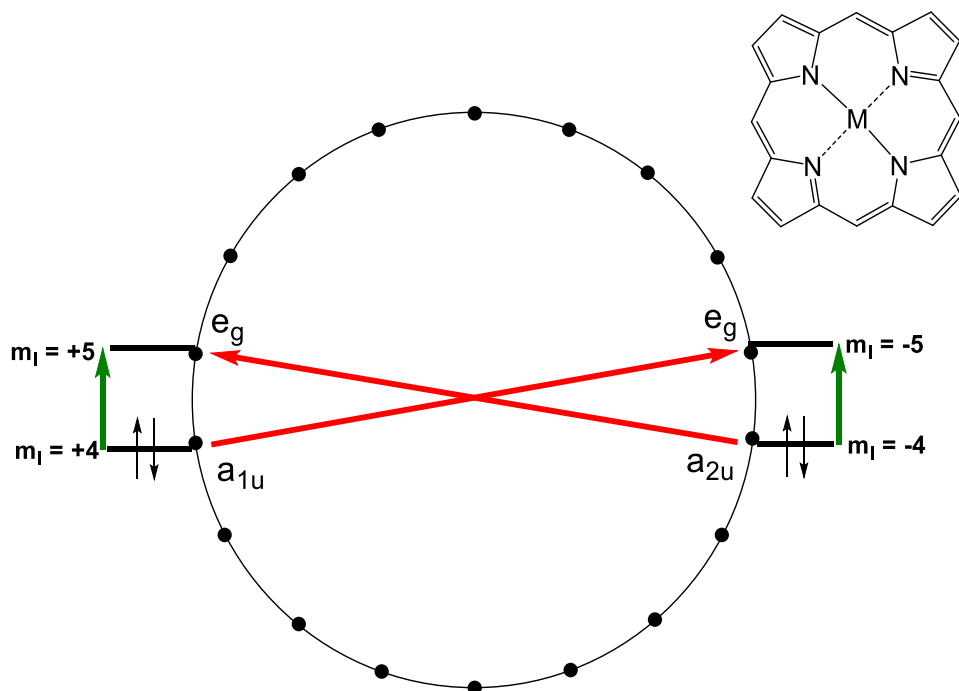


Figure 5. Gouterman's four-orbital perimeter model for porphyrins.

Fig. 5 above represents the focus of Gouterman's four orbital model, where each dot signifies one of the 18 π -orbitals in porphyrin. Essentially, there are only four possibilities for electron promotion within the frontier (Gouterman's) porphyrin electronic structure. These include two allowed transitions (green arrows) of $\Delta m_l = \pm 1$ and two forbidden transitions (red arrows) of $\Delta m_l = \pm 9$. These "a_{1u}", "a_{2u}", and "e_g" pair of energy levels are Gouterman's four orbitals and the transitions that occur between them comprise nearly all if not all of the signals that can be observed in the optical absorption spectra of porphyrinoids. These four orbitals are further described in Fig. 6.

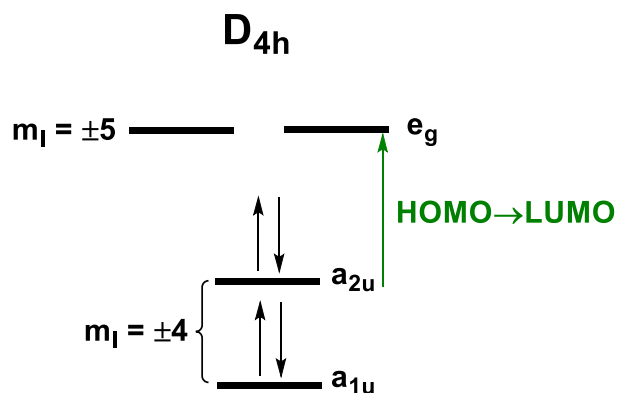


Figure 6. Identification of molecular orbitals involved in porphyrin electron promotion.

Shown in Fig. 6 is a description of the molecular orbitals involved in the promotion of electrons in porphyrin, which belongs to the D_{4h} point group. The $m_l = -4$ value corresponds to the a_{1u} orbital which represents the HOMO-1 and the $m_l = +4$ to the a_{2u} orbital, representing the HOMO. Finally, the $m_l = -5$ and $m_l = +5$ magnetic quantum numbers correspond to the degenerate pair of e_g orbitals which are the LUMO and LUMO+1 MOs, respectively.

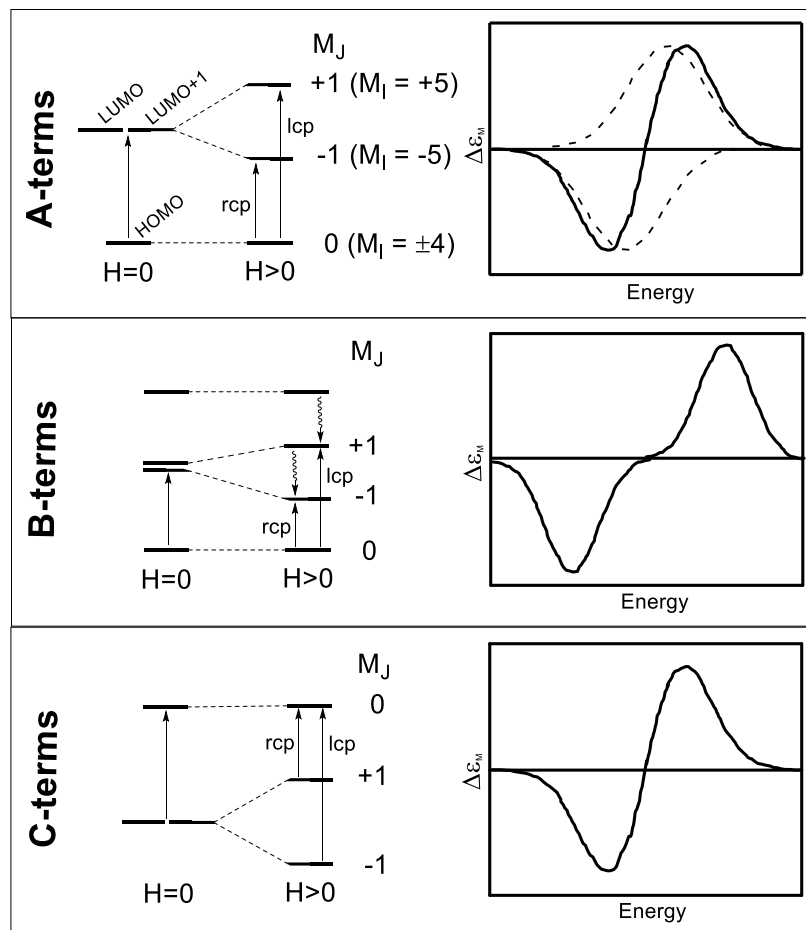


Figure 7. General conceptual summary of magnetic circular dichroism theory of porphyrinoids.

The general summary of magnetic circular dichroism theory when applied to porphyrins and their analogues is shown in a convenient diagram in Fig. 7. The signal produced by the MCD instrument has very characteristic peak shapes and sign sequences. Essentially, three types of signals are possible in MCD spectroscopy and these signal types have been classified into terms, specifically Faraday A, B, and C- terms.

Faraday *A*-terms are derived from degenerate excited states and are common in systems of D_{4h} symmetry such as some symmetrical, metallated porphyrins and phthalocyanines. These D_{4h} porphyrinoid systems feature degenerate LUMO and LUMO+1 energy levels which are split apart, in terms of energy, by the magnetic field. The right and left circularly polarized light have affinities for and interact with the lower and higher energy levels which are split apart to produce negative and positive signal components in the MCD spectrum, respectively (represented by the dashed lines)¹⁴. These negative and positive signal components are close in energy and when combined, they average together to form the “derivative” signal shape, which is a classical-looking Faraday *A*-term.

Faraday *B*-terms are derived from non-degenerate excited states which are typical for a lower degree of symmetry and are common in systems of D_{2h} symmetry such as symmetrical, free-base porphyrins and phthalocyanines. These porphyrinoids lack any kind of degeneracy of their Gouterman’s four orbitals. The magnetic field causes exaggerated splitting of the energy levels and as a result, their negative and positive components are further apart in terms of energy and won’t average together like the *A*-terms.

Faraday *C*-terms correlate and are solely associated with degenerate excited states in paramagnetic systems. They feature a degenerate ground state and can be elucidated with a temperature dependent experiment. At room temperature, they will appear similar to a Faraday *A*-term; however, upon decreasing the temperature, one of the lobes of the *A*-term will decrease and the other will increase, eventually appearing as a single peak of one sign. Since all of the systems studied in this thesis are diamagnetic, no *C*-terms were expected.

Electrochemistry

Electrochemistry is a very useful technique which measures reduction and oxidation potentials that are induced by applying a dynamic voltage to the sample system under study. When paired with other techniques such as spectroelectrochemistry and computational calculations, explanations of redox activity of the molecule under study can become even more substantial and well-defined. A brief description of an electrochemical apparatus follows.

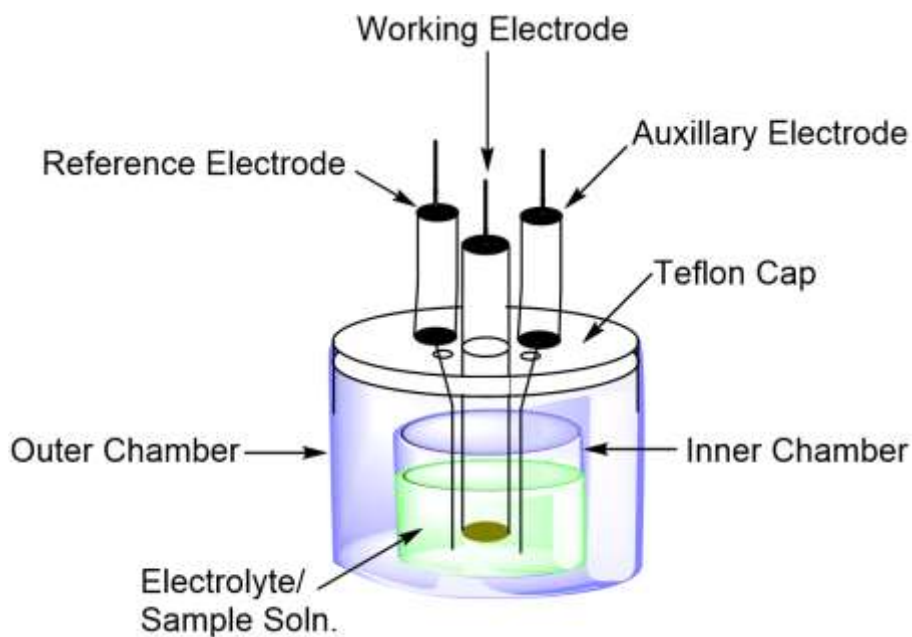


Figure 8. Electrochemical apparatus diagram.

Fig. 8 shows a classic electrochemical setup. The outer chamber is typically comprised of glass which provides a closed system in which no oxygen can enter. The glass inner chamber holds the liquid sample solution which contains a dissolved electrolyte in dry solvent. The sample is

dissolved into this solution and purged of oxygen using a pure inert gas such as nitrogen or argon. A Teflon cap is securely fixed to the outer chamber and Parafilm is used to cover any remaining holes in the Teflon cap such as the hole for the purge. Three electrodes are required for a successful electrochemistry experiment. The auxiliary electrode, also commonly referred to as the counter electrode, provides the source and/or sink for electrons in the system so this electrode transfers electrons from the external source throughout the sample solution¹⁵. The function of the reference electrode is to provide a constant potential which can be used as a reference for which to compare the other electrodes. Finally, the working electrode provides a location for the redox events to take place. Not pictured in Fig. 8 are the wires that attach to the electrodes. These wires feed to an electrochemical analyzer which converts the data into a readable spectral format.

Spectroelectrochemistry

Spectroelectrochemistry is often used as a comparative or supplementary technique which probes how many redox events are taking place in addition to indication of charge transfer type¹⁵. Spectroelectrochemistry pairs UV-vis spectroscopy and electrochemistry together to monitor how the UV-vis spectrum changes as a constant potential is applied and slowly increased (oxidation) or decreased (reduction) in a stepwise manner. The essential difference between the electrochemical and spectroelectrochemical setup is in the design of the sample cell. Instead of employing the inner and outer glass chambers, a quartz sample cell with a one-millimeter path length is used to hold the electrolyte and sample solution instead. A platinum wire mesh is used

as the working electrode as opposed to the typical cylindrical working electrode employed in electrochemical experiments. The three electrodes are added to the solution and the sample cell is placed into the spectrophotometer. A method called bulk electrolysis is used with the electrochemical analyzer and a constant potential is applied to the sample electrolyte solution. After an initial UV-vis spectrum is obtained, the potential is increased or decreased to generate new electroactive species. Such new oxidized or reduced species have different UV-vis spectra compared to the starting material.

Computational Methods

Determination of the type of computational calculations needed to employ the correct basis set and exchange correlation functional (ECF) will vary depending on the structure of the molecule under study. In this body of work, Density Functional Theory (DFT) and Time-Dependent DFT (TDDFT) calculations were performed to provide important relative data such as energies of frontier π -molecular orbitals as well as molecular orbital composition at several energy levels. For the porphyrins, phthalocyanines, naphthalocyanines, and anthracocyanines studied in these projects, several ECFs were used including B3LYP, CAM-B3LYP, TPSSh, BP86, LC-BP86, LC-wPBE, and PBE1PBE in addition to semi-empirical ZINDO calculations.

When considering porphyrinoid systems, reducing computational cost is important and can be accomplished by reducing large, non-essential functional groups such as long alkyl chains into smaller groups such as methyl. Also, using an appropriately sized basis set can reduce

computational cost so in all the calculations performed in this thesis, the medium-sized 6-31 G(d) basis set was employed. Larger basis sets that were tested resulted in very similar results, so an increased basis set size was needless. From previous work, it has been determined that overall, the modern hybrid exchange correlation functionals provide the best agreement between experiment and theory for the prediction of vertical excitation energies of porphyrinoid systems. In general, if the agreement between theory and experiment needs to be improved, the variable of import that should be considered first is the amount of Hartree-Fock (HF) exchange present in the exchange correlation functional. Increasing or decreasing the level of HF exchange is the most efficient method of tuning calculations.

The molecules themselves were created and optimized with Gaussian 09¹⁶ software. The single point data is used to generate molecular orbital images while the TDDFT output files are used to obtain the excited state energies and simulated UV-vis spectra. The typical for $\pi \rightarrow \pi^*$ transitions 0.1 – 0.15 eV bandwidth was used in all simulations of the TDDFT-predicted UV-vis spectra. The molecular orbital images and profile of the simulated UV-vis spectra were prepared and processed using the Gaussview software package¹⁷. In each case, the polarized continuum model (PCM) approach¹⁸ using chloroform as a solvent was employed to provide the most accurate results.

Chapter 2: Systematic Studies of the Electronic Structures and MCD Spectra of Synthetic Oxochlorins, Dioxobacteriochlorins, and Dioxoisobacteriochlorins

Summary

Several octaethyloxochlorins, octaethyldioxobacteriochlorins, and octaethyldioxoisobacteriochlorins were synthesized and isolated via β -oxidative modification of the peripheral pyrrolic fragments to include ketone and diketone moieties. The resulting hydroporphyrin macrocycles featured more intense and red-shifted NIR bands than their parent porphyrin. The bacteriochlorin molecule class has historically been targeted for photochemotherapeutic application in the field of photodynamic therapy (PDT) for the non-invasive treatment of cancer due to their superior resistance to melanin content interference and strong NIR absorption within the therapeutic window of tissue (600-940 nm). All studied chlorins, bacteriochlorins, and isobacteriochlorins had split Q_x - and Q_y -bands and a non-split or slightly split Soret band in the 395-425 nm spectral region. All key features present in the experimentally observed UV-vis and MCD spectra of the studied hydroporphyrins can be explained by Goutermann's four-orbital model and were predicted by electronic structure calculations. Specifically, DFT predicted a $\Delta\text{HOMO} > \Delta\text{LUMO}$ relationship for the majority of the compounds which agrees well with the observed -,+,+ experimental MCD sign sequence in the Vis-NIR spectral region. TDDFT also accurately predicted the experimentally observed split Soret band in

many compounds and splitting between the Q_y - and Q_x -bands. The bacteriochlorin compound **2.6** studied in this project exhibited a rare $\Delta\text{LUMO} \approx \Delta\text{HOMO}$ relationship.

Introduction

The unique and desirable electronic structures of naturally occurring porphyrinoids such as photosynthetic pigments have gained increasing interest in recent years. Their electronic structures enable these molecules to absorb light very strongly in the near infra-red (NIR) region of the optical absorption spectrum. Motivated by this natural phenomenon, the electronic structures of several substituted porphyrins have been prepared and analyzed. Substitution of a variety of β -substituents on the porphyrin periphery has a significant effect on the frontier π -molecular orbitals, and hence on the optical absorption spectrum, with the most desirable peripheral substitutions causing red-shifting of the λ_{max} band of longest wavelength. These strong NIR absorptions enable these tetrapyrroles to have important application in tumour imaging and as potential photochemotherapeutics for use in treatment of cancer via photodynamic therapy¹. Natural porphyrin analogues such as bacteriochlorins have been reported to have superior resistance to melanin content interference, further justifying the experimental motivations and approach in mimicking natural biomolecules.

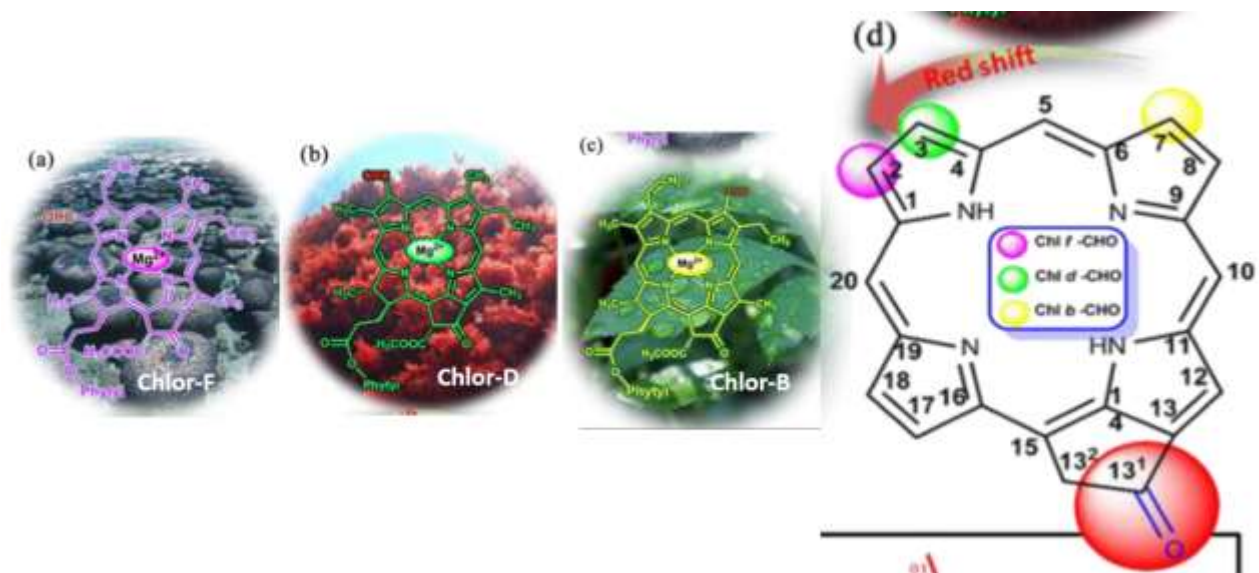


Figure 9. Chemical structures of a.) Chlorophyll *f*, b.) *d*, c.) *b*, and d.) orientation of β -formyl groups with respect to red-shift, e.) comparison of red-shift behavior of *cis* and *trans* porphyrinoid isomers (figure adapted from reference 19).

A motivational example of the importance of the molecule design featured in this project is shown in Fig. 9. In this figure are the structures of naturally occurring chlorophylls *f*, *d*, and *b*. The chlorophyll structures in Figs. 9a-c are very similar; however, the peripheral location of the formyl (CHO) group is varied with respect to the carbonyl (C=O) moiety. This variation has an effect on the Q_y band in the NIR region, causing increased red-shift behaviour as the formyl group is moved further from the carbonyl group in a counter-clockwise direction (Fig. 9d).

Fig. 10 shows the characteristic UV-vis spectrum for tetraphenylporphyrin (TPP). Since their macroheterocyclic core structures contain many of the same features, a very similar spectrum would be generated for porphyrin or even octaethylporphyrin (OEP). The absorption

bands that are visible in the UV-vis spectra of porphyrins correspond to electronic transitions between HOMO and HOMO-1 (HOMO is the highest occupied molecular orbital) and LUMO (lowest unoccupied molecular orbital) and LUMO+1. According to Gouterman's four-orbital model^{12,13}, in the case of metallated TPP, the HOMO and HOMO-1 involved in the transitions are a_{1u} and a_{2u} and the LUMO and LUMO+1 that are involved are two degenerate e_g orbitals, which is confirmed by computational methods. The UV-vis spectrum of the characteristic porphyrin (metal-free tetraphenylporphyrin) features the single, strongly absorbing B-band, known as the Soret band, followed by four bands [$Q_y(0-0)$, $Q_y(0-1)$, $Q_x(0-0)$, and $Q_x(0-1)$] of decreasing magnitude in descending energy. Due to the two-fold increase in symmetry going from a free-base to a metallated porphyrin, the number of Q-bands in the UV-vis spectrum are cut in half due to increased degeneracy.

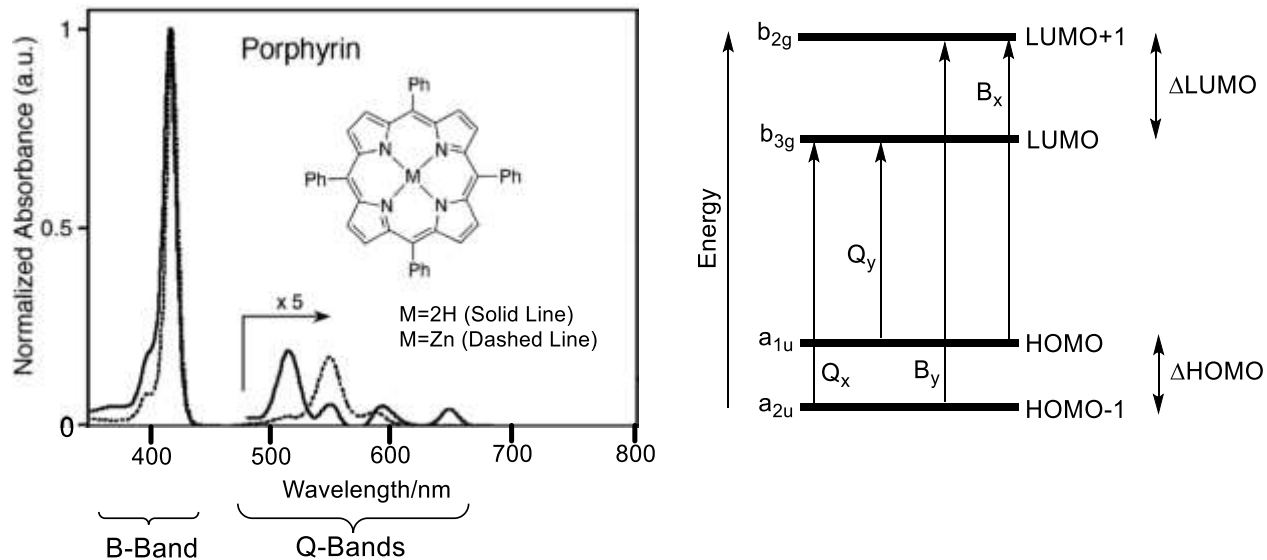


Figure 10. Characteristic UV-vis spectrum of TPP with corresponding peak assignment (all MO labels correspond to idealized D_{2h} geometry of the metal-free porphyrin; figure partially adapted from reference 20).

Fig. 10 defines the relationship between the frontier π -molecular orbitals and the absorption spectrum. According to Gouterman's four-orbital model^{12,13}, in the case of porphyrins, the molecular orbitals (MOs) that affect optical absorptions are confined to HOMO-1, HOMO, LUMO, and LUMO+1. Depending on which MO is excited and the degree of excitation, the UV-vis spectrum manifests itself. The Soret band (B-band) is almost always a mixing and overlap of excited states to produce the strongly absorbing peak at relatively high energy. The Soret band is derived from transitions between the two degenerate e_g orbitals in D_{4h} symmetry or a pair of b_{2g} and b_{3g} orbitals in D_{2h} symmetry.

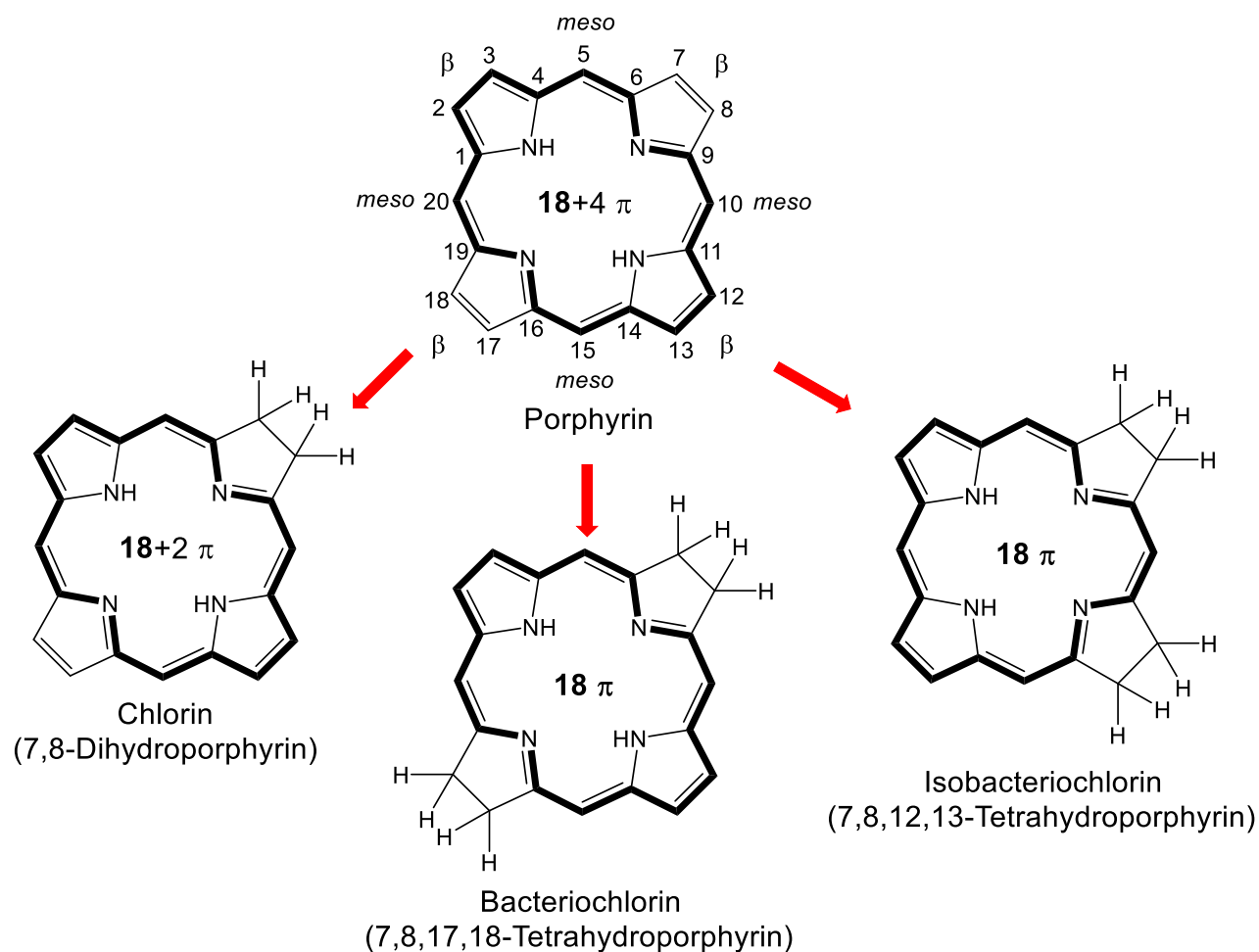


Figure 11. Structural overview of reduction of porphyrin to the hydrochlorins (figure reproduced from reference 20).

Fig. 11 shows the reduction of porphyrin to the hydrochlorins. In each of the macrocycles pictured above, all maintain 18 π -electrons in their closed conjugated aromatic systems. A reduction of one β - β' cross-conjugated pyrrolic double bond results in a chlorin. Reduction of two opposing peripheral pyrrolic double bonds results in a bacteriochlorin and reduction of two adjacent pyrrolic double bonds results in an isobacteriochlorin. As the degree

of reduction increases, the conformational flexibility also increases and this deviation from planarity leads to increased red-shift behaviour and decreased basicity²⁰.

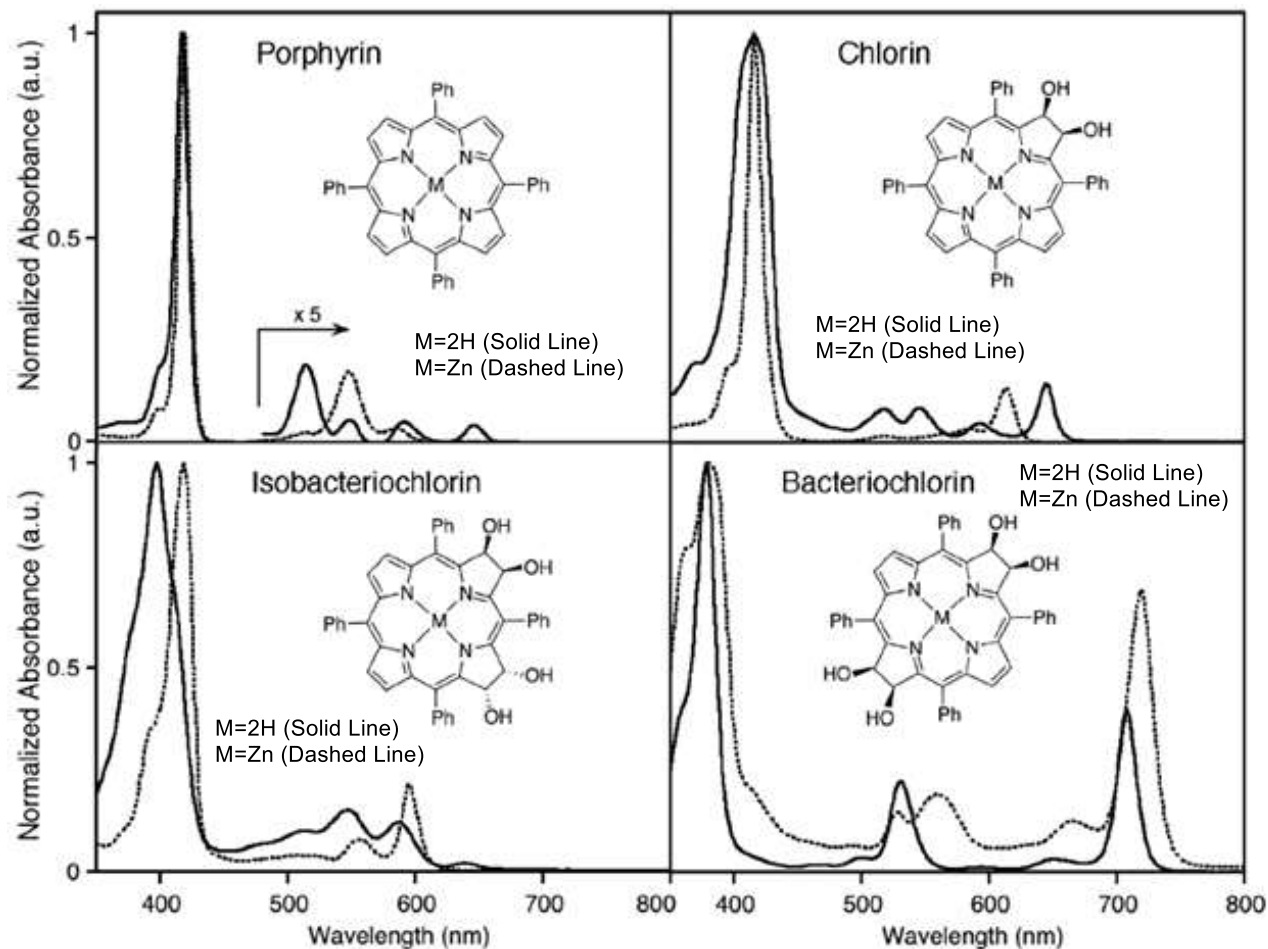


Figure 12. Characteristic UV-vis spectra of porphyrin and the hydroxymethyl-substituted porphyrins²⁰ (figure adapted from reference 20).

Fig. 12 shows characteristic UV-vis spectra of porphyrin and the hydroxymethyl-substituted porphyrins. This side-by-side comparison demonstrates typical and expected absorption peaks for unsubstituted porphyrin and the hydroxymethyl-substituted porphyrins. In reference to the previously discussed Fig. 10,

unsubstituted porphyrin has a strongly absorbing Soret band appearing at high energy followed by either two or four Q-bands of decreasing magnitude in descending energy depending on the symmetry, usually dictated by the composition of the porphyrin centre. The UV-vis spectra of isobacteriochlorins feature a hypsochromically shifted λ_{\max} band compared to chlorins. Bacteriochlorins have a distinct UV-vis spectrum due to their strongly absorbing Q-bands at NIR wavelengths. Of the three hydroporphyrins shown in Fig. 12, bacteriochlorins have the furthest red-shifted and strongest absorbing λ_{\max} band due to their small HOMO-LUMO gap, making them a most attractive platform for molecule design with the intent of PDT application.

The logic behind the motivation to use metal-free, synthetic chlorophylls such as bacteriochlorins as photochemotherapeutics lies in their strong absorption at NIR wavelengths and known resistance to melanin content interference. Essentially, tissue penetration depth versus wavelength is best modelled by exponential growth rather than a linear equation, whereas longer wavelength light can penetrate the skin much deeper than light of even slightly shorter wavelengths (Fig. 13).

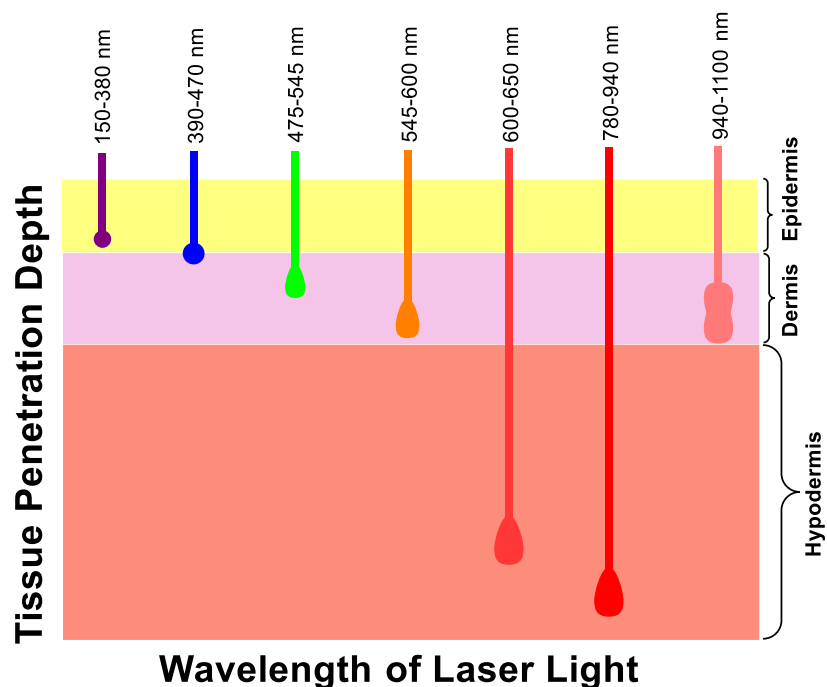


Figure 13. Relative tissue penetration depth for lasers of differing wavelength.

The typical incident intensity of a PDT light source is up to 200 mW/cm² for oncological application²¹. The current standards also require sufficient power to evenly irradiate up to 500 cm² of surface area. The light source itself can consist of either a laser or an incoherent light source which is matched to the absorption profile of the photosensitizer.

Researchers in this field are currently limited in their pursuit of molecules capable of absorbing increasingly long NIR wavelengths due to the absorption and scattering of light by melanin, known as melanin content interference, since longer wavelength light is absorbed and scattered more readily than that of shorter wavelength light. In early in-situ trials, bacteriochlorins were shown to resist melanin content absorption in appreciable magnitudes²⁰, further justifying the motivation to research this class of molecule intended for PDT application.

To replicate the electronic structures of naturally occurring porphyrinoids, seven hydroporphyrins of potential clinical importance have been synthesized (Fig. 14) and analyzed through computational (DFT and TDDFT) and experimental (UV-vis and MCD) spectroscopic methods.

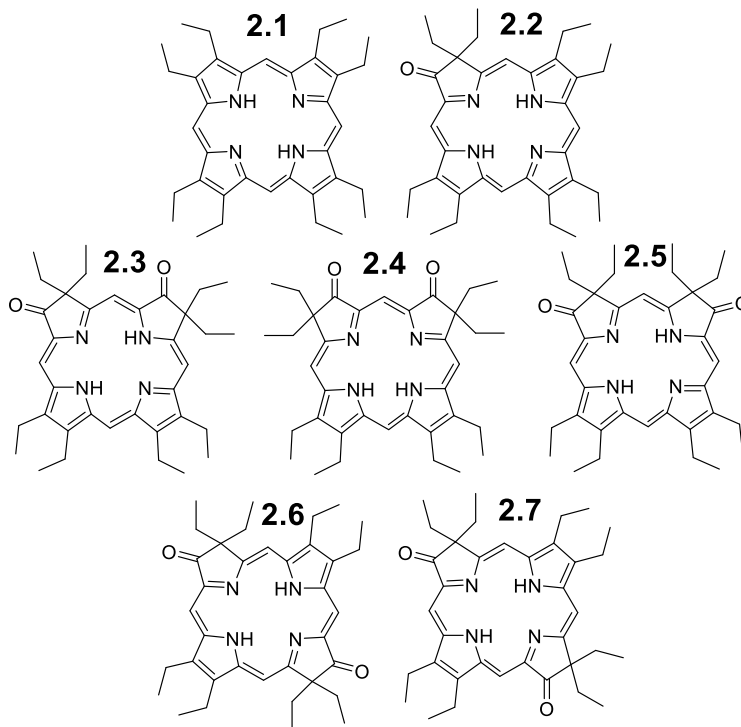


Figure 14. Structures of **2.1-2.7**.

Experimental Details

Synthesis and Instrumentation

Methylene chloride solvent was purchased from commercial sources and dried using distillation. Six octaethylxochlorin species (**2.2-2.7**) and the parent octaethylporphyrin (**2.1**)

were synthesized by the research group of Dr. Christian Brückner at University of Connecticut as described previously²².

UV-vis data were obtained with a Jasco V-670 spectrophotometer using DCM solvent. The MCD data were obtained with an OLIS DCM 17 CD spectropolarimeter using a permanent 1.4 T DeSa magnet. For each sample, two spectra were recorded: one using a parallel field and the other using an antiparallel field. The spectral intensities were expressed as molar ellipticity per τ .²³

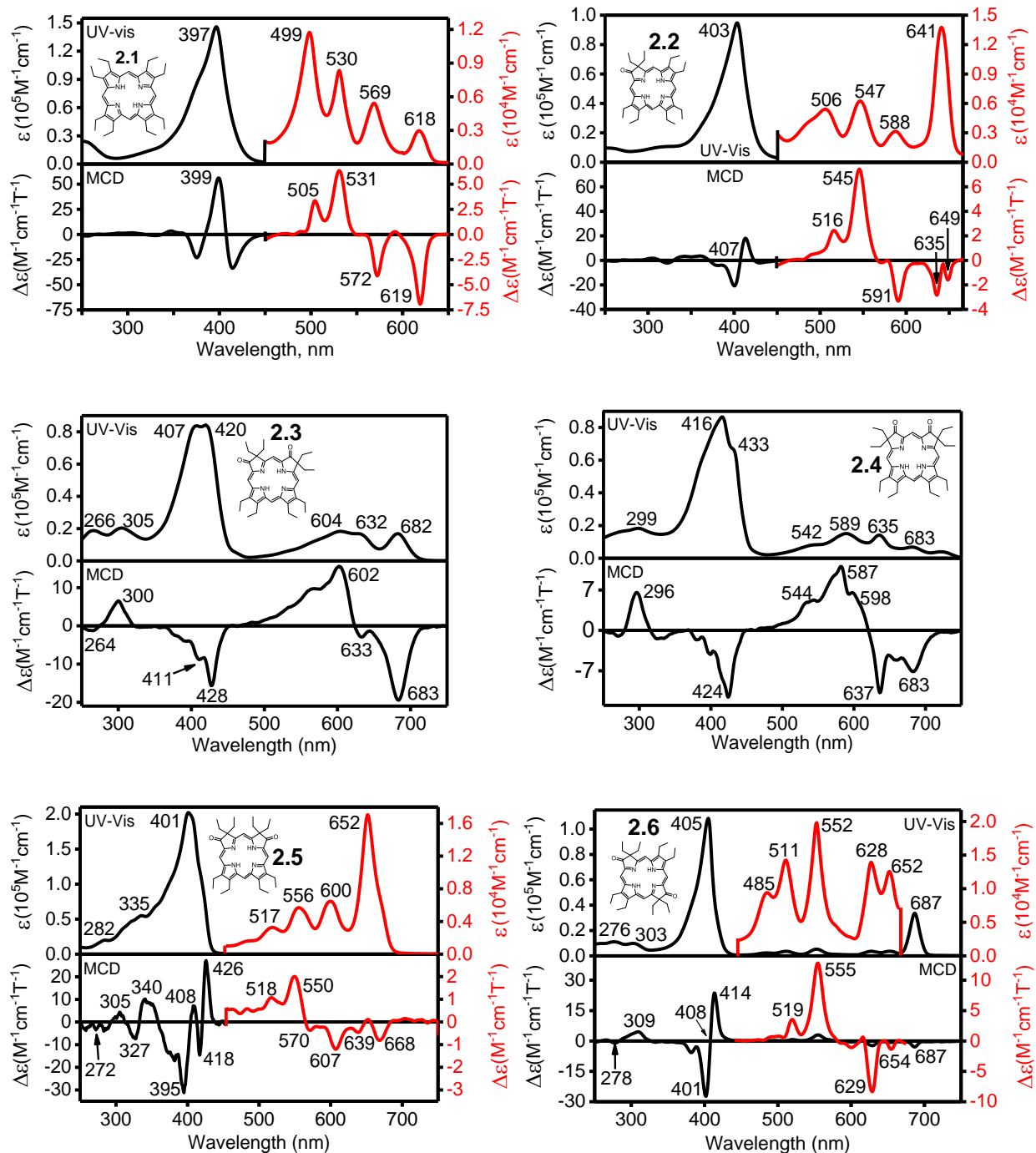
Computational Aspects

All DFT and TDDFT calculations were performed using Gaussian 09 software¹⁶. The starting geometries of **2.1-2.7** were optimized using the CAM-B3LYP exchange-correlation functional (10% of Hartree-Fock exchange).²⁴ The equilibrium geometries were confirmed with frequency calculations and more specifically, by the absence of imaginary frequencies. Modeling of all atoms was performed using the 6-31G(d) basis set¹⁸. For the TDDFT calculations, the solvent effects were calculated using the PCM approach¹⁸ with DCM as a solvent. The QMForge²⁵ program was used to compile orbital contributions from single-point calculations.

Results and Discussion

UV-Vis and MCD Spectra

The experimental UV-vis and MCD spectra for **2.1-2.7** are shown in Fig. 15.



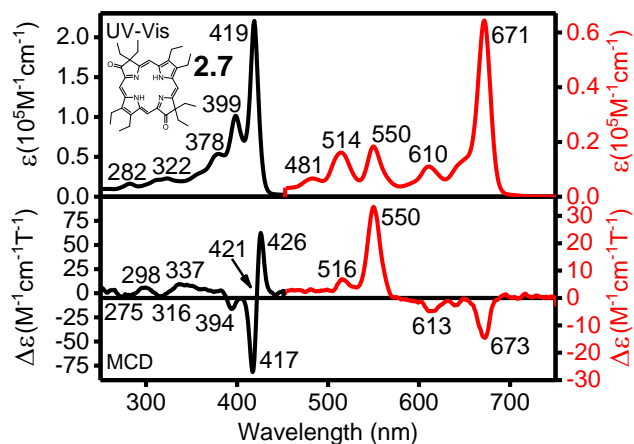


Figure 15. Experimental UV-vis (top) and MCD (bottom) spectra of **2.1-2.7**.

The absorption spectrum of oxochlorin **2.2** shows a shifted Q_y -band from 618 nm in **2.1** to 641 nm with a noticeable increase in the magnitude of intensity which corresponds to the negative MCD signals present at 635 and 649 nm. The Q_x -band of **2.2** is also red-shifted to 547 nm compared to the Q_x -band in OEP which occurs at 530 nm. This Q_x -band of **2.2** corresponds to an intense, positive MCD signal which is centred at 545 nm. Oxochlorin **2.2** possesses a Soret band at 403 nm which corresponds to a pseudo MCD A-term which is centred at 407 nm. Compared to normal porphyrin compounds, this pseudo MCD A-term has a reversed (positive to negative with increasing energy) shape.

The experimental UV-vis and MCD spectra of the dioxoisobacteriochlorins **2.3-2.5** can be grouped into two categories. The first category is **2.5** which possesses a strong Q_y -band present at 652 nm and corresponds to a negative MCD signal centred at 668 nm. This compound has a Q_x -band at 556 nm which corresponds to a positive MCD signal at 550 nm. The Q-band spectral region in **2.5** is comprised of five well-resolved bands present between 450 and 660 nm. Due to

their spectral similarities, the second category to discuss is **2.3** and **2.4**. In the case of isobacteriochlorins **2.3** and **2.4**, the Q_y-band observed at 683 nm is dramatically shifted in both compounds and overall, the Q-band region is not easily defined. The Q_y-band of **2.3** and **2.4** corresponds to a broad and negative MCD signal centred at 683 nm. The Soret band of **2.3** and **2.4** is much broader which is unlike the case of **2.5** and corresponds to a negative set of MCD signals between 400 and 430 nm. The Soret band of **2.5** is much narrower and corresponds to many negative and positive MCD signals present between 400 and 430 nm.

The dioxobacteriochlorins **2.6** and **2.7** possess the lowest energy Q_y bands which were observed at 687 nm for **2.6** and 671 nm for **2.7**. Both of these Q_y bands correspond to negative MCD signals centred at 687 nm for **2.6** and 673 nm for **2.7**. The experimentally observed Q_x bands in dioxobacteriochlorins **2.6** and **2.7** are observed at 552 and 550 nm, respectively and correspond to MCD signals centred at those same wavelengths. The intense Q_y band dominates the Q-band region of **2.6** and **2.7**. In dioxobacteriochlorin **2.6**, the Soret band observed at 405 nm corresponds to a reversed MCD pseudo A-term which is centred at 408 nm while in the case of **2.7**, three clear transitions at 378, 399, and 419 nm were observed in the Soret band region which correspond to a reversed MCD pseudo A-term which is centred at 419 nm.

No clear trends were observed in the energy differences between the Q_x- and Q_y-bands (the lowest energy positive and negative MCD signals) of **2.2-2.7** and this energy difference varied from 1970 to 3462 cm⁻¹, an example of which is the energy variation from 1970 and 3311 cm⁻¹ in **2.2-2.5**. It was clearly observed from the MCD spectra of **2.2-2.7** that their Q_x-bands all correspond to positive MCD signals while their first, lowest energy MCD signal always had

negative sign bands. These designations are quite common for tetra-*meso* aryl and octa-alkyl porphyrins and indicates that $\Delta\text{HOMO} > \Delta\text{LUMO}$ ^{7,26} (ΔHOMO is the difference in energy between the “a_{1u}” and “a_{2u}” Goutermann’s orbitals and ΔLUMO is the difference in energy between the “e_g” pair of Goutermann’s orbitals)^{12,13}. This MCD signal sequence of compounds **2.2-2.7** was similar to that of reduced porphyrins which originate from the OEP core^{20,27-38}; however, the observed $\Delta\text{HOMO} > \Delta\text{LUMO}$ relationship is unusual relative to chlorins, isobacteriochlorins, and bacteriochlorins reported earlier in which a reversed energy order was observed and corresponds to a positive MCD signal at lower energy and a negative MCD signal at higher energy¹⁹.

The coexistence of no less than two N-H tautomers which have different spectroscopic features was indicated via literature analysis of isobacteriochlorin isomers²⁰. Tautomers **2.3-2.5ac** possess a pyrrolic N-H hydrogen with another N-H hydrogen on the opposing pyrrole-modified macrocycle while tautomers **2.3-2.5ad** contain two N-H hydrogens on adjacent pyrrolic fragments which oppose the peripherally-modified pyrrole rings. A large 6-311+G(d,p) basis set was employed to estimate the difference in energy between the possible N-H tautomers of **2.3-2.5** (Table 1).

Table 1. Energy differences between tautomers of **2.3-2.5** as predicted by DFT.

<i>Tautomer</i>	<i>$\Delta\text{Energy}/\text{cm}^{-1}$</i>	<i>Boltzmann Distribution at 298K</i>
2.3ac	0	61%
2.3ad	135	32%
2.3bd	445	7%
2.4ad	0	94%
2.4ac	571	6%
2.5ac	0	97%
2.5ad	743	3%

To assist in the explanation of the MCD result, a set of DFT and TDDFT calculations were performed. In the cases of **2.2**, **2.6**, and **2.7**, only one single atropisomer which has two N-H hydrogens on opposing pyrrole rings were determined to be energetically possible; however, in the case of the dioxoisobacteriochlorins **2.3-2.5** and due to their close energies, several N-H tautomers were calculated. These energetically favorable tautomers are shown in Fig. 16 while the energetically unlikely tautomers (**2.3bc**, **2.3cd**, **2.3ab**, **2.4bc**, **2.4ab**, **2.5bc**, and **2.5ab**) weren't considered.

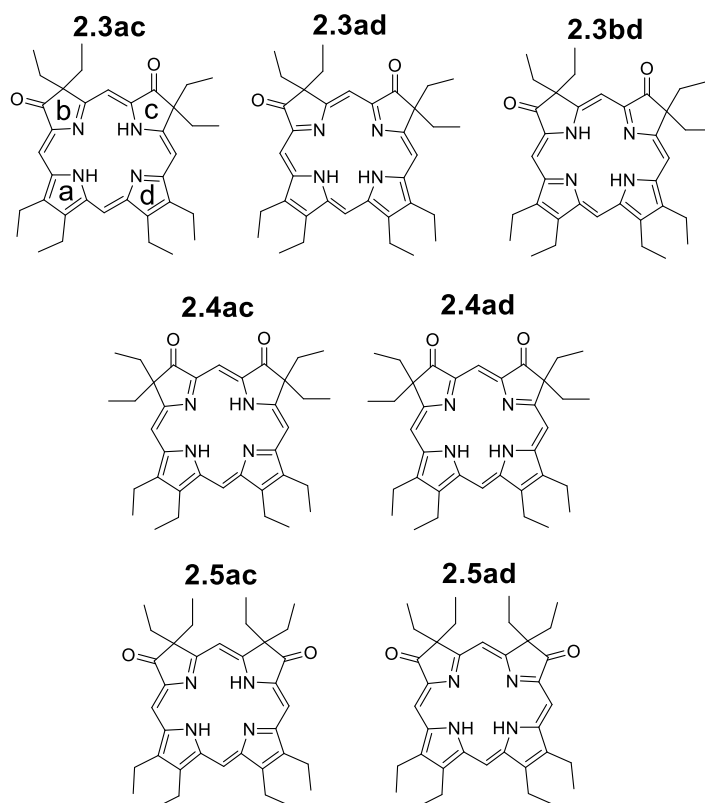


Figure 16. Structures of dioxoisobacteriochlorin tautomers **2.3-2.5** with similar DFT-predicted energies.

In the case of dioxoisobacteriochlorin **2.5**, the tautomers “**ac**” and “**ad**” only contribute to spectroscopic signatures with a 97:3% ratio of **ac:ad**, as predicted by the DFT calculations. It was predicted by DFT that for dioxoisobacteriochlorin **2.4**, the same two tautomers should contribute to its UV-vis and MCD spectra, except the “**ad**” tautomer will be much more dominant over the “**ac**” tautomer with a 94:6% ratio of **ad:ac**. The differences in the absorption spectra of **2.4** and **2.5** can be explained by these DFT predictions since the “**ac**” N-H tautomer of dioxoisobacteriochlorin **2.5** corresponds to the Q_y band at 652 nm while the absorption spectra of **2.4** is dominated by the “**ad**” tautomer with the Q_y band occurring at 683 nm. Lastly, the “**ac**”, “**ad**”, and “**bd**” N-H tautomers of dioxoisobacteriochlorin **2.3** contribute to the UV-vis and MCD spectra with an **ac:ad:bd** ratio of 61:32:7%. Due to this N-H tautomer ratio, it is expected that the **2.3ad** tautomer should make the largest contribution to the observed 682 nm band which is similar to the case of **2.4** where a 683 nm band was observed.

Shown in Fig. 17 is the DFT-predicted energy level diagram for **2.1-2.7** followed by the frontier molecular orbital images pictured in Fig. 18.

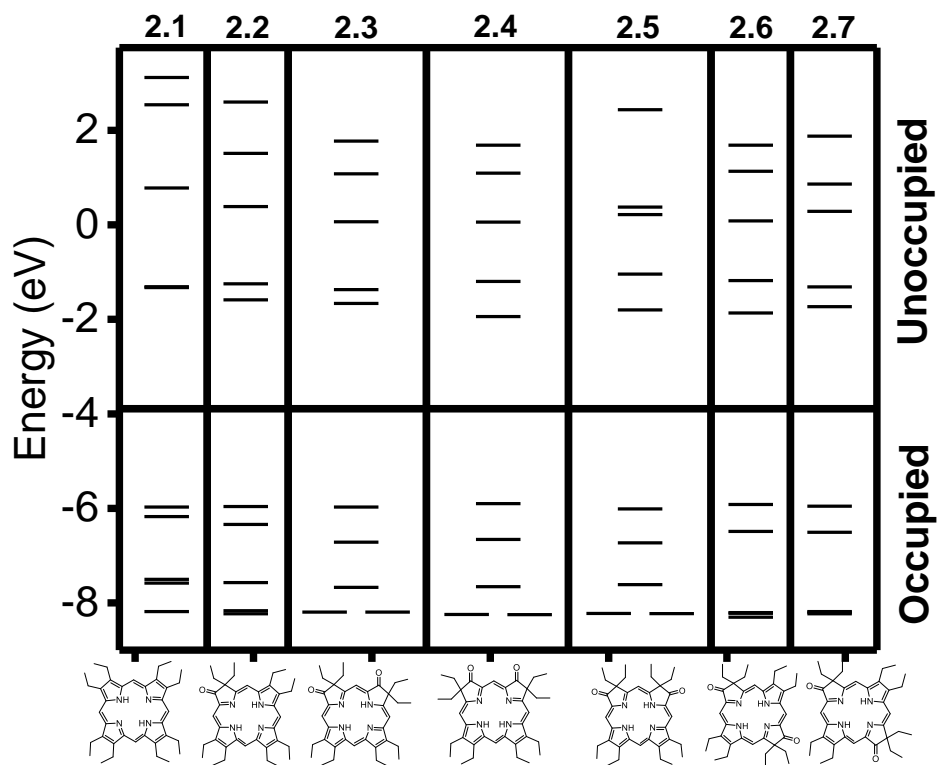


Figure 17. Energy level diagram for **2.1** and the most stable tautomers of compounds **2.2-2.7** as predicted by DFT.

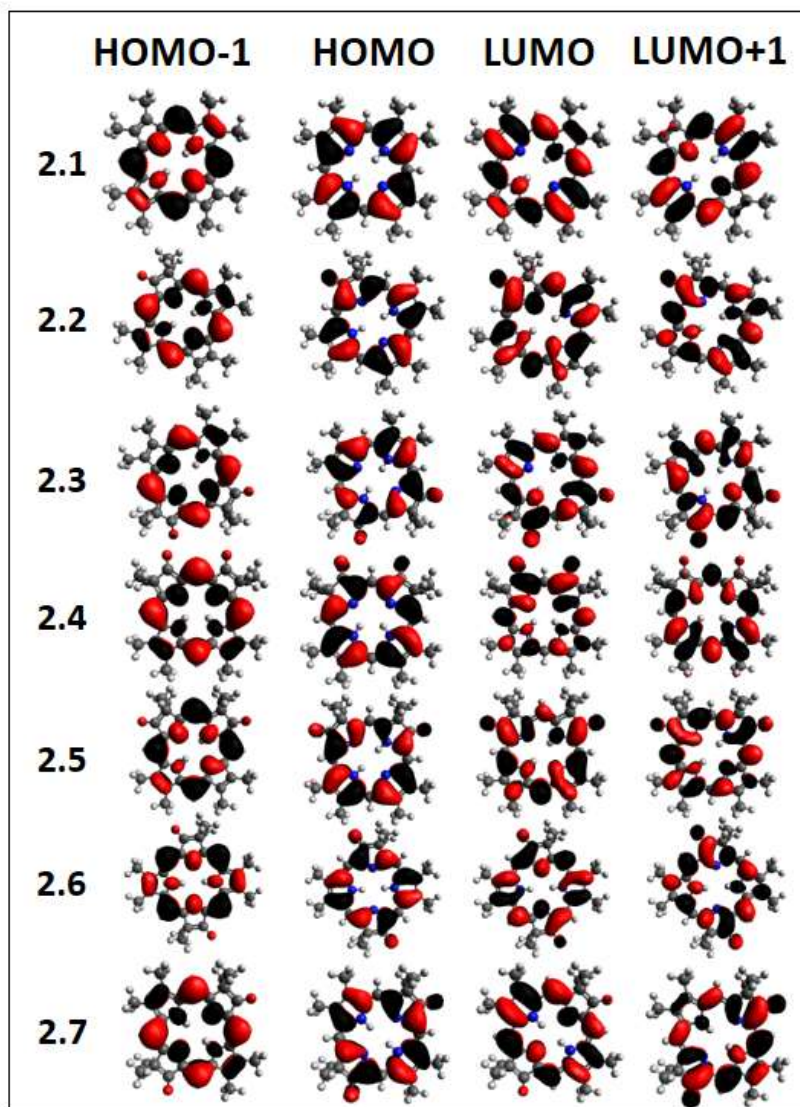
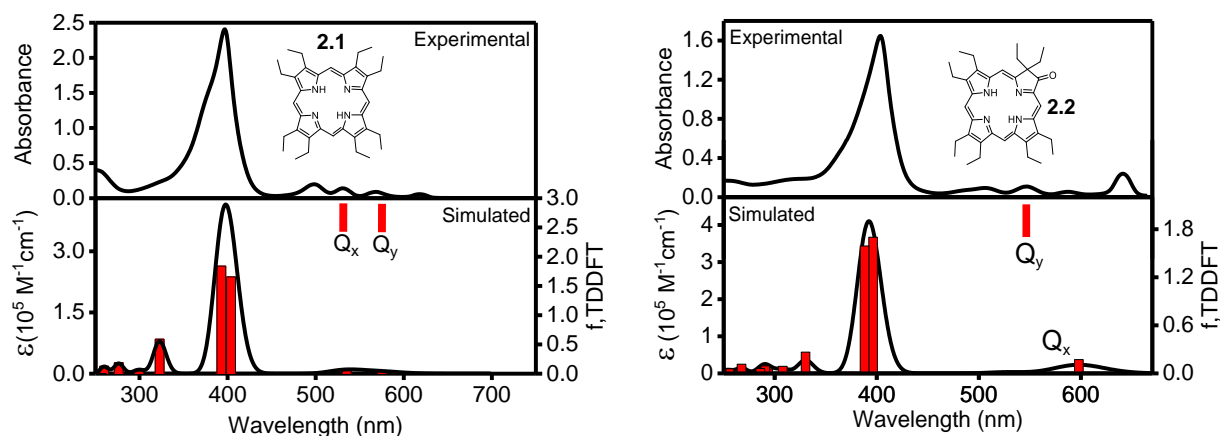


Figure 18. Frontier molecular orbitals for **2.1-2.7** as predicted by DFT.

In D_{4h} point group notation, the HOMO of **2.2-2.7** possesses Goutermann's " a_{1u} " character and the HOMO-1 is comprised of Goutermann's " a_{2u} " character which was similar to the case of the free-base, parent **2.1**. Goutermann's " e " pair of molecular orbitals³⁹ best describes the LUMO and LUMO+1 in all cases. According to the perimeter model⁷⁻¹⁰, it's

expected that the negative to positive (in ascending energy) MCD sign sequence corresponds to a $\Delta\text{HOMO} > \Delta\text{LUMO}$ relationship. The experimental MCD spectra of **2.1-2.7** correlate well with the DFT-predicted $\Delta\text{HOMO} > \Delta\text{LUMO}$ relationship, with the exception of compounds **2.4bc**, **2.5ad**, and **2.6**. Regarding compounds **2.4bc** and **2.5ad**, the DFT-predicted $\Delta\text{HOMO} < \Delta\text{LUMO}$ relationship indicates an expected reversal in MCD sign sequence within the Q-band region (for example, positive to negative MCD *B*-terms with increasing energy); however, a negligibly small contribution of **2.4bc** and 3% contribution from **2.5ad** N-H tautomers that were predicted by DFT calculations would not change their MCD spectra. In regard to dioxobacteriochlorin **2.6**, the DFT-predicted ΔHOMO (0.63 eV) and ΔLUMO (0.64 eV) are nearly identical; thus, for this specific compound, the prediction of the magnitudes of the MCD signals is difficult within the framework of the perimeter model.

To correlate the DFT-predicted electronic structures with experimental UV-vis and MCD spectra of **2.1-2.7**, TDDFT calculations were employed with the spectra shown in Fig. 19.



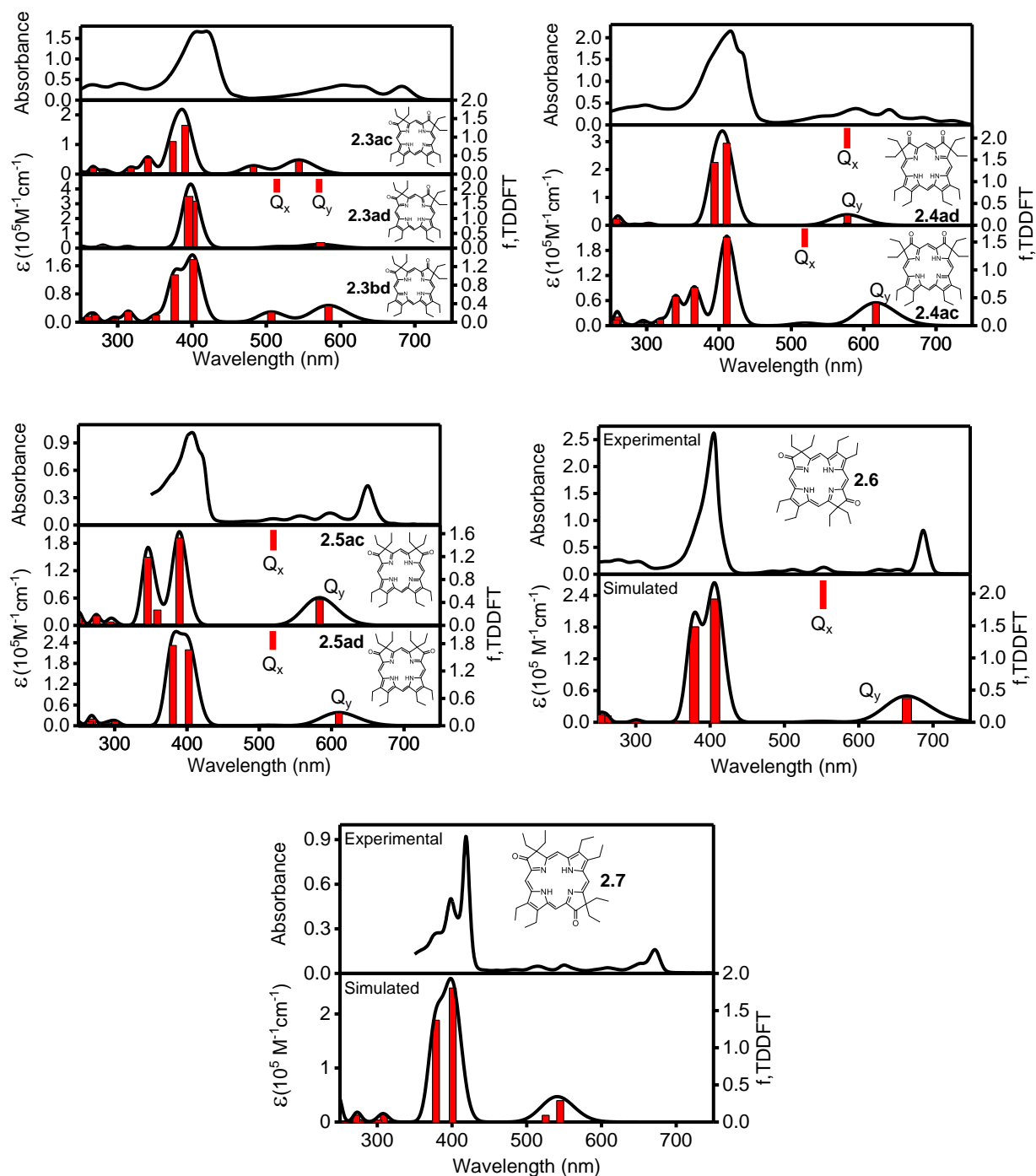


Figure 19. Experimental (top) and TDDFT-predicted (bottom) UV-vis spectra of **2.1-2.7**.

Goutermann's four-orbital model provides a good correlation with the TDDFT-predicted UV-vis spectrum of the parent **2.1**. The Q-band region is comprised of single-electron excitations starting at the HOMO and HOMO-1 and promoting to the almost degenerate LUMO and LUMO+1. Furthermore, Goutermann's four-orbital model nearly solely describes the energies and intensities of the Soret band region. Oxochlorin **2.2** shows a similar situation with TDDFT-predicted first excited state domination by way of HOMO to LUMO single electron excitation. As opposed to **2.1**, the second excited state within the Q-band region of **2.2** was predicted to be comprised of nearly equal HOMO-1 to LUMO and HOMO to LUMO+1 single electron excitations (Table 2).

Table 2. UV-vis spectral Q-band region single electron excitations of **2.1-2.7**.

<i>Compound</i>	<i>State</i>	<i>Energy/nm(cm⁻¹)</i>	<i>Excitations and Expansion Coefficients</i>
2.1	1	575(17388)	H-1→L -0.44819, H→L+1 0.54877
2.1	2	535(18686)	H-1→L+1 0.39863, H→L 0.58365
2.1	3	404(24759)	H-3→L 0.16273, H-1→L 0.52956, H→L+1 0.44239
2.1	4	393(25452)	H-1→L+1 0.58578, H→L -0.40241
2.2	1	586(17076)	H-1→L+1 0.30916, H→L 0.62571
2.2	2	525(19046)	H-1→L -0.45161, H→L 0.10808, H→L+1 0.52972
2.2	3	401(24926)	H-1→L 0.52116, H-1→L+1 0.10773, H→L+1 0.45324
2.2	4	345(25681)	H-1→L -0.11466, H-1→L+1 0.61575, H→L -0.30434
2.3ac	1	544(18385)	H-1→L+1 0.20841, H→L 0.64121, H→L+1 -0.17341
2.3ac	2	483(20718)	H-1→L+1 -0.30330, H→L 0.18507, H→L+1 0.60213
2.3ac	3	391(25589)	H-2→L -0.10463, H-1→L 0.60518, H→L+1 0.30956
2.3ac	4	374(26717)	H-2→L 0.15595, H-2→L+1 -0.12460, H-1→L+1 0.63250, H→L -0.21061
2.3ad	1	573(17450)	H-1→L+1 -0.33753, H→L 0.61816
2.3ad	2	517(19337)	H-1→L 0.38905, H→L+1 0.58700
2.3ad	3	401(24913)	H-1→L 0.57704, H-1→L+1 0.11676, H→L+1 -0.38605
2.3ad	4	395(25291)	H-1→L -0.11582, H-1→L+1 0.60252, H→L 0.33305
2.3bd	1	584(17128)	H-1→L+1 0.23094, H→L 0.64784, H→L+1 -0.12314
2.3bd	2	507(19730)	H-1→L -0.28311, H→L 0.14193, H→L+1 0.62621
2.3bd	3	402(24880)	H-1→L 0.60858, H-1→L+1 0.16167, H→L+1 0.28620

2.3bd	4	377(26539)	H-1→L -0.16142, H-1→L+1 0.63702, H→L -0.22455
2.4ad	1	578(17314)	H-1→L+1 -0.26526, H→L 0.65378
2.4ad	2	576(17348)	H-1→L 0.44288, H→L+1 0.54797
2.4ad	3	411(24352)	H-1→L 0.54853, H→L+1 -0.44587
2.4ad	4	394(25399)	H-1→L+1 0.65374, H→L 0.27083
2.4ac	1	617(16210)	H-1→L+1 0.16826, H→L 0.68302
2.4ac	2	519(19276)	H-1→L -0.45226, H→L+1 0.53604
2.4ac	3	411(24349)	H-1→L 0.52957 H→L+1 0.44886
2.4ac	4	375(26669)	H-5→L+2 -0.10350, H-4→L 0.61682, H-4→L+2 -0.26340, H-4→L+4 0.13438
2.5ac	1	583(17146)	H-1→L+1 0.18250, H→L 0.67805
2.5ac	2	452(22122)	H-1→L 0.52056, H→L+1 -0.46772
2.5ac	3	390(25668)	H-2→L -0.16283, H-1→L 0.44904, H→L+1 0.51166
2.5ac	4	359(27850)	H-2→L 0.66312, H-1→L 0.13614
2.5ad	1	610(16392)	H-1→L+1 -0.27753, H→L 0.64856
2.5ad	2	512(19541)	H-1→L 0.56444, H→L+1 0.42147
2.5ad	3	403(24843)	H-1→L -0.42328, H→L+1 0.56598
2.5ad	4	381(26281)	H-1→L+1 0.64350, H→L 0.28339
2.6	1	665(15041)	H-1→L+1 -0.22744, H→L 0.66310
2.6	2	547(18274)	H-1→L 0.49735, H→L 0.10393, H→L+1 0.48999
2.6	3	407(24593)	H-1→L -0.49648, H→L+1 0.50703
2.6	4	378(26421)	H-1→L+1 0.66792, H→L 0.23117, H→L -0.10301
2.7	1	629(15889)	H-1→L+1 0.11017, H→L 0.69735
2.7	2	569(17576)	H-1→L -0.46211, H→L+1 0.52426
2.7	3	438(22837)	H-3→L 0.29549, H-1→L 0.45485, H→L+1 0.44218
2.7	4	388(25765)	H-3→L 0.56832, H-2→L -0.28448, H-1→L -0.24570

It was predicted from TDDFT calculations that in the case of dioxobacteriochlorins **2.6** and **2.7**, the first excited state will be largely comprised of HOMO to LUMO single-electron excitations and the second excited state will contain similar contributive excitations from HOMO-1 to LUMO and HOMO to LUMO+1. The experimental UV-vis spectra of **2.3-2.5** should consist of contributions from two or three N-H tautomers, as was determined from TDDFT calculations and discussed earlier. The TDDFT-predicted spectra for the individual N-H tautomers of **2.3** are close to each other in the Soret band region but quite dissimilar in the Q-band region. This provides a clear explanation of the relatively narrow Soret band and the

broad Q-band region in the experimental UV-vis spectra of this compound. This was similar to the case of dioxoisobacteriochlorins **2.4** and **2.5** where the two contributing tautomers have similar energies and intensities of their Soret band regions but differing energies of their Q_y- and Q_x-bands as predicted by TDDFT.

Table 3. $\Delta HOMO/\Delta LUMO$ values of studied compounds.

<i>Sample</i>	<i>$\Delta HOMO/eV$</i>	<i>$\Delta LUMO/eV$</i>
2.1	0.29	0.02
2.2	0.44	0.31
2.3ad	0.49	0.16
2.3bc	1.06	0.43
2.3ac	0.81	0.25
2.3bd	0.77	0.25
2.4ad	0.52	0.28
2.4bc	0.84	1.18
2.4ac	0.81	0.66
2.5bc	1.12	0.47
2.5ad	0.42	0.58
2.5bd	0.75	0.73
2.6	0.63	0.64
2.7bd	0.96	0.72
2.7ac	0.93	0.87

Table 3 lists the TDDFT-predicted $\Delta HOMO$ and $\Delta LUMO$ values for **2.1-2.7** using the CAM-B3LYP exchange-correlation functional. The energies of the occupied and unoccupied molecular orbitals were used to calculate these values and these energies were directly listed in the TDDFT output files. In most cases, a $\Delta HOMO > \Delta LUMO$ relationship was observed and this correlates well with the experimentally observed -,+, -, + MCD sign sequence. In the cases of **2.4bc**, **2.5ad**, and **2.6**, a rare $\Delta LUMO > \Delta HOMO$ relationship was predicted by DFT; however,

2.4bc and **2.5ad** were tautomers that were considered to be extremely unlikely to be present in the solution. Due to the closeness of the ΔHOMO and ΔLUMO values for **2.6**, a -,+,+,- MCD sign sequence was experimentally observed and agrees well with the TDDFT results. The coordinates, excited states, molecular orbital images, and electron density distribution plots for compounds **2.1-2.7** are all listed in the Supporting Information section. In general, although not extremely precise in quantitative terms, there is good correlation between the experimental data and TDDFT calculations when considering typical TDDFT error of the predicted excited state energies which provides a good explanation for the experimental trends in the UV-vis and MCD spectra of **2.2-2.7**.

Conclusions

The electronic structures of a variety of octaethyl- porphyrin, oxochlorin, dioxobacteriochlorin, and dioxoisobacteriochlorin samples were analyzed using UV-vis-NIR and magnetic circular dichroism spectroscopy as well as DFT and TDDFT calculations. The UV-vis-NIR data suggested that the degree of peripheral pyrrole double bond reduction influences the NIR absorption of the Q_y -band and so as the degree of reduction was increased, the Q_y -band became more red-shifted and intense. Compounds **2.2-2.7** all possessed a split Soret band in the 395-425 nm spectral region and relatively small splitting of their Q_x - and Q_y -bands. The electronic structure calculations predicted that all key features present in the experimentally observed UV-vis and MCD spectra of **2.1-2.7** can be explained by Goutermann's four-orbital model. In particular, the DFT calculations predicted a $\Delta\text{HOMO} > \Delta\text{LUMO}$ relationship for the majority of

compounds which correlates well with the -,+,-,+ sign sequence in the experimental MCD spectrum in the Vis-NIR spectral region. Also, correctly predicted by TDDFT was the experimentally observed split Soret band and small splitting of the Q_x - and Q_y - bands. Dioxobacteriochlorin **2.6** exhibited an unusual $\Delta\text{HOMO} < \Delta\text{LUMO}$ relationship for bacteriochlorins which is typical in naturally occurring tetrapyrroles such as photosynthetic pigments in plant leaves or algae.

Chapter 3: Simultaneous Prediction of the Energies of Q_x/Q_y - Bands and Intramolecular Charge-Transfer Transitions in Benzoannulated and Non-Peripherally Substituted Metal-Free Phthalocyanines and Their Analogues: No TDDFT Silver Bullet Yet

Summary

The electronic structures of metal-free tetraazaporphyrin (H_2TAP), phthalocyanine (H_2Pc), naphthalocyanine (H_2Nc), and anthracocyanine (H_2Ac) in both unsubstituted and substituted with electron-donating groups at α -positions forms were investigated experimentally using UV-vis and MCD spectroscopies as well as DFT, TDDFT, and semi-empirical ZINDO/S calculations. The

experimental data are indicative of crossover behaviour of the 1^1B_{2u} and 1^1B_{3u} excited states (in classic D_{2h} notation) at ~ 800 nm. A broad scope of exchange-correlation functionals (ECFs) with varying amounts of Hartree-Fock (HF) exchange were utilized. With respect to Q-band energy, Q-band splitting, Q-band centre, and intramolecular charge-transfer (ICT) transitions region prediction, the long-range corrected LC-wPBE and LC-BP86 functionals provided the best correlation between theory and experiment. The ICT transitions, typically observed in the 450-650 nm region for -NR₂, -SR, and -OR substituted phthalocyanines and their analogues were significantly underestimated by the pure GGA (BP86) ECF and strongly overestimated by the ZINDO/S method while the hybrid CAM-B3LYP, PBE1PBE, and B3LYP ECFs were much more effective in the prediction of the energies of these ICT transitions. Ultimately, not a single ECF that was tested could simultaneously predict the splitting and energies of the Q_x- and Q_y-bands in tandem with the ICT transitions region for the relatively large sampling of unsubstituted and substituted metal-free Pcs and their benzoannulated analogues.

Introduction

The aforementioned synthetic oxochlorins were a motivational starting point in this broad electronic structure analysis due to their intense, low energy Q-bands in the near-infrared region of the optical absorption spectrum. The next focal point of this work was on peripheral extension of the π -conjugation in phthalocyanines (Pcs), naphthalocyanines (Ncs), and anthracocyanines (Acs) in addition to the effect of adding electron-donating substituents at α -positions.

There are essentially two approaches that can be taken when designing photochemotherapeutic molecules. Obviously, the goal is to induce red-shift behaviour of the λ_{\max} band in the NIR region of the optical absorption spectrum. Since naturally occurring tetrapyrroles such as chlorophylls absorb and harvest light in this NIR region, one design approach is to synthetically mimic the physical structure of these naturally occurring macrocycles. Additionally, these quasi-natural molecules have the potential for increased cohesion in biological systems and this was the approach taken and described in chapter two. The second design approach is to extend the π -system by increasing peripheral bulk with conjugated moieties which will red-shift the λ_{\max} band due to theorized, more intense π -stacking behaviour. In addition to increasing peripheral bulk, the introduction of electron-donating moieties at α -positions can further affect energies of the frontier π -MOs.

To extend the π -system outward, phthalocyanines, naphthalocyanines, and anthracocyanines were employed and their structures were synthetically modified. Pcs, Ncs, and Acs are molecule classes that are closely related to their tetraazaporphyrin core, both structurally and electronically; examples of which were shown in Fig. 1.

In a broader sense, the chemistry and spectroscopy of phthalocyanines and their analogues lends itself to their vast assortment of applications such as non-linear optics³, materials chemistry⁴⁰, chemical sensing⁴¹, nanotechnology⁴², antimicrobial and antibacterial phototherapy², photodynamic therapy of cancer¹, oxidative catalysis⁴, and dyes or pigments⁴³. Most of these applications focus on the desirable optical properties of Pcs and their analogues with specific reference to the intense and low-energy Q-band observed in the Vis-NIR region. This

Q-band is represented by the first excited state in systems with four-fold, D_{4h} symmetry; however, in the case of low-symmetry or metal-free phthalocyanines and their analogues, the Q-band is split into Q_x - and Q_y -transitions as a result of splitting of the doubly degenerate first excited state of 1E_u symmetry into two components of x- and y-polarization. The energy of the Q-bands in phthalocyanines and their analogues can be tuned by either (1) elimination or addition of annulated benzene rings in Pcs which results in stepwise decrease or increase of the aromatic π -system or (2) by introducing substituents onto the phthalocyanine core⁴⁴⁻⁴⁷. In case (1), the position of the Q-band (average energy of the Q_x - and Q_y -transitions when the Q-band is split) is red-shifted by ~ 100 nm in each case going from TAP to Pc to Nc to Ac systems (Fig. 20). In addition to this, the Q_x/Q_y -band splitting in metal-free compounds historically decreases as the molecular size increases with the large H_2Nc and H_2Ac molecules having only a single Q-band, representing the ${}^1B_{2u}$ and ${}^1B_{3u}$ excited states (in D_{2h} symmetry notation) which are accidentally degenerate⁴⁴. When electron-donating substituents are added at α -positions to Pcs and their analogues, a 40-80 nm red-shift is observed while similar substitutions at β -positions (periphery) cause minimal change in the energetic position of the Q-bands^{48,49}. The different effects observed for either α - or β -positional substitution are attributed to the greater contribution of the α -carbons to the HOMO, which causes greater destabilization of the HOMO when applying electron-donating groups⁵⁰. In reference to the metal-free compounds under study, the Q_x/Q_y -band splitting decreases as their energies decrease⁴⁷. Contradicting earlier assumptions, one research group has recently shown experimental UV-vis spectra for H_2Nc and H_2Ac which feature significant splitting ($230\text{-}250\text{ cm}^{-1}$) of the Q-band into Q_x - and Q_y -components when using CCl_4 solvent⁵¹. Another report demonstrated splitting of the Q_x - and Q_y -bands present at 980 and 954 nm,

respectively for the $H_2(\alpha\text{-OipT})_8\text{Ac}$ compound in polar THF solution⁵². These recent findings justify a reevaluation of the electronic structures and excited states which exhibit accidental degeneracy in metal-free phthalocyanines and their analogues.

Additionally, the relatively intense intramolecular charge-transfer (ICT) bands observed in the 400-600 nm range for the expanded Pcs which were α -substituted with electron-donating groups originate from single-electron excitations from the donor-atom lone pair to the macrocycle-centred π^* molecular orbitals⁵⁰. The extra bands observed in this range for the expanded Pcs are attributed to low-intensity $\pi\text{-}\pi^*$ transitions⁴⁴. The electronic structures, UV-vis spectroscopy, Q_x - and Q_y -band energies, and Q-band splitting of the metal-free Pcs and their analogues have been studied by means of PPP^{49,53}, semi-empirical ZINDO/S⁴⁴, TDDFT^{47,54}, and SAC-CI^{45,55} methods; however, no comprehensive study has been conducted on the simultaneous prediction of Q_x - and Q_y -band energies and splitting as well as ICT transitions in the substituted and unsubstituted metal-free Pcs and their analogues, which would compare both semi-empirical and modern TDDFT methods.

In this chapter, experimental UV-vis and MCD spectroscopy as well as TDDFT and ZINDO/S calculations are presented on a large sample of metal-free Pcs and their analogues to answer the following questions: (1) how accurately can theoretical methods predict Q_x - and Q_y -band positions in metal-free phthalocyanines and their analogues? (2) Can experimental trends in Q_x - and Q_y -band splitting be predicted by TDDFT and ZINDO/S methods? (3) What is the nature of the low-intensity bands observed between 400 and 600 nm in the Pcs that have been α -substituted by electron-donating groups? (4) Can the agreement between experimental data and

predicted vertical excitation energies be improved by long-range corrected exchange-correlation functionals of the target compounds?

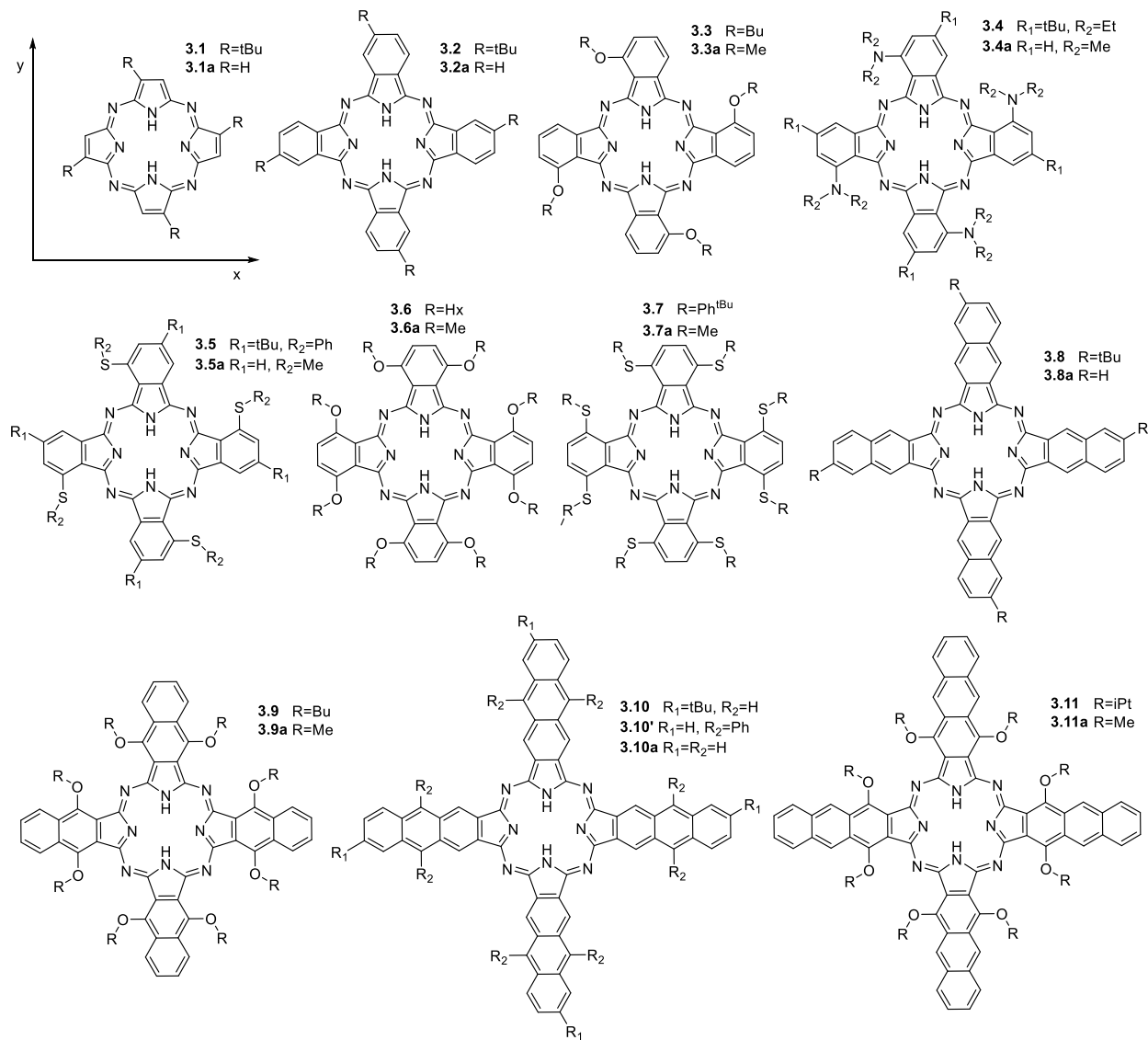


Figure 20. Target metal-free Pcs and their analogues.

Experimental Details

Materials and Instrumentation.

In order to remove possible moisture or acid contamination, all solvents were purified using standard procedures⁵⁶. Compounds **3.1**, **3.2**, **3.6**, **3.8**, and **3.9** were either purchased from commercial sources or prepared using previously published procedures^{44,49,57}. Compounds **3.3**, **3.4**, and **3.5** were received from Professor Eugenii Lukyanets and **3.7** was obtained from Professor Keiichi Sakamoto. Jasco-720 or Cary 17 spectrophotometers were used to collect UV-vis data. An OLIS DCM 17 CD spectropolarimeter with a 1.4 T DeSa magnet was used to obtain MCD data. The MCD spectra were measured in terms of $mdeg=[\theta]$ and were converted to $\Delta\epsilon=(M^{-1}cm^{-1}T^{-1})$ using the following conversion formula: $\Delta\epsilon=\theta/(32980*Bdc)$; where B is magnetic field in T, d is path length in cm, and c is concentration⁵⁸ in M. The complete spectra were measured in parallel and anti-parallel directions with respect to magnetic field at room temperature. Preliminary MCD spectra were collected by Jared Sabin and Prof. Victor Nemykin.

Computational Aspects.

All calculations were completed using Gaussian 03⁵⁹ or Gaussian 09²³ software with UNIX OS or Windows. The molecules were designed with Gaussview 5.0 Software¹⁷ and following an initial “clean-structure” command, the coordinates were submitted for optimization calculations. The BP86 optimized geometries were used for gas-phase calculations with TPSSh, LC-wPBE, LC-BP86, and BP86 ECFs as well as ZINDO/S calculations and B3LYP/PCM optimized geometries were

used for the B3LYP/PCM and CAM-B3LYP/PCM calculations. The TPSSh/PCM and PBE1PBE/PCM calculations employed geometries that were optimized at the same level of theory. The geometry for all compounds was optimized without reduction except all X-(Alk)_n or X-(Aryl)_n groups (where X=O,S, n=1; X=N, n=2) were replaced with methyl groups and the tBu groups were replaced with hydrogen atoms to reduce computational cost. For the tetrasubstituted Pcs, only one of four possible positional isomers was prepared in an effort to avoid further symmetry reduction with this isomer having the four substituents positioned in the most symmetric configuration (Fig. 20). The highest possible *D*_{2h} point group was used to optimize compounds **3.1**, **3.2**, **3.6**, **3.8**, and **3.10**. The *C*_{2v} point group was used to optimize compounds **3.9** and **3.11** and the *C*_{2h} point group was used to optimize **3.3** and **3.5**. In the case of compound **3.7**, it was determined that the *D*₂ conformation was 4.4-5.3 kcal/mol less stable than the *C*_{2v} symmetry conformation. Although both geometries gave quite similar results, only the *C*_{2v} conformation of **3.7** was used for this reason. Two nearly energetically equivalent (0.06-0.28 kcal/mol difference) atropisomers ($\alpha,\alpha,\alpha,\alpha$ - and $\alpha,\beta,\alpha,\beta$ -), optimized in the *C*₁ point group, were considered for compound **3.4** since its -NMe₂ groups are not exactly coplanar. Data for the $\alpha,\beta,\alpha,\beta$ -isomer are presented below.

Vibronic frequencies were calculated for all optimized geometries to confirm potential energy surface minima on the macrocycles. To ensure that both B- and Q-band regions of the UV-vis spectra were covered, the excitation energies of the lowest 60-100 singlet excited states were considered for the TDDFT approach. It was determined via test calculations that the larger 6-311G(d) and 6-311+G(d) basis sets gave only minor changes to the vertical excitation energies and electronic structure predictions, so a medium-sized 6-31G(d) basis set⁶⁰ was used after considering macrocycle size. The TDDFT and single point calculations were performed using the

pure GGA BP86, the long-range corrected CAM-B3LYP, LC-wPBE, and LC-BP86, and hybrid PBE1PBE, B3LYP, and TPSSh exchange-correlation functions. Additional test calculations of the Q_x - and Q_y -band energies of compounds **3.1**, **3.7**, and **3.8** were also performed using EOMCCSD, TPSS, M06L, wB97X, wB97, BMK, M062X, HSeh1PBE, X3LYP, wB97XD, O3LYP, M06HF, and B97D methods. The VModes program⁶¹ was employed to calculate atomic orbital contribution percentages of the respective molecular orbitals. Gaussview 5.0 software¹⁷ was used to model all theoretical spectra calculated by TDDFT and the bandwidth was 800 cm^{-1} in all cases. The custom-made semi-empirical ZINDO/S program, where 100 excited states were considered, was used for the simulation of UV-vis and MCD spectra of all studied compounds. Due to limitations with this program, the absolute magnitude of the MCD signals that were calculated for the Q_x - and Q_y -bands of **3.8** and **3.9** exceeded the maximum programmed value of 1000 for the B-terms; in other words, their absorbance maxima were unavoidably exceeded and the MCD spectra of **3.10** and **3.11** were not calculated.

Results and Discussion

UV-Vis and MCD Spectra of Expanded and α -Substituted Pcs and their Analogues

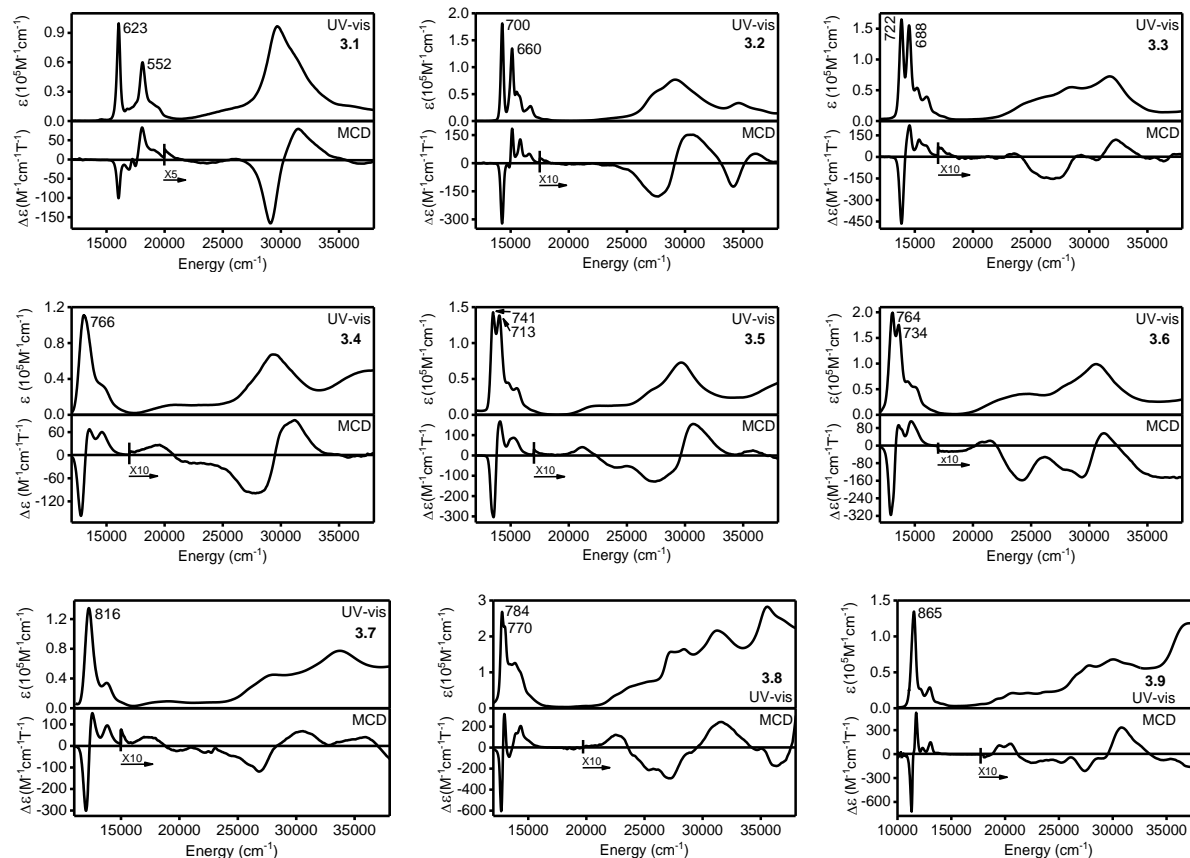


Figure 21. Experimental UV-vis and MCD spectra of compounds **3.1-3.9**.

The UV-vis and MCD spectra of the studied metal-free phthalocyanines and their analogues are shown in Fig. 21. It has been previously established that the energy gap between the Q_x - and Q_y -bands decreases upon a stepwise increase in benzoannulation ($H_2TAP < H_2Pc < H_2Nc < H_2Ac$) and these two bands merge into a single band in the case of the H_2Nc and H_2Ac compounds^{51,62}. This has been observed by experimental UV-vis measurement of H_2Nc^{tBu} (**3.8**)

and $\text{H}_2\text{Ac}^{\text{tBu}}$ (**3.10**) in pyridine, which showed only a single Q-band in the low-energy spectral region⁴⁴; however, in a recent report one group⁵¹ demonstrated experimental Q-band splitting into Q_x - and Q_y -components with $\text{H}_2\text{Nc}^{\text{tBu}}$ (**3.8**) and $\text{H}_2\text{Ac}^{\text{Ph8}}$ (**3.10**) in CCl_4 . To examine this discrepancy, UV-vis spectra of **3.8** in a wide variety of solvents were collected (Fig. 22).

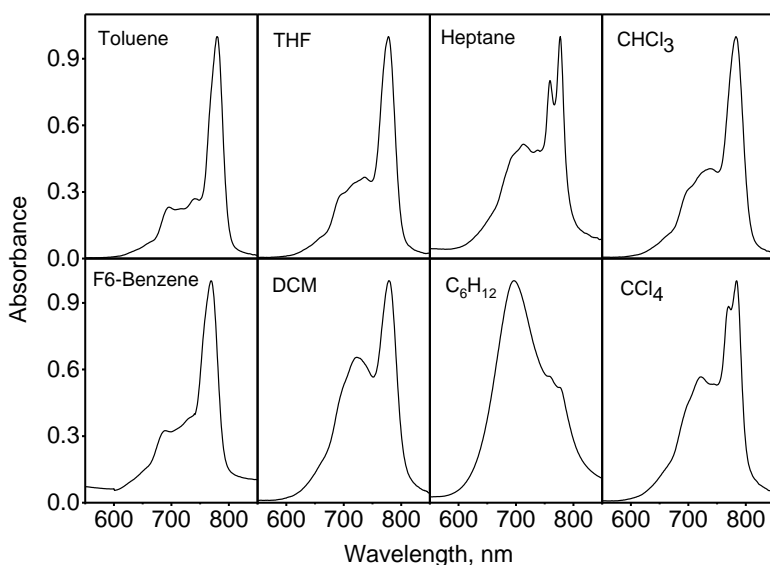


Figure 22. Experimental UV-vis spectra of $\text{H}_2\text{Nc}^{\text{tBu}}$ (**3.8**) in a variety of solvents.

The above UV-vis spectra of **3.8** in DCM, CHCl_3 , pyridine, toluene, benzene, and THF all show a single Q-band in the vis-NIR region; however, both Q_x - and Q_y -components were observed in cyclohexane, heptane, and CCl_4 . Interestingly, the bandwidth of the single Q-band of **3.8** when dissolved in DCM, pyridine, and THF was larger than those of the bands that were split into Q_x - and Q_y -components in heptane and CCl_4 .

To better understand these UV-vis observations, MCD spectra of H₂Nc^{tBu} (**3.8**) were collected in four different solvents. The MCD spectra of compounds **3.1-3.11** should only be interpreted using Faraday *B*-terms since all compounds are diamagnetic (no *C*-terms expected) and have no degenerate excited states (dictated by effective symmetry). The MCD spectrum of **3.8** in CCl₄, which showed the smallest degree of aggregation out of all non-polar solvents, shows clear MCD Faraday *B*-terms going from negative to positive, in ascending energy, at 789 and 772 nm, respectively. These signals are closely associated with observed maxima at 784 and 770 nm in the corresponding UV-vis spectrum (Fig. 21). When using more polar solvents, the Q-band maximum in the UV-vis spectra occurs close to the MCD signal crossing point, typically observed as MCD Faraday *A*-terms and usually caused by degenerate excited states in porphyrinoid systems. Considering the effective D_{2h} symmetry that these metal-free Pcs and their analogues possess, MCD Faraday *A*-terms are not possible and are derived as a result of accidental degeneracy^{51,52}. A MCD Faraday pseudo *A*-term results from this accidental degeneracy and consists of two closely spaced MCD Faraday *B*-terms of opposite sign (Fig. S72).

Another interesting trend observed in the MCD spectra of **3.8** in various solvents is the aggregation behaviour. The formation of H-aggregates is common for Pcs and their analogues and result in the appearance of new bands which are blue shifted and possess a negative to positive sign pattern in their MCD spectra. From this methodology and with respect to compound **3.8**, the ratio of MCD intensities of the positive *B*-term to the negative *B*-term of the Q-bands were used to determine the relative degree of aggregation of **3.8** in the different solvents. The result of this comparison follows: pyridine < THF < CCl₄ < DCM. In many cases, the Q-band region showed a minor solvatochromic effect caused by π-π* transitions which resulted

in solvent-dependent aggregation of **3.8** and splitting of the Q-band into Q_x- and Q_y- components.

The observed Q_x- and Q_y-band splitting in **3.1** and **3.2** was also slightly solvatochromic and reached up to ~200 cm⁻¹ in **3.1**, which was similar to the case of H₂Nc^{tBu} (**3.8**) (Table 4).

Table 4. Experimental UV-vis Q-band data.

<i>Compound</i>	<i>Solvent^a</i>	<i>Q_y (cm⁻¹)</i> <i>λ (nm)</i>	<i>Q_x (cm⁻¹)</i> <i>λ (nm)</i>	<i>Q_x-Q_y</i> <i>(10³ cm⁻¹)</i>	<i>0.5[Q_x+Q_y]</i> <i>(10³ cm⁻¹)</i>	<i>ΔE</i> <i>(10³ cm⁻¹)</i>	<i>Ref^b</i>
H₂TAP^{tBu} (3.1)	CCl ₄	18116	16051	2.065	17.08	0	tw
		552	623				
	DCM	18083	16103	1.980	17.09		tw
		553	621				
	Py	18165	16155	2.010	17.16		42
		550	619				
H₂Pc^{tBu} (3.2)	CCl ₄	15129	14286	0.843	14.71	-2.37	tw,49
		661	700				
	DCM	15106	14327	0.779	14.72		tw
		662	698				
	Py	15049	14316	0.733	14.68		42
		664	698				
H₂(α-OBu)₄Pc (3.3)	THF	14514	13850	0.664	14.18	-2.90	tw,47
		689	722				
	DCM	14454	13812	0.639	14.13		tw
		692	724				
H₂(α-NEt₂)₄Pc^{tBu} (3.4)	Deconv.	13376	12888	0.488	13.13	-3.95	tw
	CCl ₄	748	776				
		13038	13038				
H₂(α-NBu₂)₄Pc	CHCl ₃	767	767	0.000	12.99		61
		12987	12987				
		770	770				
H₂(α-SPh)₄Pc^{tBu} (3.5)	THF	14025	13495	0.529	13.76	-3.32	tw,47
		713	741				
	CCl ₄	14164	13550	0.614	13.86		tw
		706	738				
H₂(α-SBu)₄Pc	THF	14085	13633	0.452	13.85		47
		710	734				
		14085	13633				
H₂(α-OHx)₅Pc	CCl ₄	13624	13089	0.535	13.36	-3.72	tw

(3.6)		734	764				
H₂(α-OPt)₈Pc	PhMe	13550	13123	0.427	13.34		55
		738	762				
H₂(α-SPh^{tBu})₈Pc	Deconv.	12449	12105	0.344	12.28	-4.80	tw
(3.7)		803	826				
	DCM	12255	12255	0.000	12.26		tw,62
		816	816				
H₂(α-SBu)₈Pc	THF	12430	12430	0.000	12.43		47
		805	805				
H₂Nc^{tBu} (3.8)	CCl ₄	12987	12755	0.232	12.87	-4.21	tw,49
		770	784				
	Heptane	13175	12870	0.305	13.02		tw
		759	777				
	DCM	12821	12821	0.000	12.82		tw
		780	780				
	Py	12762	12762	0.000	12.76		42
		784	784				
H₂(α-OBu)₈Nc	CCl ₄	11574	11574	0.000	11.57	-5.51	tw
(3.9)		864	864				
	Heptane	11669	11669	0.000	11.67		tw
		857	857				
H₂Ac^{Ph8} (3.10)	CCl ₄	11062	11312	-0.250	11.19	-5.89	49
		904	884				
H₂Ac^{tBu}	Py	11650	11650	0.000	11.65		42
		858	858				
H₂(α-OiPt)₈Ac	PhMe	10204	10482	-0.278	10.34	-6.74	50
(3.11)		980	954				

^adeconv. = Q-band positions were determined via deconvolution analysis. ^btw = this work

Similar to previous reports, the use of non-polar solvents such as CCl₄ caused the largest Q-band splitting in the UV-vis and MCD spectra of H₂TAP^{tBu} (**3.1**) and H₂Pc^{tBu} (**3.2**). In the case of compound **3.10**, the octaphenyl-substituted H₂Ac^{Ph8} showed Q_x- and Q_y-band splitting of ~150 cm⁻¹ (51) in CCl₄ while the tetra-*tert*-butyl substituted H₂Ac^{Ph8} version, run in more polar pyridine, displayed only a single Q-band which corresponds to an MCD Faraday pseudo A-term and these results are in agreement with the previously observed solvent polarity dependence data which is

available on the $H_2Ac^{(R)n}$ compounds. Also, additional bands were observed in the 450-600 nm region of their UV-vis and MCD spectra for the $H_2Nc^{(R)n}$ and $H_2Ac^{(R)n}$ compounds (Fig. 21).

Due to increased resolution of the Q_x - and Q_y -bands in non-polar solvents, the UV-vis and MCD spectra of the Pcs and Ncs, which were substituted with electron-donating groups at α -positions, were investigated (Fig. 21). The general trends for aryl-thiol and alkoxy-substituted compounds in more polar THF were previously reported by Lukyanets, Kobayashi, and co-workers⁴⁹ and their data agrees well with data collected in this work regarding trends of the Q_x - and Q_y -band energies for $H_2(\alpha-OC_6H_{13})_8Pc$ (**3.6**) in CCl_4 . For the phthalocyanine compounds having the same number of substituents, red-shifting of the Q-band increased in the following order: $-OR < -SR < -NR_2$ with the $H_2(\alpha-NEt_2)_4Pc^{tBu}$ compound possessing a Q-band that is ~ 100 nm red-shifted to that of the parent H_2Pc^{tBu} . Upon stepwise benzoannulation of the parent core, the Q-band centre increased by about 100 nm upon going from $H_2(\alpha-OC_6H_{13})_8Pc$ (**3.6**) to $H_2(\alpha-OBu)_8Nc$ (**3.9**) to $H_2(\alpha-OiPent)_8Ac$ (**3.11**). In the cases of $H_2(\alpha-OMe)_8Nc$, $H_2(\alpha-p-SPh^{tBu})_8Pc$, and $H_2(\alpha-NMe)_4Pc^{tBu}$, the Q_x - and Q_y -bands collapse into a single band which is quite broad and is associated with Faraday pseudo A-terms which are observed in their MCD spectra. The broadest Q-band (FWHM $\sim 1200\text{ cm}^{-1}$) was observed for the $H_2(\alpha-NEt_2)_4Pc^{tBu}$ (**3.4**) compound. The broadness of the Q-band in cases where only a single Q-band was observed was investigated and the FWHM (full width at half maximum) was determined for all compounds. The largest magnitude of uncharacteristic broadening was observed for the $H_2(\alpha-NEt_2)_4Pc^{tBu}$ (**3.4**) (1200 cm^{-1}) and $H_2(\alpha-p-SPh^{tBu})_8Pc$ (**3.7**) (600 cm^{-1}) compounds (Table 4). This broadening has been observed with similar compounds before but has not been discussed in any sort of detail. This broadening is reflective of either two Q_x - and Q_y -bands that are closely spaced in energy or the presence of

multiple positional isomers (**3.4** only). As has been recently demonstrated by Kobayashi⁴⁹, Jiang⁶³, and Nemykin⁵⁵, the UV-vis and MCD spectra of the $H_2(\alpha-NR_2)_4Pc$ compounds and their metallated analogues are dominated by a single positional isomer due to the relative bulkiness of the NR_2 groups, which prefer to form the most symmetric phthalocyanines (Fig. 20). The idea that the single, broad Q-bands observed for the $H_2(\alpha-NEt_2)_4Pc^{tBu}$ (**3.4**) and $H_2(\alpha-p-SPh^{tBu})_8Pc$ (**3.7**) compounds were comprised of Q_x - and Q_y -bands that were closely spaced in energy was investigated via deconvolution analysis of the Q-band region (Fig. 23).

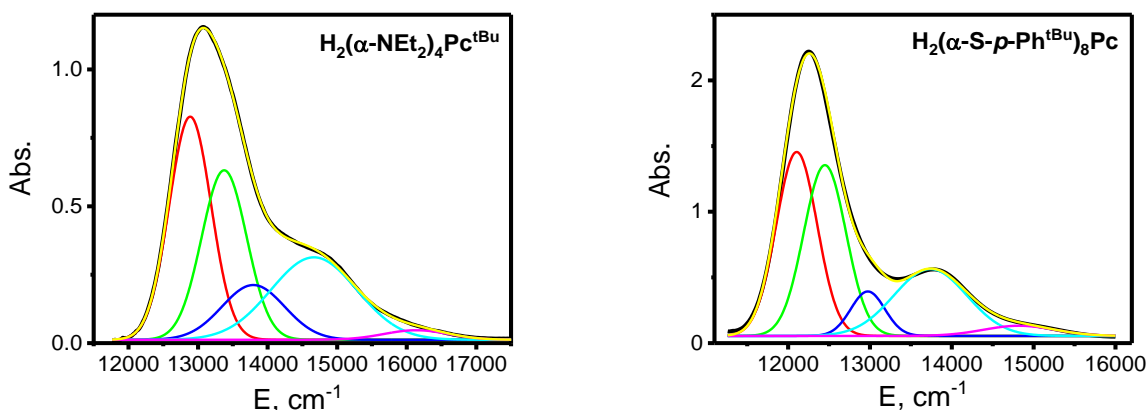


Figure 23. Q-band region deconvolution analysis spectra of $H_2(\alpha-NEt_2)_4Pc^{tBu}$ (**3.4**) and $H_2(\alpha-S-p-Ph^{tBu})_8Pc$ (**3.7**).

The results of the band deconvolution analysis show that the single Q-band is comprised of Q_x - and Q_y -bands that appear merged since they are so close in energy; however, even though the results of this analysis converged to very similar results using different starting points, the results of this deconvolution analysis are to be considered highly theoretical at this

point. Nonetheless, this result provides a much better explanation of the unusual broadening of the apparent single Q-bands in the UV-vis spectra of **3.4** and **3.7**. Compounds **3.4**, **3.5**, **3.6**, **3.7**, **3.9**, and **3.11**, which were all substituted with electron-donating groups at α -positions, all have additional bands between 450-600 nm and were assigned as interligand -OR/-SR/-NR₂ to -Pc/Nc/Ac charge-transfer (ICT) transitions and will be discussed below in comparison with TDDFT calculations. For the alkoxy derivatives, the Q_x- and Q_y-band splitting follows the order: H₂(α -OBu)₄Pc > H₂(α -OC₆H₁₃)₈Pc > H₂(α -OBu)₈Nc < H₂(α -OiPent)₈Ac. Considering the parent systems dissolved in CCl₄, the Q_x- and Q_y-band splitting progresses in the following order: H₂TAP^{tBu} > H₂Pc^{tBu} > H₂Nc^{tBu} < H₂Ac^{Ph8}. Both of these trends indicate the possibility of crossover behaviour of the ¹B_{2u} and ¹B_{3u} excited states.

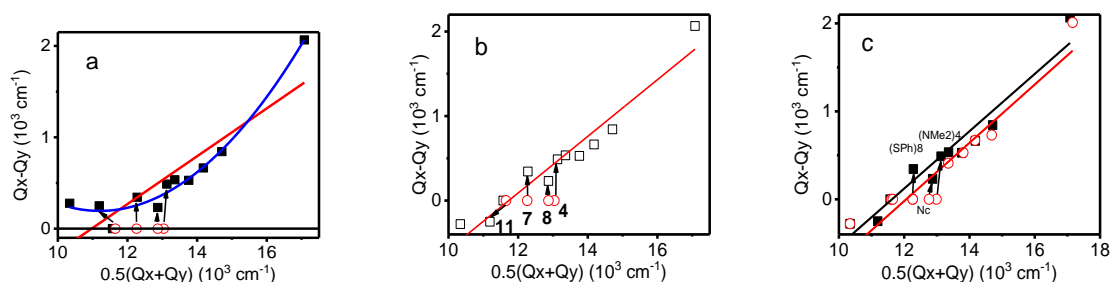


Figure 24. Q-band splitting vs. Q-center correlation plots for (a) no ¹B_{2u} and ¹B_{3u} intercrossing, (b) possible ¹B_{2u} and ¹B_{3u} intercrossing, and (c) deconvolution analysis.

An experimental observation that the Q_x-/Q_y-band splitting in H₂Nc^{tBu} < H₂Ac^{Ph8} and H₂(α -OBu)₈Nc < H₂(α -OiPent)₈Ac pairs increases with the increase of the aromatic π -system contradicts the earlier suggestion that the Q_x- and Q_y-bands in metal-free phthalocyanines and their

analogues collapse into a single band when the target compounds have absorption above ~ 770 nm. Indeed, if one would assume a lack of the 1^1B_{2u} and 1^1B_{3u} intercrossing, then the energy center of the Q-bands versus Q_x - Q_y splitting graph will have a “J-shape” character (Figure 24a). Once we assume that the intercrossing between the 1^1B_{2u} and 1^1B_{3u} excited states is possible, then the Q_x - Q_y vs $0.5(Q_x+Q_y)$ correlation graph becomes more linear with the $H_2(\alpha\text{-NEt}_2)_4Pc^{tBu}$ and $H_2(\alpha\text{-S-p-Ph}^{tBu})_8Pc$ compounds being the largest outliers (Figure 24b). Finally, if band deconvolution results are used to resolve anomalous broadening of the Q-band in the $H_2(\alpha\text{-NEt}_2)_4Pc^{tBu}$ and $H_2(\alpha\text{-S-p-Ph}^{tBu})_8Pc$ compounds, then the Q_x - Q_y vs $0.5(Q_x+Q_y)$ correlation would be the most straightforward (Figure 24c).

TDDFT and ZINDO/S Calculations

In order to probe the above proposed idea of potential intercrossing of the 1^1B_{2u} and 1^1B_{3u} excited states in metal-free Pcs and their analogues, time-dependent density functional theory (TDDFT) and semi-empirical ZINDO/S calculations were performed on compounds **3.1-3.11**. Several theoretical studies on core-extended, metal-free tetraazaporphyrins are currently available in literature^{44,45,65}. For example, spectroscopic trends in metal-free expanded tetraazaporphyrins were explored by Kobayashi and co-workers using semi-empirical ZINDO/S calculations⁴⁴. There have also been many TDDFT studies reported on metal-free Pcs and their analogues⁵⁴. In two interesting publications, SAC-CI methodology was compared with TDDFT results on metal-free tetraazaporphyrin and its analogues by Nakatsuji^{45,55} and coworkers. B3LYP TDDFT calculations were used to predict the vertical excitation energies and electronic

structures of several Pcs which were α -substituted with -OR and -SR groups and were discussed by Stillman, Kobayashi, Zhang, and coworkers^{47,66}. Also, TDDFT calculations on different phthalocyanines that were α -substituted with -NR₂ groups are available^{49,55,63}; however, no comprehensive investigation into the influence of exchange-correlation functional on simulated vertical excitation energies of metal-free expanded and α -substituted with electron-donating groups phthalocyanines and their analogues is available in literature.

It has already been proven that TDDFT calculations can successfully predict the vertical excitation energies and electronic structures of porphyrinoids⁶⁷ and also that the amount of Hartree-Fock exchange within the ECF is more important for the determination of the energies of the π - π^* and n - π^* transitions for Pcs rather than the actual basis set quality⁶⁴ (this is assuming the inclusion of a polar function on heavy atoms and that the minimal basis set is of double- ζ quality). The dominant influence of the exchange-correlation functional on the Q_x- and Q_y-band energies and splitting was confirmed using H₂Nc as a test compound since accurate prediction of these values was of high interest (Fig. 25, S1125).

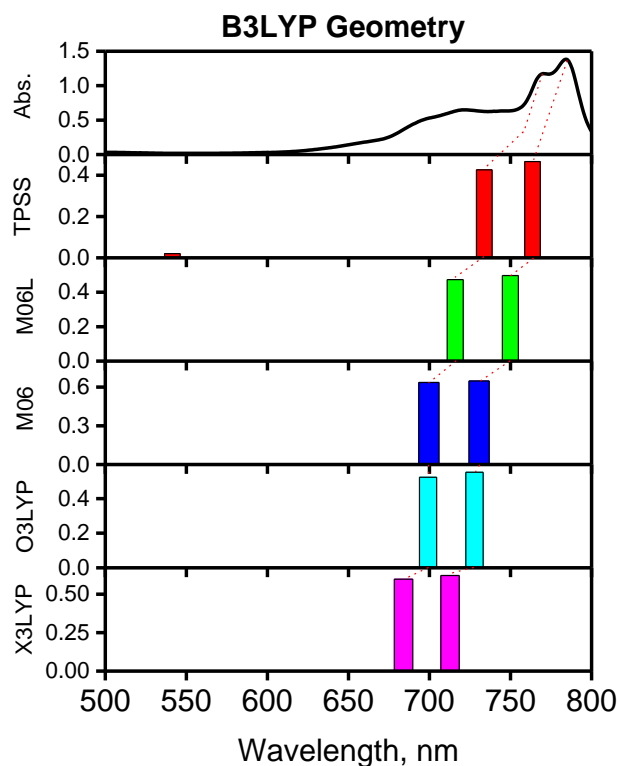


Figure 25. Simulated Q-band splitting for H₂Nc using B3LYP-predicted geometry and various ECFs.

BP86- and B3LYP-predicted geometries of H₂Nc were tested to investigate the influence of starting geometry on the predicted energies of the Q-bands. It was determined that the amount of Hartree-Fock exchange within the exchange-correlation functional agrees well with the simulated vertical excitation energies of the Q_x- and Q_y-bands and their splitting, which is in good agreement with prior calculations on phthalocyanines and their analogues (Fig. 26).

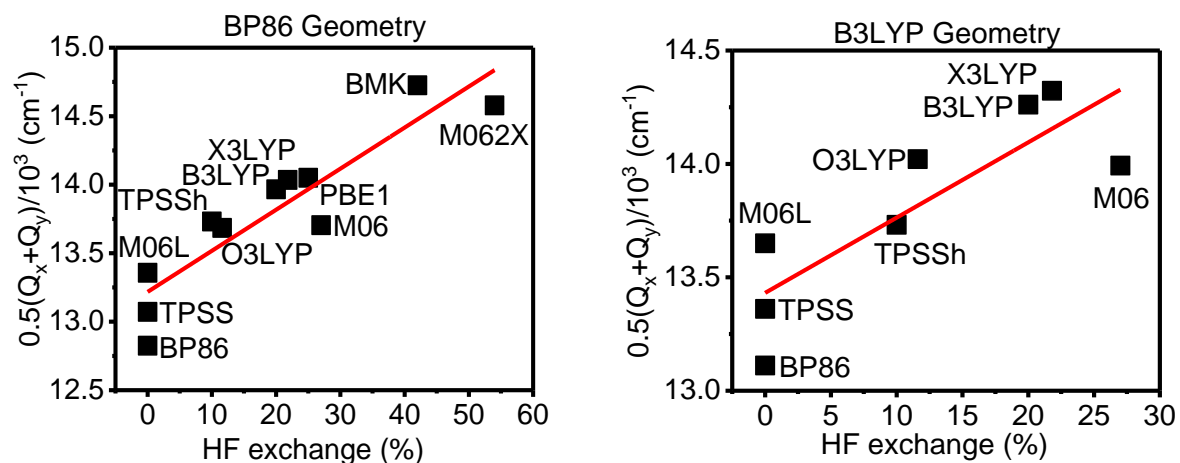


Figure 26. Correlation between Q-band splitting and Hartree-Fock exchange for H₂Nc using BP86 and B3LYP geometries.

Compared to the “hybrid” ECFs, the GGA and long-range corrected GGA-related exchange-correlation functionals (BP86, LC-wPBE, and LC-BP86) provided better correlation between experiment and theory, overall. The quite popular B3LYP ECF, which possesses ~20% of Hartree-Fock exchange overestimated, by ~0.2 eV, the Q_x- and Q_y-band energies and this overestimation increased with the amount of HF present in the calculation. The initial geometry was found to have only a very minor influence. A broad scope of exchange-correlation functionals were used for the calculation of compounds **3.1-3.11** including PBE1PBE (hybrid with a large amount of Hartree-Fock exchange), CAM-B3LYP (long-range corrected hybrid), B3LYP (standard hybrid), TPSSh (hybrid meta-GGA with a smaller amount of HF exchange), LC-wPBE (long-range corrected GGA), LC-BP86 (long-range corrected GGA), and BP86 (pure GGA). It was also determined, although by no surprise, that the incorporation of solvent effects into the

calculations helped to improve the agreement between experiment and theory for the hybrid ECFs, so the polarized continuum model (PCM) was used for these types of exchange-correlation functionals. The semi-empirical ZINDO/S method was also used as a reference since it has been a traditional option for the calculation of vertical excitation energies of phthalocyanines and their analogues and was interesting to see how they compared to the more modern and expensive TDDFT approach. Also, the ZINDO/S codes which were modified by Joseph Michl and co-workers makes the calculation of Faraday MCD *B*-terms possible, so it was hypothesized that the ZINDO/S approach could assist in the explanation of experimentally observed MCD spectral trends in the metal-free phthalocyanines and their analogues. All computationally-predicted data for the Q-bands are listed in Tables 5-8 and Figs. 27-30.

Table 5. Calculated Q-band data for compounds **3.1-3.11**.

<i>Functional/Method</i>	Q_y (cm^{-1}) λ (nm)	Q_x (cm^{-1}) λ (nm)	$F(Q_y)$	$F(Q_x)$	$Q_x - Q_y$ ($10^3 cm^{-1}$)	$0.5[Q_x + Q_y]$ ($10^3 cm^{-1}$)
H₂TAP (3.1a)						
LC-wPBE	15198 658	17794 562	0.1735	0.1678	2.596	16.50
LC-BP86	14999 667	17650 567	0.1893	0.1825	2.651	16.32
BP86	18191 550	19137 523	0.0537	0.0562	0.946	18.66
TPSSh	18917 529	19988 500	0.0951	0.0959	1.071	19.45
TPSSh/PCM	18556 539	19514 512	0.2910	0.3039	0.958	19.04
B3LYP/PCM	18407 543	19444 514	0.3396	0.3504	1.037	18.93
PBE1PBE/PCM	18697 535	19798 505	0.3781	0.3830	1.101	19.25
CAM-B3LYP/PCM	17021 588	18563 539	0.3979	0.4011	1.542	17.79

ZINDO/S	14214 704	16821 594	0.2769	0.3100	1.598	15.52
H₂Pc (3.2a)						
LC-wPBE	13850 722	14918 670	0.4304	0.5018	1.068	14.38
LC-BP86	13675 731	14735 679	0.4533	0.5218	1.060	14.21
BP86	15616 640	15873 630	0.2779	0.3350	0.257	15.74
TPSSh	16290 614	16532 605	0.3477	0.4003	0.242	16.41
TPSSh/PCM	15203 658	15234 656	0.7928	0.7517	0.031	15.22
B3LYP/PCM	15270 655	15202 658	0.7935	0.8307	-0.068	15.24
PBE1PBE/PCM	15521 644	15507 645	0.8352	0.8653	-0.014	15.51
CAM-B3LYP/PCM	14603 685	14477 691	0.8838	0.8347	-0.126	14.54
ZINDO/S	13566 737	14489 690	0.6445	0.8279	0.923	14.03
H₂(α-OMe)₄Pc (3.3a)						
LC-wPBE	13533 739	14534 688	0.4790	0.5583	1.001	14.03
LC-BP86	13383 747	14384 695	0.5013	0.5771	1.001	13.88
BP86	14498 690	14113 709	0.3545	0.2613	-0.385	14.31
TPSSh	15232 657	15503 645	0.3671	0.4394	0.271	15.37
TPSSh/PCM	14010 714	13857 722	0.7871	0.8048	-0.152	13.93
B3LYP/PCM	14316 699	14137 707	0.8467	0.8706	-0.179	14.23
PBE1PBE/PCM	14601 685	14454 692	0.8997	0.9067	-0.147	14.53
CAM-B3LYP/PCM	13994 715	13851 722	0.9486	0.9202	-0.143	13.92
ZINDO/S	13399 746	14298 699	0.6791	0.8661	0.899	13.85
H₂(α-NMe₂)₄Pc (3.4a)						
LC-wPBE	13056 766	13947 717	0.5072	0.5792	0.891	13.50
LC-BP86	12888 776	13779 726	0.5258	0.5914	0.891	13.33
BP86	12124 825	11378 879	0.2399	0.1104	-0.746	11.75

TPSSh	13835 723	13438 744	0.3853	0.2770	-0.397	13.64
TPSSh/PCM	12559 796	12352 810	0.6681	0.7012	-0.207	12.46
B3LYP/PCM	13323 751	13079 765	0.7902	0.8260	-0.244	13.20
PBE1PBE/PCM	13601 735	13402 746	0.8530	0.8775	-0.199	13.51
CAM-B3LYP/PCM	13468 743	13342 750	0.9541	0.9415	-0.126	13.41
ZINDO/S	13286 753	14115 708	0.7022	0.8845	0.829	13.70
H₂(α-SMe)₄Pc (3.5a)						
LC-wPBE	13458 743	14403 694	0.4793	0.5587	0.945	13.93
LC-BP86	13299 752	14242 702	0.5025	0.5783	0.943	13.77
BP86	13326 750	12825 780	0.3011	0.1608	-0.501	13.08
TPSSh	14583 686	14811 675	0.3213	0.4183	0.228	14.70
TPSSh/PCM	13625 734	13456 743	0.7400	0.7886	-0.169	13.54
B3LYP/PCM	14034 713	13831 723	0.8301	0.8703	-0.203	13.93
PBE1PBE/PCM	14323 698	14172 706	0.8832	0.9125	-0.151	14.25
CAM-B3LYP/PCM	13919 718	13859 722	0.9615	0.9298	-0.060	13.89
ZINDO/S	13528 739	14416 694	0.6657	0.8504	0.888	13.97
H₂(α-OMe)₈Pc (3.6a)						
LC-wPBE	13193 758	14100 709	0.5233	0.6109	0.907	13.65
LC-BP86	13087 764	14001 714	0.5439	0.6280	0.914	13.54
BP86	12743 785	12303 813	0.3022	0.1943	-0.440	12.52
TPSSh	13899 719	14126 708	0.3339	0.4313	0.227	14.01
TPSSh/PCM	12390 807	12248 816	0.7182	0.8013	-0.143	12.32
B3LYP/PCM	13045 767	12823 780	0.8386	0.8964	-0.222	12.93
PBE1PBE/PCM	13329 750	13153 760	0.9003	0.9470	-0.176	13.24
CAM-B3LYP/PCM	13176 759	13113 763	0.9881	1.0365	-0.063	13.14

ZINDO/S	13207 757	14076 710	0.7123	0.9111	0.869	13.64
H₂(α-SMe)₈Pc (3.7a; C_{2v})						
LC-wPBE	12492 801	13279 753	0.4800	0.5469	0.787	12.89
LC-BP86	12357 809	13154 760	0.5012	0.5653	0.797	12.76
BP86	10960 912	10482 954	0.1940	0.0943	-0.478	10.72
TPSSh	12591 794	12754 784	0.2443	0.3494	0.163	12.67
TPSSh/PCM	11698 855	11496 870	0.6317	0.6983	-0.202	11.60
B3LYP/PCM	12347 810	12071 828	0.7614	0.7957	-0.276	12.21
PBE1PBE/PCM	12577 795	12353 809	0.8169	0.8445	-0.224	12.47
CAM-B3LYP/PCM	12644 791	12580 795	0.9049	0.9363	-0.064	12.61
ZINDO/S	13124 762	13916 719	0.6589	0.8293	0.792	13.52
H₂Nc (3.8a)						
LC-wPBE	12773 783	12929 773	0.6769	0.7642	0.156	12.85
LC-BP86	12607 793	12726 786	0.7052	0.7870	0.119	12.67
BP86	13052 766	12602 794	0.3897	0.4300	-0.450	12.83
TPSSh	13978 715	13482 742	0.5135	0.5442	-0.496	13.73
TPSSh/PCM	12778 783	12109 826	1.0043	0.9898	-0.669	12.44
B3LYP/PCM	13045 767	12298 813	1.0760	1.0517	-0.747	12.67
PBE1PBE/PCM	13314 751	12620 792	1.1304	1.1009	-0.694	12.97
CAM-B3LYP/PCM	12803 781	12161 822	1.1616	1.1716	-0.642	12.48
ZINDO/S	13000 769	12960 772	1.1595	0.9453	-0.040	12.98
H₂(α-OMe)₈Nc (3.9a)						
LC-wPBE	11669 857	11596 862	0.7436	0.7944	-0.073	11.63
LC-BP86	11542 866	11437 874	0.7719	0.8163	-0.105	11.49
BP86	11171 895	10836 923	0.3413	0.3875	-0.335	11.00

TPSSh	12253 816	11813 846	0.4819	0.5107	-0.440	12.03
TPSSh/PCM	11430 875	10761 929	0.9804	0.9647	-0.669	11.10
B3LYP/PCM	11992 834	11209 892	1.0796	1.0509	-0.783	11.60
PBE1PBE/PCM	12188 820	11458 873	1.1414	1.1052	-0.730	11.82
CAM-B3LYP/PCM	11927 838	11183 894	1.2171	1.2089	-0.744	11.56
ZINDO/S	12362 809	12298 813	1.2716	1.0600	-0.064	12.33

H₂Ac (3.10a)

LC-wPBE	12075 828	11694 855	0.8959	0.9677	-0.381	11.89
LC-BP86	11908 840	11473 872	0.9284	0.9915	-0.435	11.69
BP86	10915 916	9679 1033	0.3519	0.3102	-1.236	10.30
TPSSh	12121 825	10912 916	0.4731	0.5364	-1.209	11.52
TPSSh/PCM	11031 906	9895 1011	1.0825	0.9789	-1.135	10.46
B3LYP/PCM	11521 868	10307 970	1.2140	1.0962	-1.214	10.91
PBE1PBE/PCM	11830 845	10673 937	1.2904	1.1679	-1.157	11.25
CAM-B3LYP/PCM	11784 849	10688 936	1.4006	1.3469	-1.096	11.24
ZINDO/S	12724 786	12187 821	1.1525	1.2818	-0.537	12.46

H₂(α -OMe)₈Ac (3.11a)

LC-wPBE	10965 912	10406 961	0.9626	0.9819	-0.559	10.68
LC-BP86	10835 923	10230 978	0.9955	1.0056	-0.605	10.53
BP86	9742 1027	8811 1135	0.3636	0.3365	-0.931	9.28
TPSSh	10872 920	9912 1009	0.5405	0.4941	-0.960	10.39
TPSSh/PCM	10014 999	8968 1115	1.0802	0.9724	-1.046	9.49
B3LYP/PCM	10679 936	9501 1053	1.2230	1.1019	-1.178	10.09
PBE1PBE/PCM	10884 919	9763 1024	1.3038	1.1749	-1.121	10.32
CAM-B3LYP/PCM	10939 914	9784 1022	1.4494	1.3731	-1.155	10.36

ZINDO/S	12198 820	11659 858	1.8583	1.4980	-0.539	11.93
---------	--------------	--------------	--------	--------	--------	-------

Table 6. Exchange-correlation functional fitting data for the Q-centre.

	<i>LC-wPBE</i>	<i>LC-BP86</i>	<i>BP86</i>	<i>TPSSh</i>	<i>TPSSh/PCM</i>	<i>B3LYP/PCM</i>	<i>PBE1PBE/PCM</i>	<i>CAM-B3LYP/PCM</i>	<i>ZINDO/S</i>
Q-Center Intercept	-2.4122	-2.2014	4.59053	2.81913	4.10005	2.97112	2.80813	0.94958	-11.0702
Slope	1.17182	1.3242	0.67033	0.73713	0.70182	0.76598	0.76167	0.92469	1.79978
R	0.98857	0.98058	0.97415	0.99653	0.98436	0.98869	0.98953	0.98883	0.96622
R²	0.97727	0.96153	0.94897	0.99308	0.96896	0.97751	0.97916	0.97778	0.93358
MAD, cm⁻¹	329	348	887	859	709	357	448	234	782

Table 7. Exchange-correlation functional fitting data for the Q-band splitting.

	<i>LC-wPBE</i>	<i>LC-BP86</i>	<i>BP86</i>	<i>TPSSh</i>	<i>TPSSh/PCM</i>	<i>B3LYP/PCM</i>	<i>PBE1PBE/PCM</i>	<i>CAM-B3LYP/PCM</i>	<i>ZINDO/S</i>
Q_x-Q_y Splitting Intercept	-0.0083	0.01338	0.8618	0.57523	0.80648	0.84465	0.79284	0.67895	0.0489
Slope	0.71723	0.68985	1.00064	0.88887	1.08706	1.01035	1.01061	0.85785	0.69927
R	0.97667	0.97265	0.90703	0.90348	0.97512	0.98028	0.98134	0.9745	0.97107
R²	0.95389	0.94605	0.82271	0.81627	0.95086	0.96094	0.96303	0.94965	0.94297
MAD, cm⁻¹	299	325	862	558	780	841	789	714	293

Table 8. Exchange-correlation functional fitting data for Q_x and Q_y intercepts.

	<i>LC-wPBE</i>	<i>LC-BP86</i>	<i>BP86</i>	<i>TPSSH</i>	<i>TPSSH/ PCM</i>	<i>B3LYP/ PCM</i>	<i>PBE1PBE/P CM</i>	<i>CAM-B3LYP/ PCM</i>	<i>ZINDO/S</i>
Q_x Int.	1478	1340	-5213	-3277	-4807	-3388	-3185	-1186	5211
Slope	0.90675	0.90495	1.32858	1.28735	1.31079	1.23196	1.2402	1.06523	0.63858
R	0.98753	0.98149	0.97184	0.99718	0.9898	0.99266	0.99313	0.98861	0.96599
R²	0.97522	0.96333	0.94446	0.99438	0.97971	0.98538	0.9863	0.97736	0.93313
MAD, cm⁻¹	338	347	1141	645	925	542	379	420	776
Q_y Int.	3492	3610	-6897	-4365	-5992	-3732	-3626	-216	8582
Slope	0.73192	0.71192	1.53788	1.42779	1.47445	1.33223	1.34436	1.04772	0.35388
R	0.98845	0.98287	0.97591	0.99117	0.97532	0.98164	0.98287	0.98826	0.9581
R²	0.97704	0.96603	0.9524	0.98242	0.95124	0.96361	0.96604	0.97666	0.91796
MAD, cm⁻¹	333	399	762	1153	551	562	816	399	794

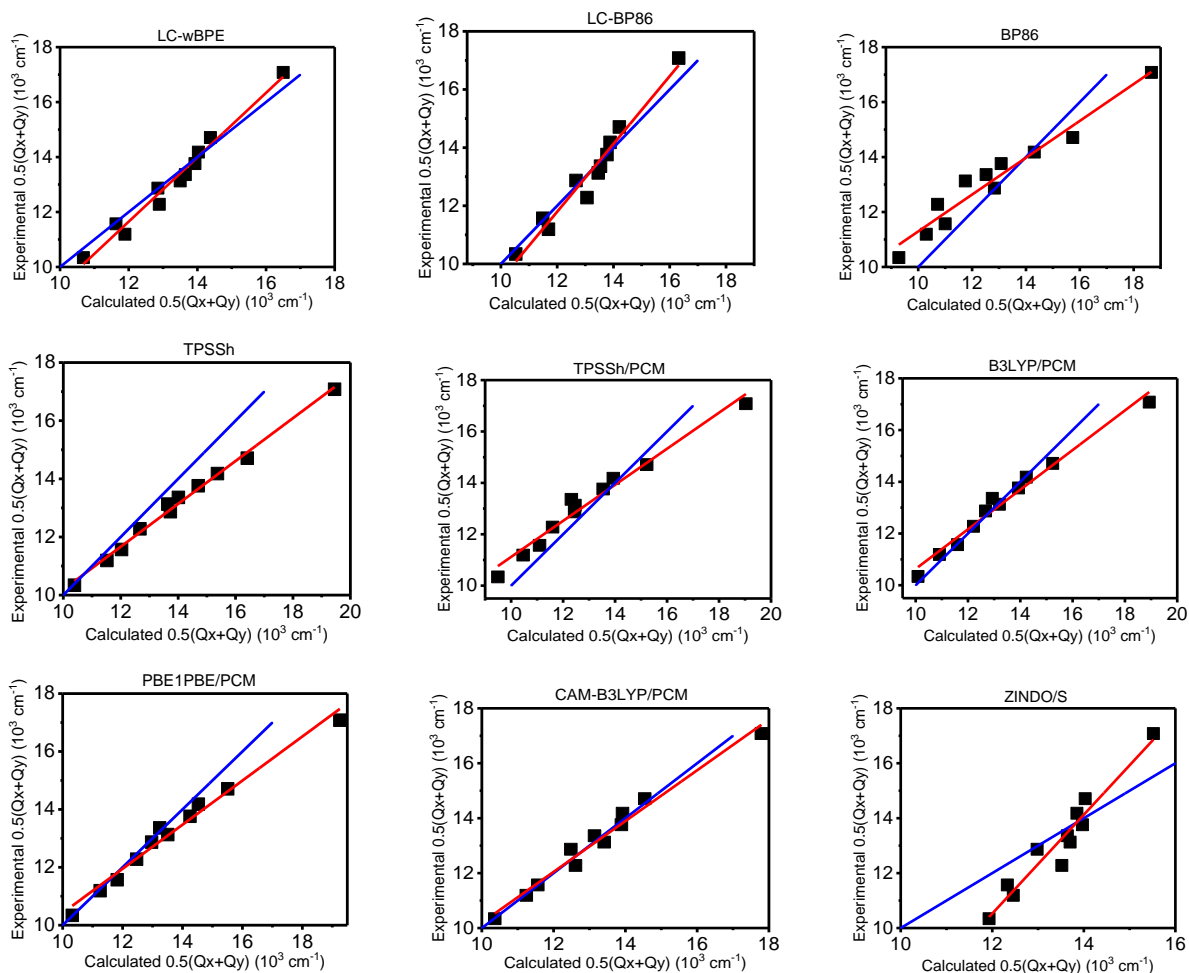


Figure 27. Experimental vs. calculated Q-centre correlation plots for compounds **3.1-3.11** (The blue line represents the ideal agreement between theory and experiment).

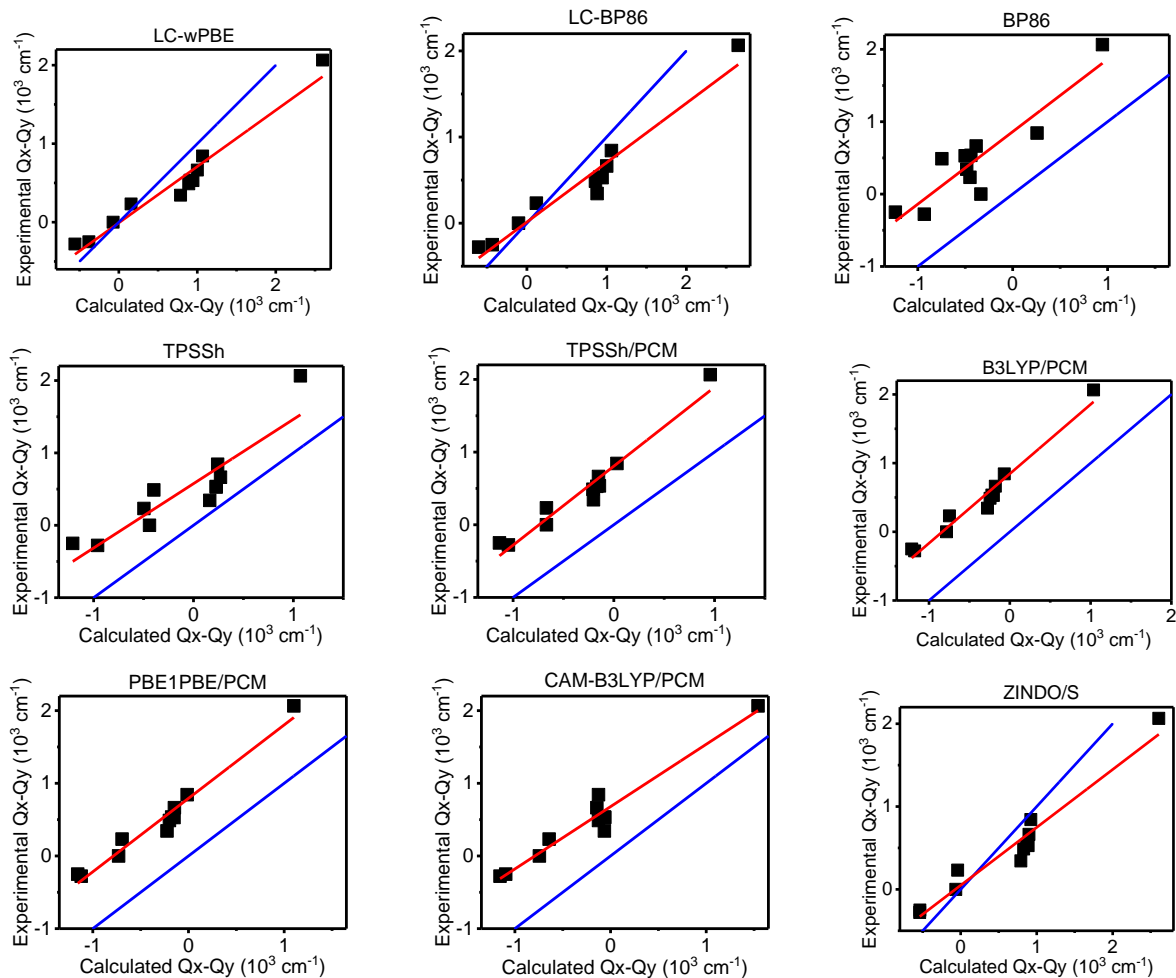


Figure 28. Experimental vs. calculated Q-band splitting correlation plots for compounds **3.1-3.11** (The blue line represents the ideal agreement between theory and experiment).

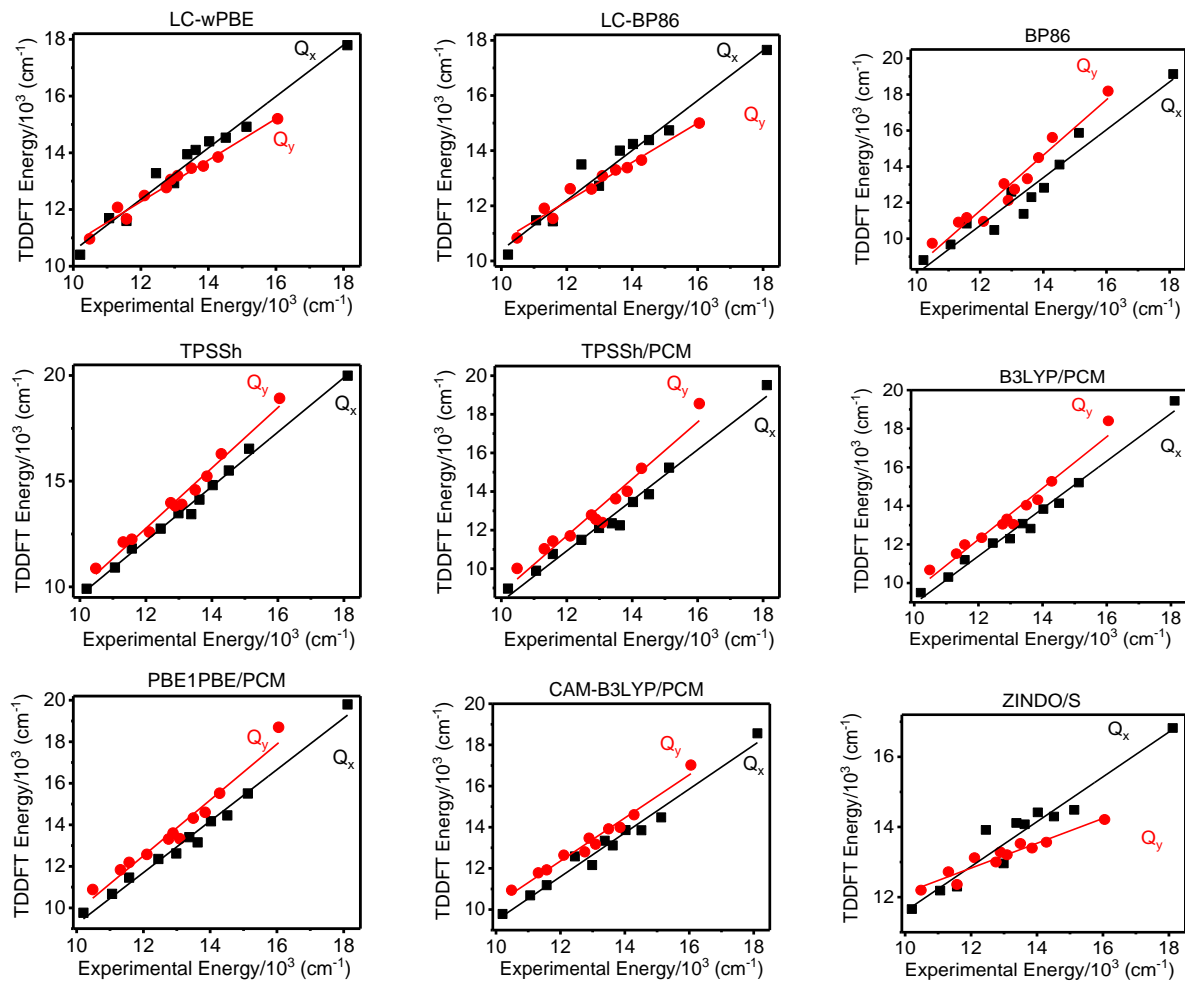


Figure 29. TDDFT vs. experimental Q_x - and Q_y -band energy correlation plots for compounds **3.1-3.11** (The blue line represents the ideal agreement between theory and experiment).

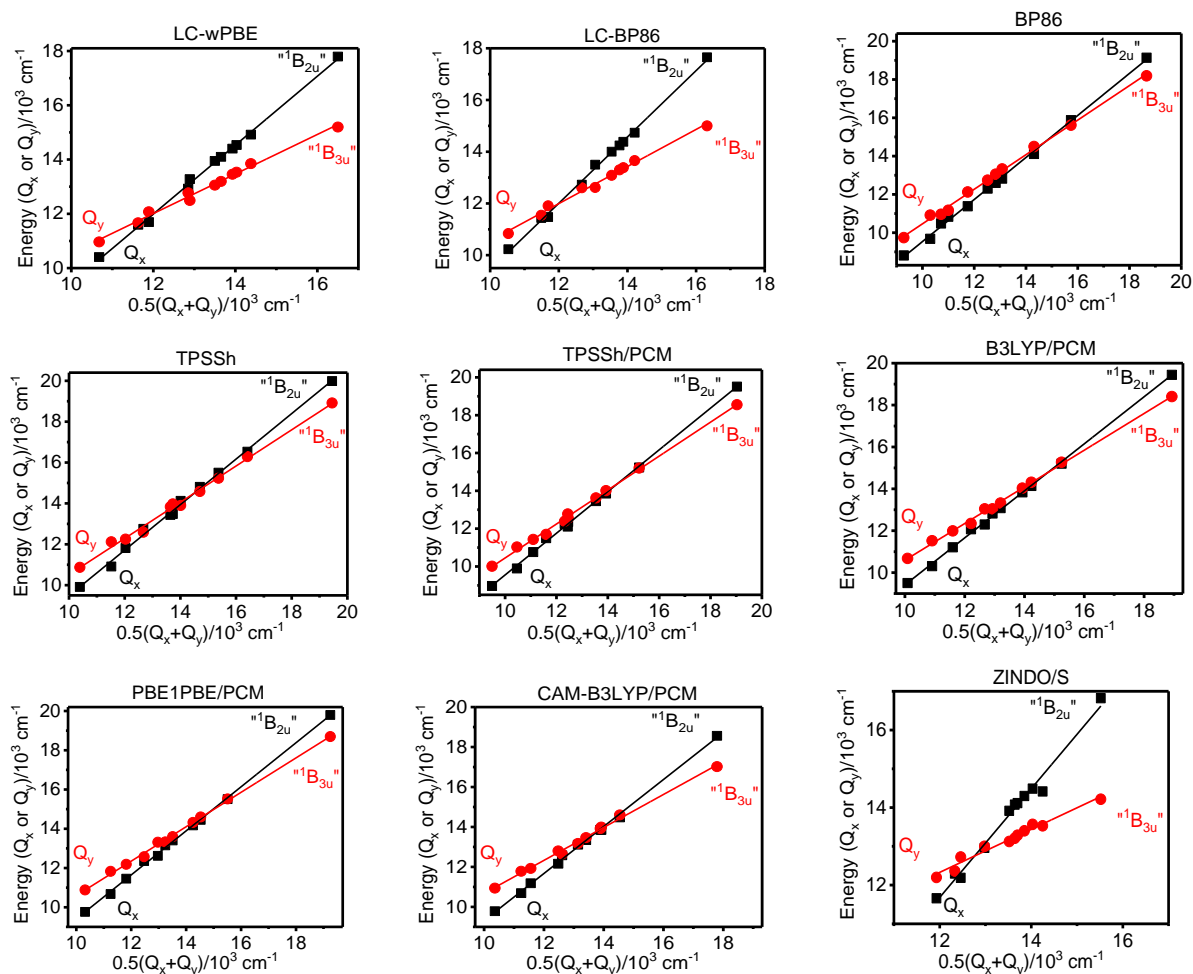


Figure 30. Calculated energies of the Q_x - or Q_y -bands vs. Q -center correlation diagrams for compounds **3.1-3.11** (The blue line represents the ideal agreement between theory and experiment).

General Trends in Predicted Q-Band Energies

Plots of the experimental versus calculated Q -band centre values were prepared to estimate trends of the Q -band energies as predicted by TDDFT and ZINDO/S calculations (Fig. 27) and the numerical fitting data is presented in Table 6. The energies of the Q -band centre were continuously overestimated with the PBE1PBE/PCM and TPSSh methods and all other methods

either under- or overestimated the Q-band centre compared to experimental data. The numerical analysis data presented in Table 4 suggests that the slopes, which are closest to unity and which have the smallest intercepts, were obtained using the CAM-B3LYP/PCM, LC-BP86, and LC-wPBE exchange-correlation functionals. The CAM-B3LYP/PCM, B3LYP/PCM, LC-BP86, and LC-wPBE ECFs provided accuracy greater than 0.05 eV ($\sim 400 \text{ cm}^{-1}$) for the Q-band centre energies of compounds **3.1-3.11**.

General Trends in Predicted Q-Band Splitting

Figure 28, with numerical analysis data listed in Table 7, shows the predicted Q_x - and Q_y -band splitting energies for the calculated TDDFT and ZINDO/S versus experimental data. The data clearly shows underestimated Q_x - and Q_y -band splitting energies for all exchange-correlation functionals except LC-BP86, LC-wPBE, and the semi-empirical ZINDO/S program. Also, only these three approaches provide the theoretically-expected $\text{H}_2\text{TAP} > \text{H}_2\text{Pc} > \text{H}_2\text{Nc} \sim 0 < \text{H}_2\text{Ac}$ Q_x - and Q_y -band splitting behaviour and it is predicted within 0.05 eV accuracy. The slope of the linear fit for the PBE1PBE/PCM, B3LYP/PCM, TPSSH/PCM, and BP86 ECFs nearly reaches unity; however, the median absolute deviations (MADs), predicted by TDDFT, are much higher than those for the LC-BP86 and LC-wPBE exchange-correlation functionals. Figure 29 and Table 8 provide a more detailed analysis of the Q_x - and Q_y -band energies as predicted by TDDFT and ZINDO/S. In line with previous work done by Kobayashi⁴⁹ and Nakatsuji⁴⁵, we defined the Q_y -band as the electronic transition dominated by a single-electron excitation from the “ a_{1u} ” occupied orbital (in D_{4h} notation), which in all cases is the HOMO, to one of the degenerate “ e_g ” orbitals, which is the

LUMO or LUMO+1 molecular orbital that contains electron density on the nitrogen atoms of the inner N-H (Figs. 31 and S100-S110) and the Q_x-band as the electronic transition dominated by a single-electron excitation from the “a_{1u}” occupied orbital (in D_{4h} notation), which in all cases is the HOMO, to one of the degenerate “e_g” orbitals, which is the LUMO or LUMO+1 molecular orbital that does not contain electron density on the nitrogen atoms of the inner N-H.

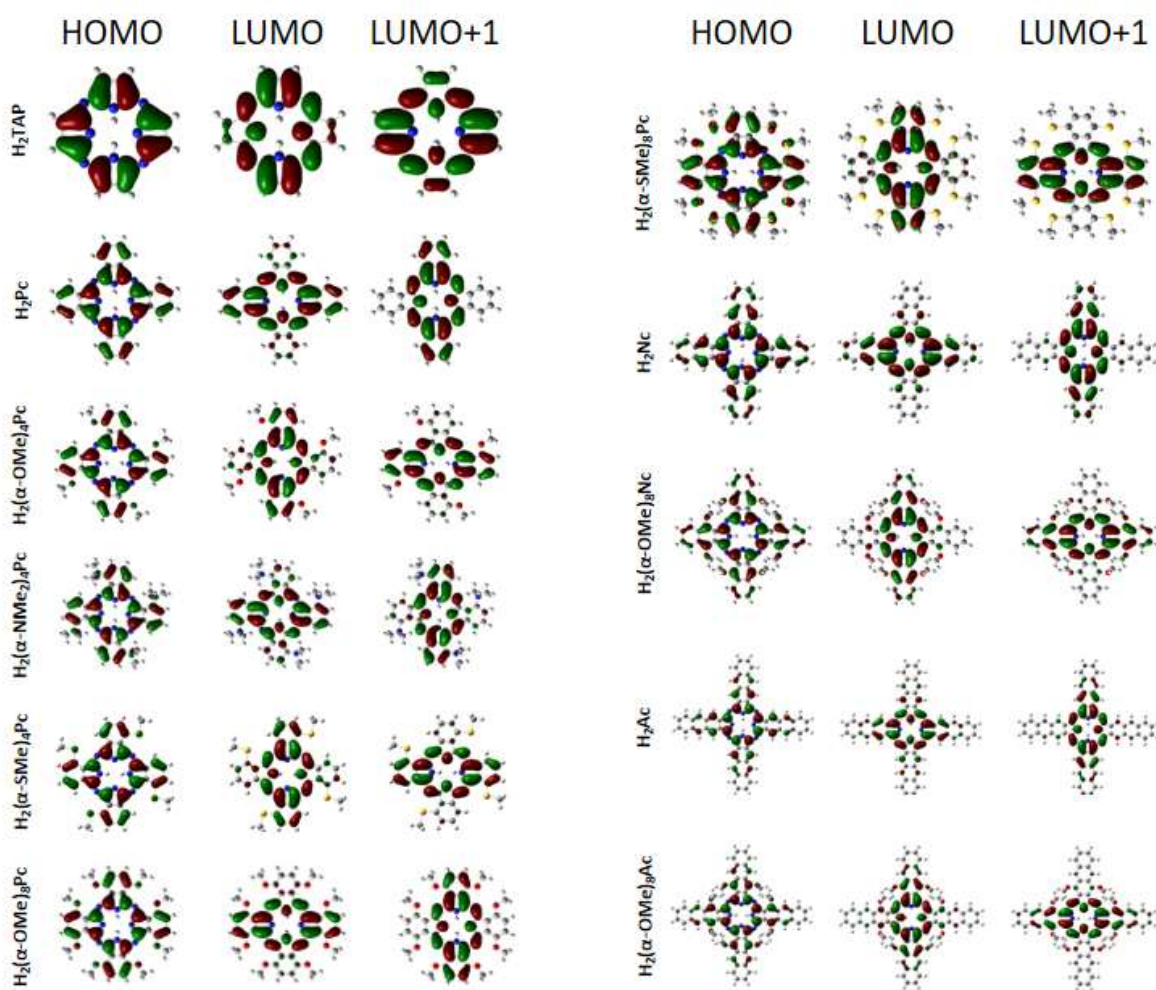


Figure 31. Frontier molecular orbitals of compounds **3.1-3.11**.

The performed TDDFT and ZINDO/S calculations indicate that only the energies of the Q_x - and Q_y -bands that were computationally predicted by the LC-BP86 and LC-wPBE exchange-correlation functionals are in good agreement (within 0.05 eV MAD) with experimental data. Also, the PBE1PBE/PCM and CAM-B3LYP ECFs correlate well with the energies of the Q_x - or Q_y -bands, respectively, but not both (Table 8). The experimental data available for metal-free Pcs suggests a linear decrease in the Q_x - and Q_y -band splitting energies going from H_2TAP to H_2Nc ; however, the experimentally observed Q_x - and Q_y -band splitting energy of $H_2Nc^{tBu} < H_2Ac^{Ph8}$ and $H_2(\alpha-Bu)_8Nc < H_2(\alpha-OiPent)_8Ac$ only can be explained by intercrossing of the “ 1^1B_{2u} ” and “ 1^1B_{3u} ” excited states in the metal-free Pcs and their analogues. Examples of this intercrossing behaviour were reported earlier for ZINDO/S and TDDFT calculations^{44,54} and compared to SAC-CI predictions^{45,55}. Agreeing well with previous calculations^{47,49,50,65,66} on similar metal-free phthalocyanines and their analogues, the TDDFT and ZINDO/S approaches predicted intercrossing of the “ 1^1B_{2u} ” and “ 1^1B_{3u} ” excited states (Fig. 30). The exchange-correlation functional has a predictable effect on the energy of such intercrossing. Interestingly, the CAM-B3LYP/PCM, PBE1PBE/PCM, B3LYP/PCM, and TPSSH/PCM ECFs predicted this intercrossing to occur nearest H_2Pc which is not in agreement with experimental data. Overall, the long-range corrected LC-BP86 and LC-wPBE methods provide the best agreement between experiment and theory when accurate (0.05 eV or better) prediction of the Q_x - and Q_y -band energies in metal-free Pcs and their analogues is required.

Description of Interligand Charge Transfer Bands for the α -Substituted Systems

It is well-known that phthalocyanines and their analogues that are α -substituted with electron-donating (-OR, -SR, and -NR₂) groups display broad, low-intensity transitions in their optical absorption spectra between the B- and Q-band regions and are attributed to substituent to macrocyclic core interligand charge-transfer character^{47,49,57,63,66}. The accurate and consistent prediction of this ICT region for the α -substituted metal-free Pcs and their analogues was investigated using TDDFT and ZINDO/S calculations. The focus of this sub-investigation hinged on the success of the long-range corrected functionals (LC-BP86 and LC-wPBE) at predicting the energies of the Q-band region; however, Fig. 32 clearly shows overestimation of the interligand charge-transfer region for these two methods and no transitions were predicted between the B- and Q-band regions. The full-size TDDFT-predicted UV-vis spectra along with the optimized coordinates and excited state energies from the TDDFT output files for all compounds are listed in the Supporting Information section.

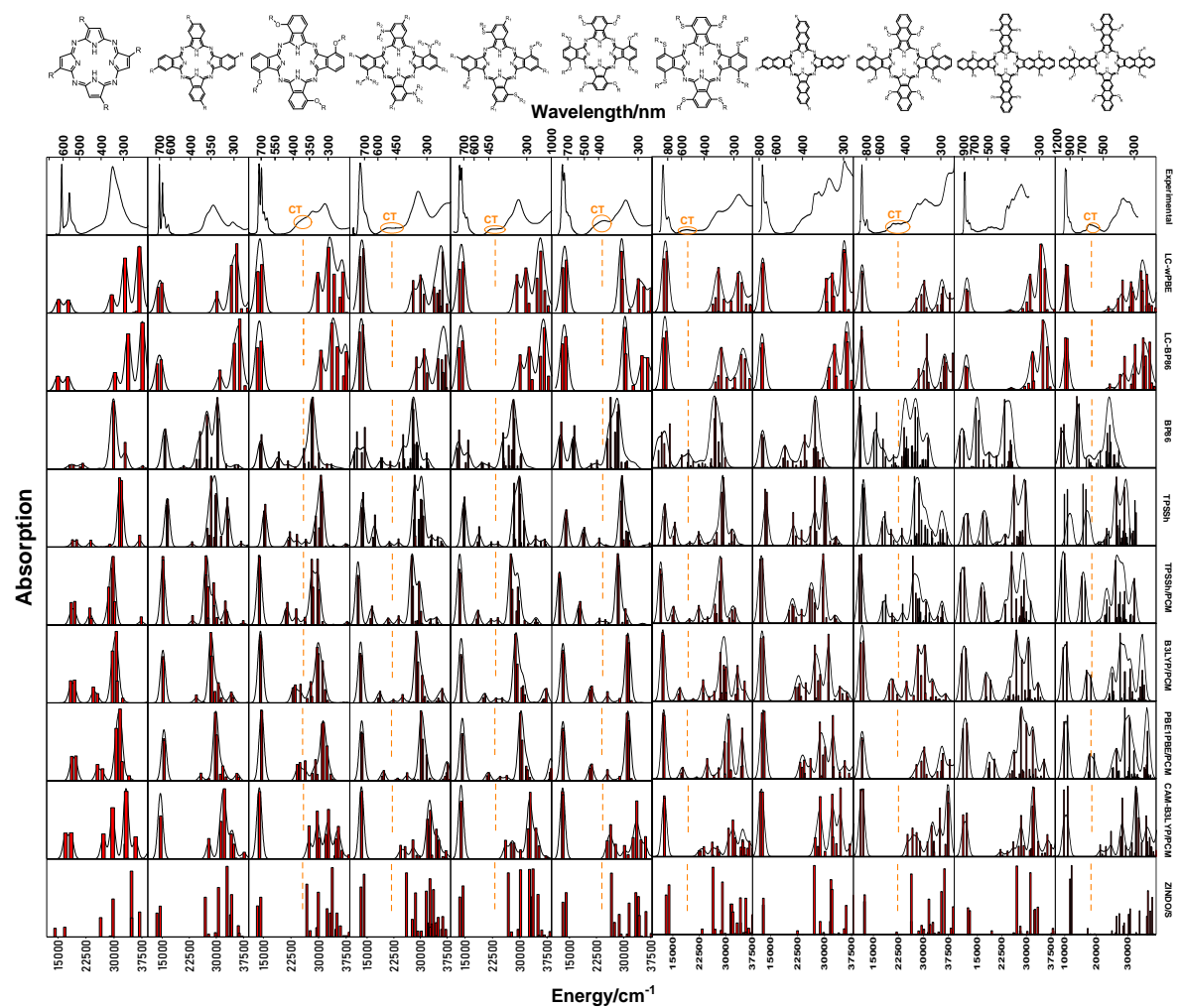


Figure 32. Experimental (top row) and computationally-predicted (rows 2-10) UV-vis spectra for compounds **3.1-3.11** (experimental spectra of compounds **3.10** and **3.11** were adapted from references 49 and 50).

The failure of the LC-BP86 and LC-wPBE exchange-correlation functionals to accurately predict the interligand charge-transfer regions for the α -substituted Pcs and their derivatives is not surprising since both ECFs contain a large amount of Hartree-Fock exchange which switches on for charge-transfer excitations. The ICT regions of the compounds of interest were underestimated by the pure GGA BP86 exchange-correlation functional which lead to substantial mixing of the macrocycle and charge-transfer based π - π^* transitions within the Q-band region. The energies of the interligand charge-transfer bands were continuously underestimated when using the TPSSh and TPSSh/PCM ECF; however, the charge-transfer and π - π^* transitions were better separated with these approaches (Fig. 32). These ICT region predictions significantly improved with the use of the hybrid CAM-B3LYP/PCM, PBE1PBE/PCM, and B3LYP/PCM exchange-correlation functionals and this was attributed to the previously established idea that 20-25% of Hartree-Fock exchange is required for a more accurate prediction of the interligand charge-transfer regions. Lastly, the energies of the ICT transitions of the α -substituted phthalocyanines and their analogues were severely overestimated when the ZINDO/S method was employed. Overall, the hybrid CAM-B3LYP/PCM, PBE1PBE/PCM, and B3LYP/PCM ECFs provided the best agreement between experiment and theory for the prediction of interligand charge transfer transitions from the α -substituents to the macrocyclic core.

Conclusions

The electronic structures of metal-free, unsubstituted and non-peripherally α -substituted with electron-donating groups, tetraazaporphyrins, phthalocyanines, naphthalocyanines, and

anthracocyanines were investigated and discussed using UV-vis, MCD, DFT, TDDFT, and semi-empirical ZINDO/S approaches with a heavy focus on Q-band energies and splitting of the Q_x- and Q_y-components. Intercrossing of the “1¹B_{2u}” and “1¹B_{3u}” excited states at ~800 nm in the optical absorption spectral region was indicated by experimental data. A broad scope of exchange-correlation functionals were used to calculate vertical excitation energies in the studied H₂TAPs, H₂Pcs, H₂Ncs, and H₂Acs. It was determined that the amount of Hartree-Fock exchange present in the exchange-correlation functional was directly correlated with the accuracy (< 0.05 eV) of the predicted Q_x- and Q_y-band energies and the ECFs that provided the best agreement between experiment and theory were LC-wPBE and LC-BP86. The predicted interligand charge-transfer transitions which were present in the 450-650 nm region of the experimental UV-vis spectra of the phthalocyanines and their analogues which were α-substituted with electron donating -OR, -SR, and -NR₂ groups were severely overestimated with the long-range corrected LC-wPBE and LC-BP86 exchange-correlation functionals and strongly underestimated by the pure GGA BP86 ECF. These energies of the ICT transitions were found to be better predicted by the hybrid B3LYP/PCM, PBE1PBE/PCM, and CAM-B3LYP/PCM exchange-correlation functionals with the B3LYP/PCM ECF providing the best simulation of these transitions. This study concludes that not a single exchange-correlation functional was able to accurately predict the Q_x- and Q_y-band energies and splitting in tandem with the interligand charge transfer transitions for the metal-free, unsubstituted and substituted phthalocyanines and their analogues.

Chapter 4: Evaluation of the Intramolecular Charge-Transfer

Properties in Solvatochromic and Electrochromic Zinc

Octa(carbazolyl)phthalocyanines

Summary

The electronic structures of zinc octacarbazolylphthalocyaninato (**4.1**) and octa(3,6-tert-butyl)carbazolylphthalocyaninato (**4.2**) complexes were studied using UV-vis and MCD spectroscopy as well as DFT and TDDFT methods. From the UV-vis and MCD data, the broad band observed in the 450-500 nm range for both compounds is indicative of interligand charge transfer (ILCT). Electrochemical and spectroelectrochemical measurements were performed to evaluate the redox properties of both compounds. The electrochemical data showed one quasi-reversible, single-electron oxidation and reduction process which was assigned as oxidation and reduction of the Pc core. Additionally, an irreversible multi-electron oxidation was observed at higher potential and was caused by simultaneous oxidation of the carbazole groups. The spectroelectrochemical data showed degradation of the Q-band and the emergence of two, new bands at energies lower than the Q-band as well as broad ILCT bands which developed at ~490 nm. These spectroelectrochemical transitions were typical for the formation of a Pc-centred cationic radical species and confirmed that the first oxidation is centred on the macrocycle.

Finally, TDDFT calculations using the PCM method correlated well with the experimental spectroscopy data.

Introduction

In the two previous chapters, two tetrapyrrolic molecule design approaches with a targeted photodynamic therapy application were presented. In chapter two, synthetic chlorophylls which mock the structure of their natural analogues were the focus. It was shown that these molecules only absorb at around 690 nm in the best case; however, the previously known resistance to melanin content interference of bacteriochlorins was the motivation for that project. In chapter three, the other commonly employed approach was used: extending the peripheral π -system, in addition to adding electron donating substituents onto the macrocyclic periphery. The results clearly favor the second approach of increasing peripheral bulk. Knowing this, the logical step forward is to pursue this second approach. From the work presented in chapter three, it was proven that with each increase in the degree of peripheral π -conjugation (via benzoannulation), the Q_y band was further red-shifted. In addition, adding electron donating substituents also helped to red shift the λ_{\max} band. The most prominent factor of adjusting peripheral bulk has to do with aggregation effects. Aggregation is common in phthalocyanines, with the most common type of aggregation being H-type, which features face-to-face molecular stacking and blue-shifted absorption signals⁶⁸. J-type aggregation features a staggered, side-by-side orientation of the molecules and red-shifted absorption signals. Typically, adding peripheral bulk to macrocycles will decrease the degree of aggregation since the bulky groups are more

likely to repel each other. This then begs the question: is there a limit to how much peripheral bulk can be added to a macrocycle or will continuously increasing the peripheral π -conjugation and adding bulky, electron-donating substituents further red-shift the λ_{max} band to longer and longer wavelengths? It turns out that in fact, there is a limit and this project explores this limit and addresses why it exists.

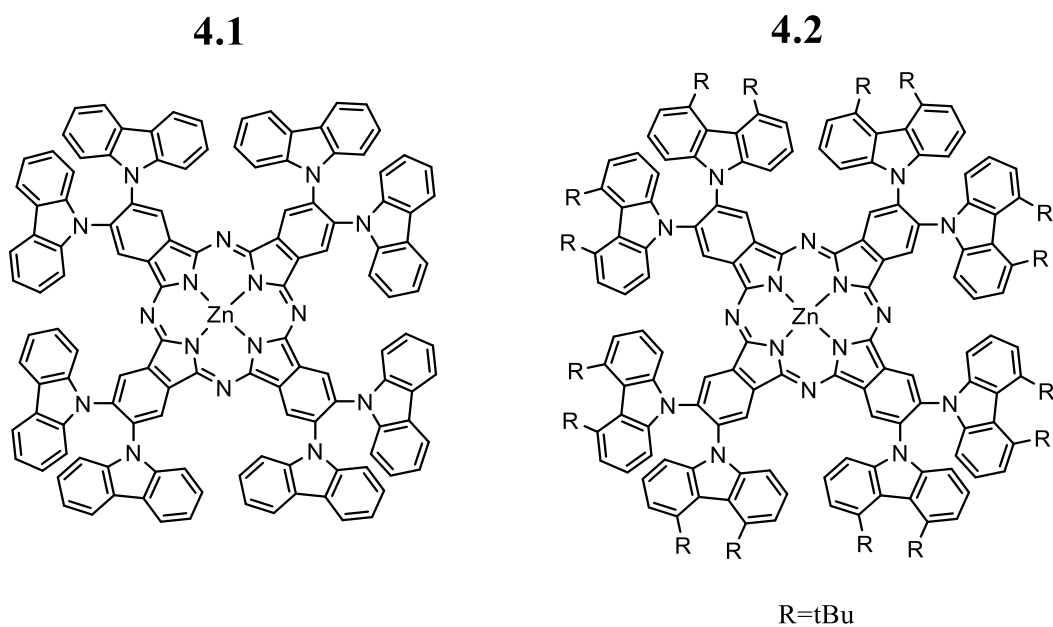


Figure 33. Structures of zinc octa(carbazoly)phthalocyanines **4.1** and **4.2**.

Shown in Fig. 33 are the structures of the zinc octa(carbazoly)phthalocyanines **4.1** and **4.2**. It's clear to see that these molecules are supremely bulky and using bulky peripheral carbazoles has been shown to prevent close self-association, even in the solid state⁶⁹. The structures presented in Fig. 33 contain the classical Pc core with a Zn metal centre. On the Pc periphery, eight carbazole groups have been incorporated. Carbazole derivatives historically have

had applications in medicinal chemistry and have been used as antimicrobial, anti-oxidative, antitumour, antihistaminic, anti-inflammatory, and psychotropic drugs⁷⁰. Also, due to their conjugated structure, carbazoles can potentially be used to further modify molecules for use in organic light emitting devices (OLEDs), photovoltaics, and display devices⁷¹. Finally, in the case of **4.2**, 16 tBu groups were added to the carbazole periphery to dramatically increase solubility.

Several techniques were employed in this body of work including DFT and TDDFT calculations, which were performed to predict energies of the frontier π -molecular orbitals, provide MO excited state images, and to simulate UV-vis spectra for correlative comparison. UV-vis and magnetic circular dichroism spectroscopies were used to provide additional information on electronic structures. Electrochemistry and spectroelectrochemistry were used to analyze charge transfer properties of the Pcs and when paired with TDDFT calculations, it was possible to determine from where on the molecule the charge was coming from and to where it was being transferred.

Experimental Details

Synthesis and Instrumentation

Methylene chloride solvent was purchased from commercial sources and dried using distillation and molecular sieves. The compounds **4.1** and **4.2** were synthesized as described previously⁵⁵ by Dr. Saad Makhseed at Kuwait University.

Electrochemical data were collected using a CH-620 electrochemical analyzer with Ag/AgCl pseudo-reference electrode and platinum working and auxiliary electrodes. Decamethylferrocene was used as an internal standard and reported potentials were corrected for the FcH/FcH⁺ couple in all cases. Spectroelectrochemical experiments were performed using a custom-made 1mm path length cell with a platinum mesh working electrode, platinum wire auxiliary electrode, and Ag/AgCl pseudo-reference electrode. All electrochemical experiments were performed using a 0.1M TBAP in DCM system, while a 0.3M TBAP in DCM system was used for all spectroelectrochemical measurements.

Computational Aspects

The CAM-B3LYP exchange-correlation functional²⁴ coupled with the LANL2DZ basis set for all atoms was used to optimize the starting geometries of all compounds. Frequency calculations confirmed the energy minima for the optimized geometries. For all single point DFT-PCM and TDDFT-PCM calculations, chloroform was used as a solvent and the polarized continuum model (PCM)¹⁸ was used to determine solvent effects. For each compound, the first 100 excited states were calculated using TDDFT-PCM calculations. All DFT and TDDFT calculations were performed with the Gaussian 09 software package¹⁶ and the molecular orbital analysis was administered using the Gaussview program¹⁷.

Results and Discussion

UV-Vis and MCD Spectra

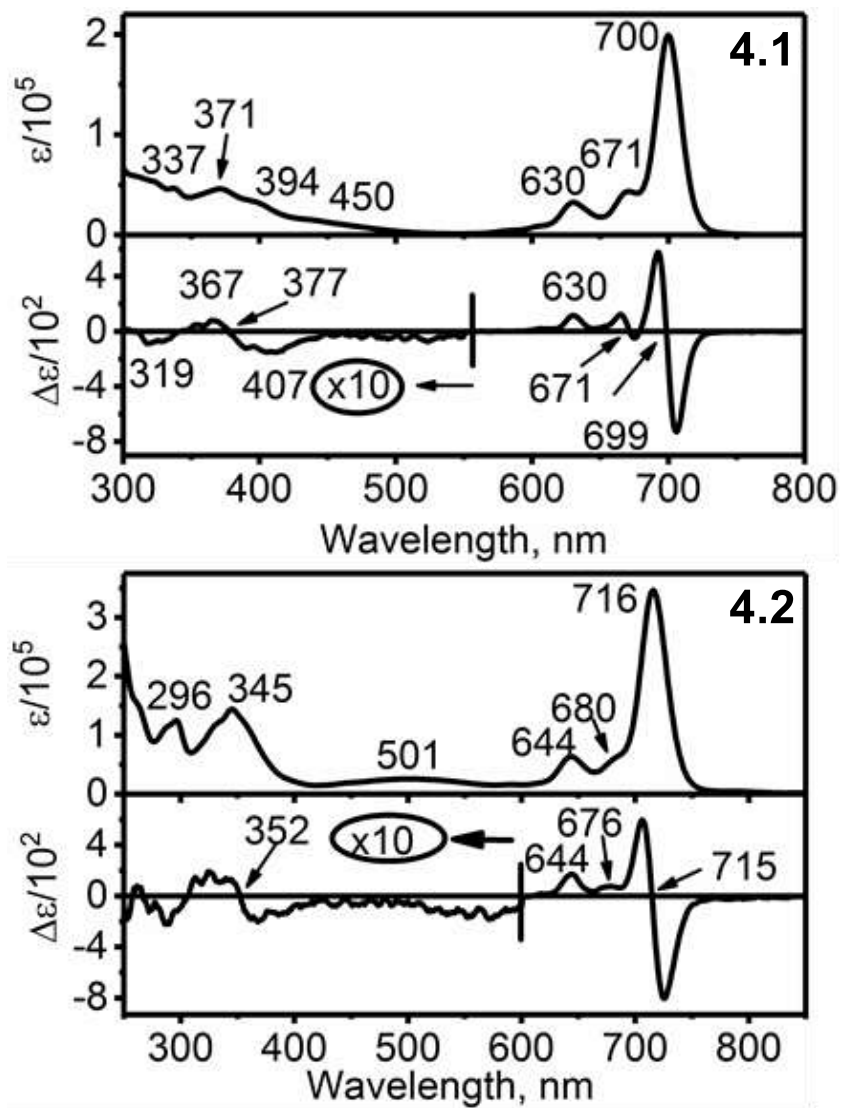


Figure 34. UV-vis and MCD spectra for 4.1 (above) and 4.2 (below).

The UV-vis and MCD spectra of **4.1** and **4.2** in DCM are shown in Fig. 34. In both cases, the UV-vis spectra are dominated by the classic Q- and B-bands. The Q-band in **4.1** (700 nm) and **4.2** (716 nm) is slightly shifted to a lower energy compared to unsubstituted **4.1** (678 nm)^{67,72}. In addition, the effect of the *tert*-butyl groups substituted onto the carbazole moieties was clearly noticeable by red-shifting of the Q-band of **4.2** when compared to its analogous complex **4.1**. Two vibronic satellites for the Q-band are also observable at higher energy in the UV-vis spectra of **4.1** and **4.2**. The B-band region is dominated by the series of overlapping transitions centered at ~350 nm, which is very common for phthalocyanine systems⁷³. Finally, a broad, low-intensity band at ~450 nm in **4.1** or ~500 nm in **4.2** was also observed in the corresponding UV-vis spectra. This band is absent in the unsubstituted or substituted with alkyl groups zinc phthalocyanines⁷⁴. The carbazole substituents in **4.1** and **4.2** have an electron-donating nature, and thus, it can be expected that energies of the carbazole-centered molecular orbitals (MOs) can be close to the energy of the phthalocyanine-centered highest occupied molecular orbital (HOMO) π -orbital. In this case, appearance of the low-energy carbazole-to-phthalocyanine interligand charge-transfer (ILCT) transitions are anticipated at higher than Q-band energies. Thus, the broad bands observed in the UV-vis spectra of **4.1** and **4.2** in the 450–500 nm region can be tentatively assigned to ILCT transitions. Such tentative assignments were further supported by MCD spectroscopy on compounds **4.1** and **4.2** (Figure 34). Indeed, MCD spectra of **4.1** and **4.2** in the Q-band region are dominated by the intense Faraday MCD A-term centered at 699 (**4.1**) or 715 nm (**4.2**). For both compounds, this A-term is accompanied by two positive MCD signals centered around vibronic satellites of the Q-band, and such spectroscopic signatures are very typical for the closed-shell phthalocyanine systems^{67,72,73,75}. In agreement with the other MCD spectra on

phthalocyanines^{67,72,73,75}, intensities of MCD transitions in the B-band region are approximately an order of magnitude lower compared to the Q-band region, but MCD Faraday A-terms can also be clearly defined in the B-band region, supporting fourfold effective symmetry of the phthalocyanine chromophore. Intensity of the MCD spectra of phthalocyanines **4.1** and **4.2** in the 450–500 nm region is very low, which correlates well with the tentative ILCT assignment of these transitions, and a similar situation was observed in phthalocyanine and porphyrinclathrocholate compounds^{75,76}.

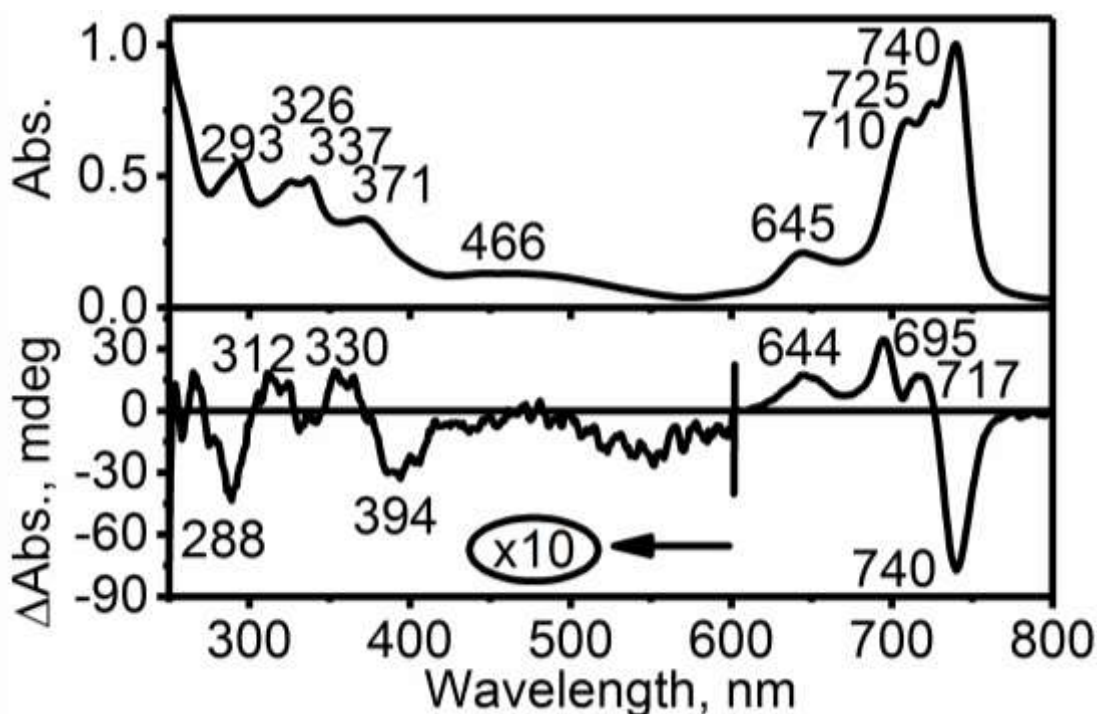


Figure 35. UV-vis and MCD spectrum for protonated **4.1**.

The presence of eight electron-donating carbazole groups in **4.1** and **4.2** should increase basicity of the *meso*-nitrogen atoms in these compounds and make them susceptible to

protonation with a variety of acids. Indeed, even a short-time exposure of **4.1** to organic acid vapors results in its UV-vis spectrum shown in Figure 35. The UV-vis spectrum of protonated **4.1** has three clear peaks in the Q-band region centered at 740, 725, and 710 nm, while an addition of organic base (NEt_3) results in restoration of the Q-band of initial complex **4.1** at 700 nm. Incremental red-shift of the Q-band in phthalocyanines upon stepwise protonation of the *meso*-nitrogen atoms is well-documented⁷⁷⁻⁷⁹. Usually, protonation of the first two *meso*-nitrogen atoms can be achieved with a variety of organic or inorganic acids, while protonation of the third and fourth *meso*-nitrogen atom requires a strong organic or inorganic acid. It is interesting that the nitrogen atoms at the carbazole groups remain intact upon protonation since they were expected to be a possible site of protonation, as the broad and low-intensity ILCT band undergoes just a small, low-energy shift, and similar protonation behaviour was observed in the case of α -alkoxy-substituted (non-peripheral positions) phthalocyanines⁸⁰. Since protonation of the *meso*-nitrogen atoms in **4.1** and **4.2** should reduce the four-fold effective symmetry of the phthalocyanine macrocycle to two-fold, the excited-state degeneracy of **4.1** and **4.2** should be relaxed, which transforms MCD Faraday *A*-terms to *B*-terms. Indeed, the Q-band at 740 nm observed in the UV-vis spectrum of protonated **4.1** correlates well with the Faraday MCD *B*-term centered at 740 nm. Similar to **4.1** and **4.2**, MCD intensity, which corresponds to the broad band centered at 466 nm, is very low, which correlates well with its assignment as an ILCT band.

Redox Properties of Phthalocyanines 4.1 and 4.2

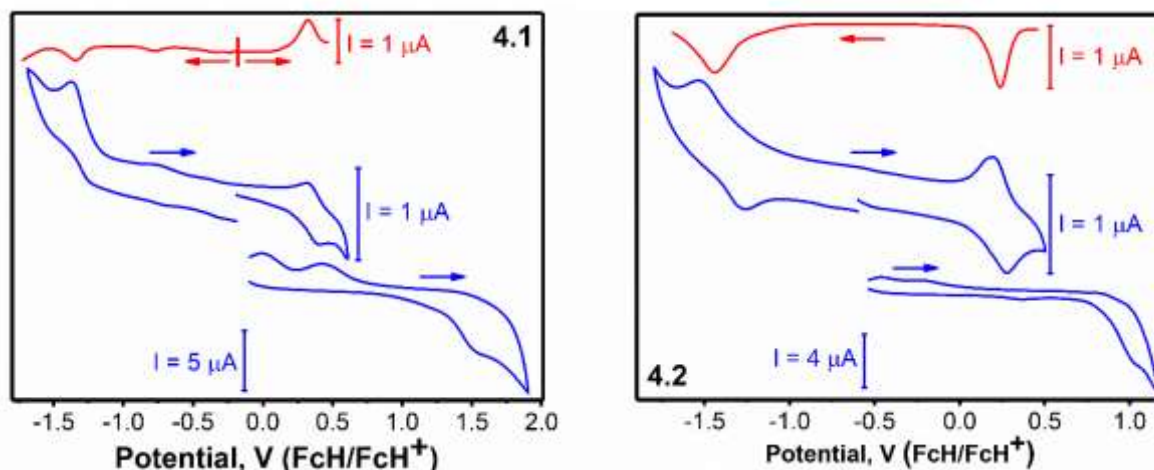


Figure 36. CV and DPV data on complexes **4.1** and **4.2** using a 0.1 M TBAP in DCM system.

Cyclic voltammetry (CV) and differential pulse voltammetry (DPV) were used to investigate the electrochemical behaviour of **4.1** and **4.2** using a 0.1M TBAP in DCM system (Fig. 36). Within the electrochemical window, one quasi-reversible single-electron reduction and oxidation process was observed for both compounds. At higher potentials, one irreversible multi-electron oxidation process was observed for **4.1** and **4.2**. This irreversible multi-electron process was assigned to a simultaneous oxidation of the carbazole groups and the reversible processes were both hypothesized to be due to redox activity of the Pc core.

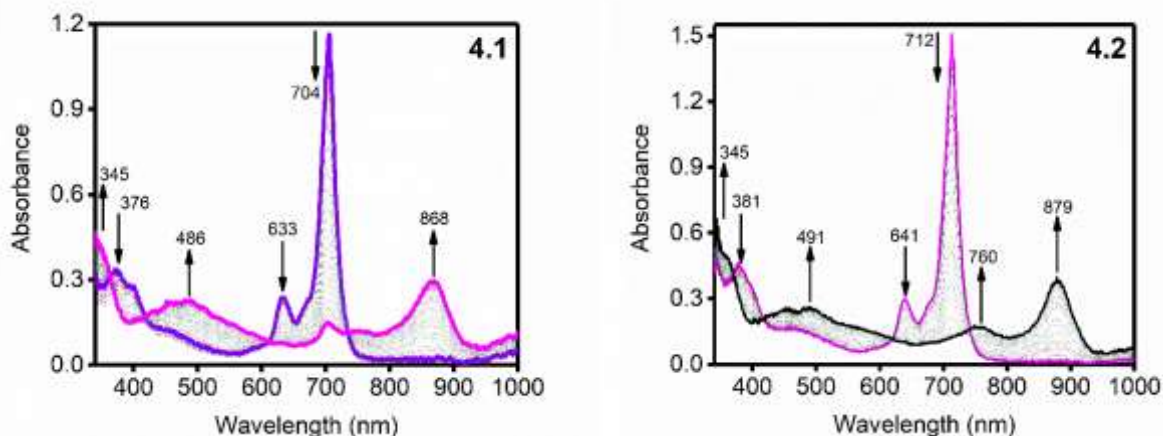


Figure 37. Spectroelectrochemical oxidation data for compounds **4.1** and **4.2** using a 0.3 M TBAP in DCM system.

To further investigate these redox processes and their proposed assignments, spectroelectrochemical oxidations of **4.1** and **4.2** using a 0.3 M TBAP in DCM system were performed (Fig. 37). Both compounds underwent very similar transformations of their UV-vis spectra as increased potential was applied. The Q-band for **4.1** and **4.2** decreased in intensity and two new bands developed for both compounds. These new bands that developed were at 753 and 868 nm for **4.1** and 760 and 879 nm for **4.2**. Broad ILCT bands started to develop at 486 and 491 nm for **4.1** and **4.2**, respectively. This is characteristic of the formation of a Pc-centred cation-radical, confirming the assignment of the first oxidation to the phthalocyanine core.

The reversibility of the oxidation process in protonated **4.1** was studied; however, upon addition of DCM to the electrolyte solution, protonated **4.1** was transformed into neutral **4.1**. This indicates very low interaction energy between the *meso*-nitrogen atoms and their

corresponding protons. It is hypothesized that some of the DCM molecules absorb the weakly associated protons on the Pc core which eventually converts a portion of the DCM to chloromethane. The redox activity of the protonated and non-protonated **4.1** compounds were studied using chemical oxidation titrations as shown in Fig. 38. Using 2,3-dichloro-5,6-dicyano-1,4-benzoquinone (DDQ) oxidant, stepwise oxidation of protonated and non-protonated **4.1** led to a mixture of monomeric and aggregated cation-radical compounds based on the appearance of two NIR bands after oxidation. The UV-vis-NIR spectra using spectroelectrochemical oxidations and chemical oxidations are nearly identical, indicating elimination of the N_{meso} -H bonds after the Pc core was oxidized.

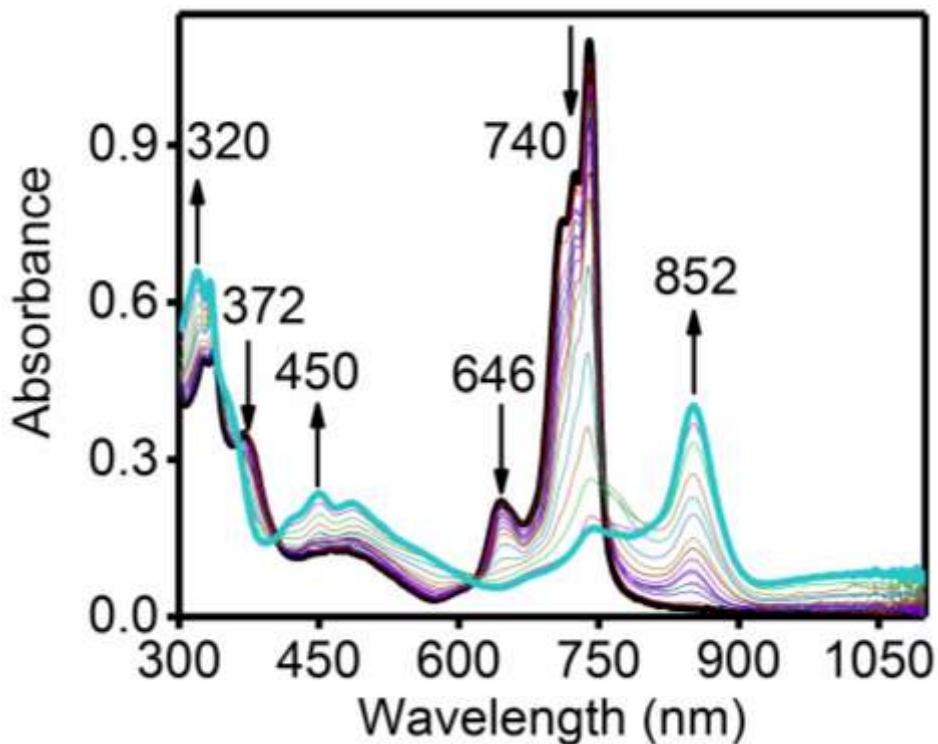


Figure 38. Chemical oxidation of protonated **4.1** using DDQ in DCM.

DFT and TDDFT Calculations

DFT and TDDFT calculations were used to explore the electronic structures and excitation energies of **4.1** and **4.2**. The PCM method¹⁸ using chloroform as a solvent was used to correlate experimental and simulated UV-vis spectra. Shown in Fig. 39 are the predicted DFT-PCM frontier molecular orbital energy diagrams for **4.1** and **4.2**.

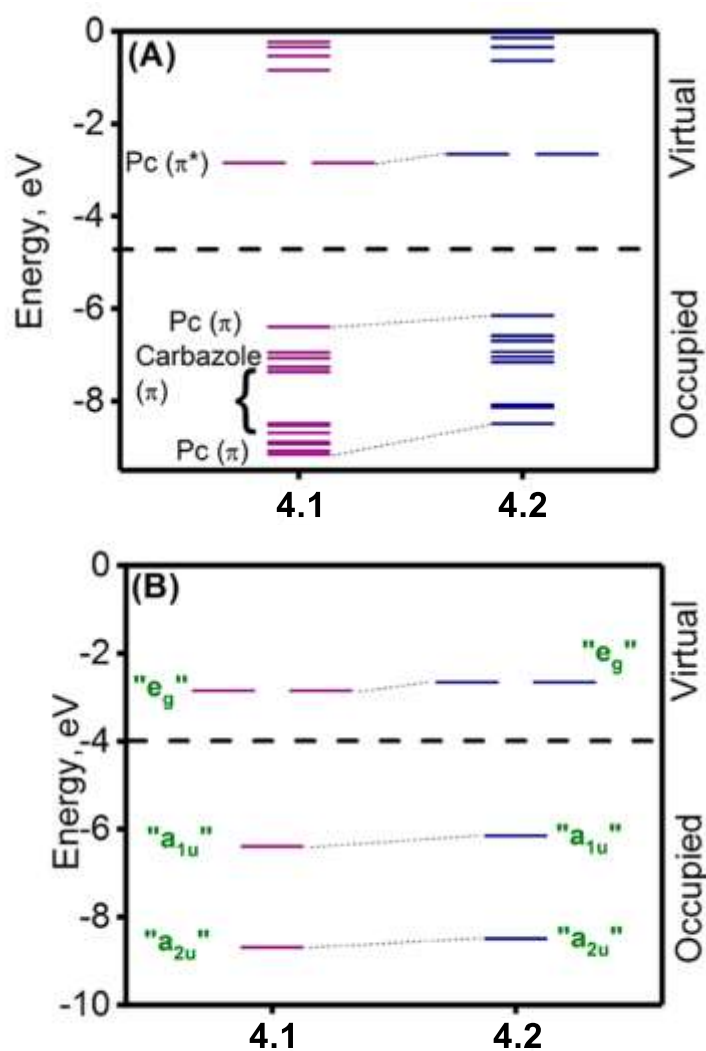


Figure 39. Predicted DFT-PCM molecular orbital energy level diagram for **4.1** and **4.2**. (A) Frontier MO energy levels; (B) select Gouterman's MO energy levels.

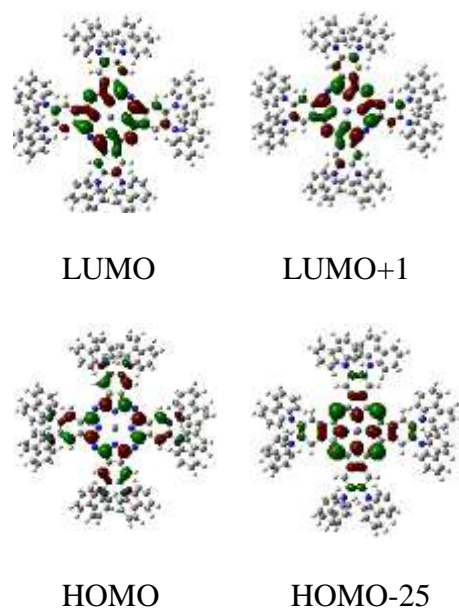


Figure 40. Gouterman's molecular orbitals of **4.1** calculated at the CAM-B3LYP/LANL2DZ level.

The DFT-predicted HOMO best resembles Gouterman's a_{1u} orbital⁸¹ with the largest contribution coming from the α - and β -pyrrolic carbon atoms in both **4.1** and **4.2**. As predicted by DFT, the HOMO-1 to HOMO-24 orbitals are centered at the carbazole moieties and the HOMO-25 orbital resembles Gouterman's a_{2u} orbital. The largest contributions from the HOMO-25 come from the *meso*- and inner-nitrogen atoms on the Pc core. Figure 39 shows the orbitals which are closely spaced in energy and there is only a small energy difference between the Gouterman's a_{1u} and a_{2u} orbitals. Also resembling the classic Gouterman's e_g pair are the DFT-predicted LUMO and LUMO+1 in **4.1** and **4.2**, which have large contributions from the α - and β -pyrrolic carbon atoms, and also from the inner- and *meso*-nitrogen atoms and phenyl ring in the Pc core (Fig. 40). The spectroscopic and electrochemical data for **4.1** and **4.2** correlates nicely with their DFT-predicted electronic structures. Specifically, elucidation of the DFT data indicates that the first

oxidation and reduction are centered on the Pc core while the second multi-electron oxidation event is centered on the carbazole groups. Additionally, as predicted by DFT, the NIR region of the absorption spectrum features a large number of ILCT transitions and the excited state that is lowest in energy is likely to be Pc-centered.

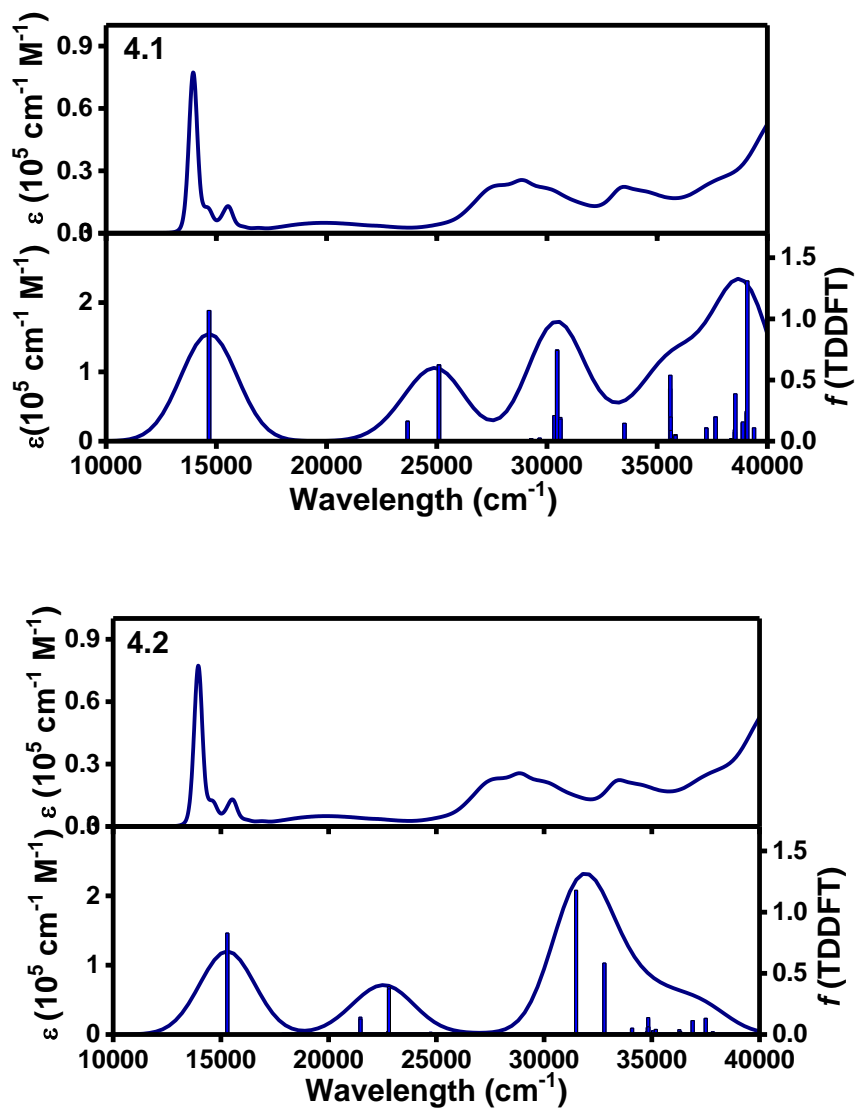


Figure 41. Experimental (upper) and computationally simulated (lower) UV-vis spectra for **4.1** and **4.2**.

Shown in Fig. 41 are the experimental and TDDFT-PCM simulated UV-vis spectra for **4.1** and **4.2**. Generally, there is good agreement between these spectra and the proposed electronic structures. In both **4.1** and **4.2** the first excited state is doubly degenerate as predicted by the TDDFT data. This first excited state is largely dominated by single-electron HOMO \rightarrow LUMO, LUMO+1 excitations. A large quantity of ILCT bands largely comprised of single-electron promotions from the occupied carbazole-centered HOMO-1 to HOMO-24 molecular orbitals to the unoccupied carbazole and Pc centered orbitals were predicted by the TDDFT calculations. Large contributions from the strongest transitions in the B-band region originating from HOMO-25 \rightarrow LUMO, LUMO+1 were also elucidated from the TDDFT data. In this project, the TDDFT calculations definitively indicate Pc-centered excited states which are low in energy followed by the predicted ILCT electronic transitions.

Conclusions

The electronic structures of zinc octacarbazolyphthalocyaninato (**4.1**) and octa(3,6-tert-butyl)carbazolyphthalocyaninato (**4.2**) compounds were analyzed using UV-vis and MCD spectroscopies as well as DFT and TDDFT calculations. The absorption spectroscopy data indicates broad bands in the 450-500 nm range which correspond to ILCT transitions. Electrochemical and spectroelectrochemical methods were used to explore the redox properties of **4.1** and **4.2**. These methods suggest that the reversible first oxidation and reduction events are Pc-centered and the second irreversible oxidation is centered over the carbazole groups. Experimental and TDDFT-predicted spectroscopic data were correlated and this data suggests

that the HOMO and LUMO orbitals are Pc-centered while the HOMO-1 to HOMO-24 orbitals are centered on the carbazole groups. The TDDFT calculations as well as the many observed ILCT transitions in the high-energy region of the UV-vis spectrum confirmed the first and second excited states to be phthalocyanine-centered.

Chapter 5: Elucidation of the Electronic Structure of Water-Soluble Quaternized *meso*-Tetrakis(3-pyridyl)bacteriochlorin Derivatives by Experimental and Theoretical Methods

Summary

The electronic structures of three tetracationic *meso*-tetrakis(3-pyridyl)bacteriochlorins (**5.1**, **5.2**, and **5.3**) were evaluated using spectroscopic (UV-vis and MCD) and computational (DFT and TDDFT) techniques. The DFT and TDDFT-PCM calculations provided simulated UV-vis spectra, energy levels of the molecular orbitals, and images of electron density on the MOs in each excited state. The UV-vis and MCD spectra of **5.1-5.3** show a split Soret band between 350-400 nm and significantly large splitting between the Q_x- and Q_y-bands in the visible to NIR spectral region. The most important experimentally observed features in the UV-vis and MCD spectra of **5.1-5.3** were explained by Goutermann's four-orbital model and were validated with the DFT and TDDFT calculations. Specifically, the observed reversal of MCD sign sequence in the visible to NIR region

correlates well with the $\Delta\text{HOMO} < \Delta\text{LUMO}$ relationship which was predicted by DFT. In addition, experimentally observed splitting of the Soret band and significantly large splitting between the Q_x - and Q_y -bands were accurately predicted by TDDFT. From this analysis, we have shown that the quaternized groups in water-soluble bacteriochlorins formed by quaternization of the nitrogen atom in free-base tetra-(3-pyridyl)bacteriochlorins have a negligible influence on their electronic structure. In general, the electronic structure and spectroscopy of quaternized bacteriochlorins are very similar to previously studied *meso*-aryl bacteriochlorins.

Introduction

Bacteriochlorins are a type of tetrahydroporphyrin, which are tetrapyrrolic macroheterocyclic 22 π -electron compounds⁸². As introduced in chapter 2, bacteriochlorins contain two opposing reduced or hydrogenated C_β - C_β bonds (Fig. 12). Bacteriochlorins are highly sought after due to their intense absorption in the optical window of tissue (650-940 nm), making them appropriately suitable candidates for use as photochemotherapeutics for photodynamic therapy (PDT) of cancer or as photosensitizers for treating skin disease⁸³⁻⁸⁸, in addition to their use as antimicrobial agents⁸⁹. Bacteriochlorins are particularly important for their use in PDT due to their known superior resistance to melanin content interference. The other novelty of bacteriochlorins is that they are known to exist as naturally occurring molecules, typically produced by organisms in the form of photosynthetic pigments or anoxygenic photosynthetic bacteria. For this reason, there is more hope for biological cohesiveness between the

photochemotherapeutic material and organic cells and systems compared to purely synthetic alternatives.

The *meso*-aryl-bacteriochlorins are synthesized from their parent chlorins or porphyrins using several approaches such as condensation of dihydrodipyridines (Lindsey's method)⁹⁰⁻⁹⁵, cycloaddition reactions^{96,97}, hydroxylation with catalytic OsO₄⁹⁸⁻¹⁰³, reduction via diimide (Whitlock's method)¹⁰⁴⁻¹¹⁰, catalytic hydrogenation¹¹¹, or reduction using elemental sodium in an alcohol system¹¹². Largely, the issue with these synthetic methods is that the bacteriochlorins produced are hydrophobic, which severely limits their utility as photosensitizers meant to be incorporated into biological systems. Since the main application of bacteriochlorins is photosensitizers for PDT, it is critical to impart water solubility into these molecules in the design process.

To make bacteriochlorins water-soluble, two approaches are employed. The first is by means of chemical methods such as quaternization or sulfonation of the bacteriochlorin molecule. The quaternization method essentially adds quaternary ammonium cations to the periphery of the bacteriochlorin and the sulfonation approach adds sulfonic acid functional groups to the molecule. The second method of imparting water-solubility to bacteriochlorins can be achieved by using solutions of surface active compounds such as Pluronic 268 or Cremophor EL. When water-soluble emulsions of bacteriochlorins are added to these solutions, the resulting bacteriochlorins are now of water-soluble character. Cremophor EL is a nonionic surfactant used as a formulation vehicle to induce solubility of pharmaceuticals that have poor water-solubility.

Pluronic 268 is a polymer which is also a nonionic surfactant and when bound to a drug, has the ability to imbed itself into micelles to promote uptake of hydrophobic compounds.

There have been a few recent successes in the synthesis of water-soluble tetracationic *meso*-tetrakis(1-methyl-3-pyridyl)bacteriochlorin tetratosylates¹¹³⁻¹¹⁶ and sulfonated *meso*-aryl-bacteriochlorins^{105-108,117}. These molecules showed great potential for clinical uses as they demonstrated large photoinduced activity *in vivo* and *in vitro*. Such compounds are hopeful prospects for use as near-infrared photosensitizers for PDT application. An expanded range of utility is achieved with tetracationic bacteriochlorins as they possess photodynamic reactivity to degrade Gram-positive and Gram-negative bacteria^{118, 119}.

Metallation of the porphyrinoid centre using different metals has recently been an area of focus in the field of molecule design of photosensitizers for PDT application¹²⁰⁻¹²². The introduction of a metal centre to a porphyrinoid changes its photophysical properties and electronic structure. Metallation of bacteriochlorins causes bathochromic red-shifting of the intense and longest wavelength λ_{max} -band in the NIR region of the UV-vis spectrum. An example of such a compound was the incorporation of a palladium atom into the centre of bacteriopheophorbide A, a bacteriochlorin derived from nature¹²³. The resulting molecule is a very useful NIR photosensitizer and its clinical application been approved in several countries. The idea of attaining metallated bacteriochlorins is very attractive to porphyrin chemists as only a few of these compounds have been synthesized.

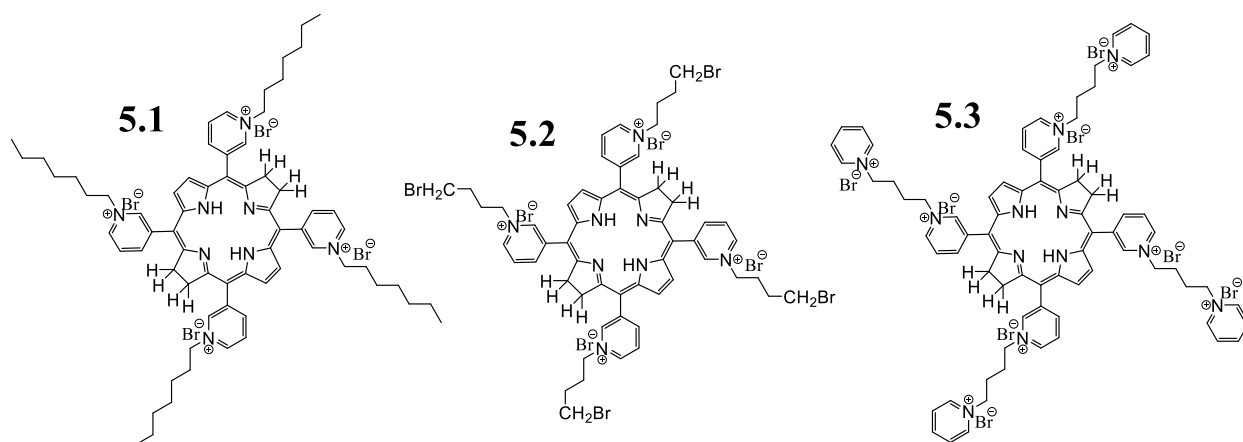


Figure 42. Structures of water-soluble *meso*-tetrakis(3-pyridyl)bacteriochlorin derivatives.

Shown in Fig. 42 are the structures of the water-soluble *meso*-tetrakis(3-pyridyl)bacteriochlorin derivatives reported on herein. The approach used to impart water-solubility into these complexes was quaternization of the pyridine groups to achieve tetracationic salts. In each case, the cationic centres are stabilized by anionic halide counterions as a result of dissociative exchange involving the halogenated reactants and the macrocycle. The experimental methods include aspects of characterization and spectroscopic analysis using UV-vis and MCD, and the electronic structures of the bacteriochlorin systems were described using DFT and TDDFT-PCM calculations.

Experimental Details

Synthesis and Instrumentation

Ethanol solvent was purchased from commercial sources. Three tetracationic *meso*-tetrakis(3-pyridyl)bacteriochlorin (**5.1**, **5.2**, and **5.3**) samples were synthesized and described previously⁸² by Dr. Elena Makarova and Dr. Eugeni Lukyanets at the Organic Intermediates and Dyes Institute in Moscow.

UV-vis data were obtained with a Jasco V-670 spectrophotometer using either ethanol or water solvent. The MCD data were obtained with an OLIS DCM 17 CD spectropolarimeter using a permanent 1.4 T DeSa magnet. For each sample, two spectra were recorded: one using a parallel field and the other using an antiparallel field. The spectral intensities were expressed as molar ellipticity per T^2 .

Computational Aspects

All TDDFT calculations were performed using the Gaussian 09 software package¹⁶. The starting geometries were optimized using the TPSSH exchange-correlation functional. To minimize computational cost, the ligand arms were shortened to omit sections that don't contribute to the electronic structure. The equilibrium geometries were confirmed with frequency calculations and more specifically, by the absence of imaginary frequencies. All atoms were modeled using the 6-31G(d) basis set and for the TDDFT calculations, the solvent effects

were calculated using the PCM approach¹⁸ with DCM as a solvent. The QMForge²⁵ DFT analysis program was used to compile molecular orbital contributions from single-point calculations.

Results and Discussion

The UV-vis and MCD spectra of **5.1-5.3** shown in Fig. 43 show very little deviation from each other.

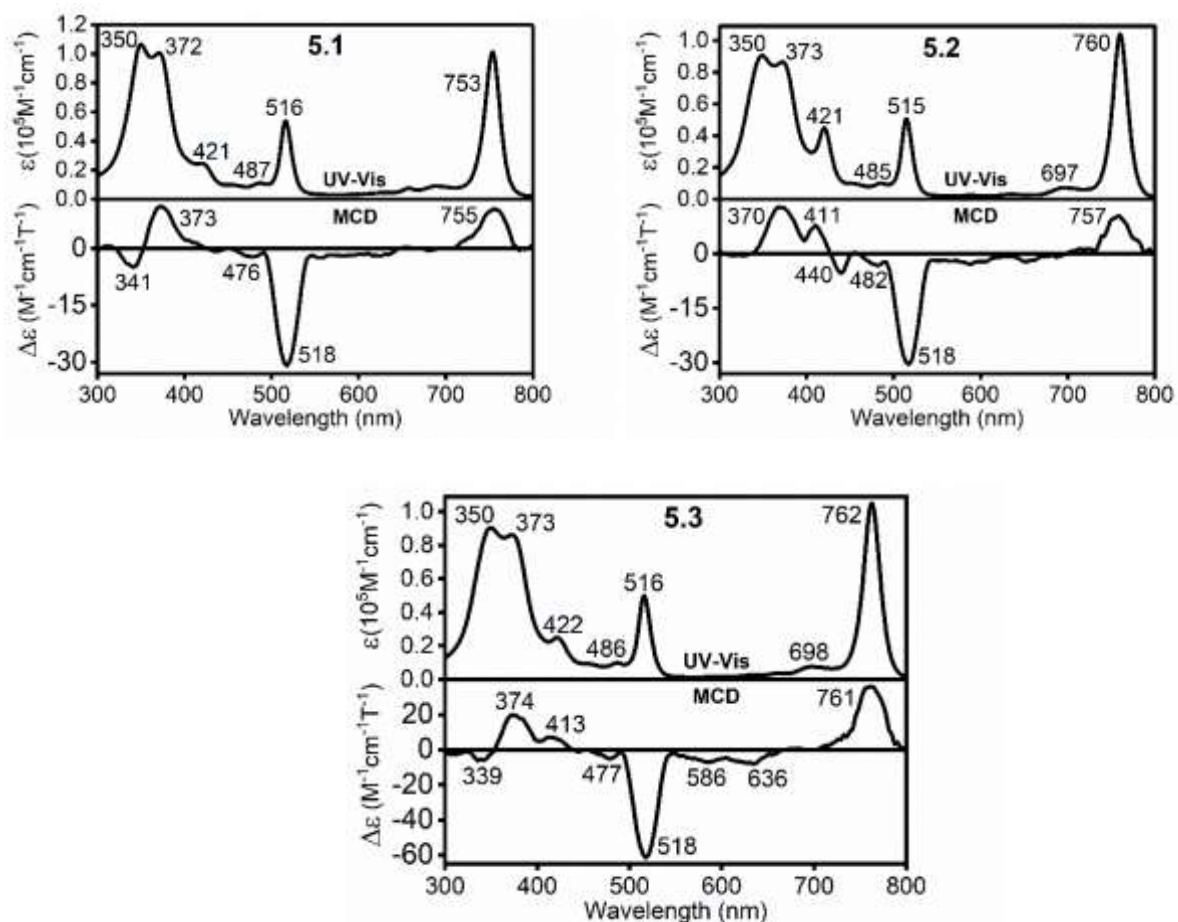
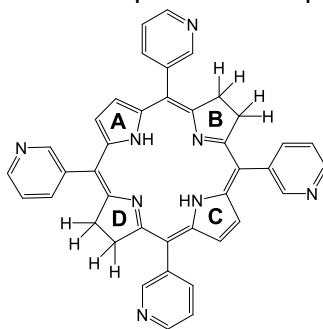


Figure 43. Experimental UV-vis (top) and MCD (bottom) spectra of **5.1-5.3**.

The influence of the peripheral substituents used for quaternizing the *meso*-pyridine moieties on the bacteriochlorin π -system was expected to be negligible, so it's no surprise that the UV-vis and MCD spectra of **5.1-5.3** are so similar. Specifically, classic bacteriochlorin Q_x- and Q_y-bands were observed for all bacteriochlorin compounds and are represented as peaks at 515 and 754-762 nm, respectively. These two characteristic bands are associated with a negative MCD signal present at 518 nm and a positive MCD signal observed between 754 and 761 nm. Both signals are assigned as MCD Faraday *B*-terms after taking into consideration the low symmetry of these bacteriochlorins and similar large splitting was observed with other bacteriochlorin systems investigated to date^{124,125}. In each case, the Soret band shows clear splitting with signals at ~372 and ~350 nm which are associated with negative and positive Faraday *B*-terms in their corresponding MCD spectra. The experimentally observed positive to negative MCD signal pattern in terms of increasing energy for the ~750 and ~515 nm absorption bands indicates a $\Delta\text{LUMO} > \Delta\text{HOMO}$ relationship, according to the perimeter model⁷⁻¹⁰. Bacteriochlorins substituted with aryl groups at *meso* positions characteristically possess such a ΔLUMO and ΔHOMO relationship³⁹. Interestingly, for the oxobacteriochlorins that originated from the octaethylporphyrin core, the opposite relationship was observed²⁷⁻³⁸.

Taking the negligible effect of the quaternizing groups into consideration, a series of DFT and TDDFT calculations were performed on the parent tetra-(3-pyridyl)bacteriochlorin in order to correlate the electronic structures of **5.1-5.3** with their experimentally observed spectroscopic signatures. To facilitate the electronic structure analysis, the reference bacteriochlorin (**5.4**) was optimized with the highest possible D₂ point group. Table 9 lists the DFT-predicted frontier orbital compositions and Fig. 44 shows the energy diagram and frontier orbital profiles.

Table 9. Frontier molecular orbital compositions for parent **5.4** as predicted by DFT.



MO	Energy/eV	A	B	C	D	meso-C	Pyridine
HOMO-1	-6.344	9.05	10.64	9.05	10.64	46.75	13.88
HOMO	-5.681	23.64	22.59	23.64	22.59	5.68	1.86
LUMO	-1.991	18.07	12.10	18.07	12.10	27.97	11.69
LUMO+1	-0.371	17.11	22.39	17.11	22.39	10.07	10.92

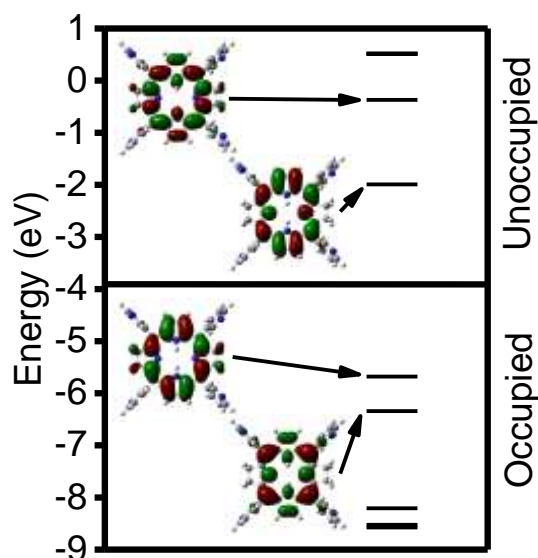


Figure 44. Energy level diagram and frontier molecular orbitals of *meso*-(3-pyridyl)bacteriochlorin **5.4**.

The Goutermann's orbitals^{12,13} as predicted by DFT were found to be the LUMO and LUMO+1 (e_g pair in D_{4h} framework), HOMO-1 (a_{2u} type in D_{4h} framework), as well as HOMO (a_{1u} type in D_{4h} symmetry framework). In the MCD spectra of **5.1-5.3**, the experimentally observed

sign sequence of the Q_x - and Q_y -bands correlates well with the DFT-predicted Δ HOMO in the tetra-(3-pyridyl)bacteriochlorin **5.4** species being much smaller (3365 cm^{-1}) than the DFT-predicted Δ LUMO (10168 cm^{-1}). The experimental and TDDFT-predicted UV-vis spectra of **5.1** and **5.4** are shown in Fig. 45.

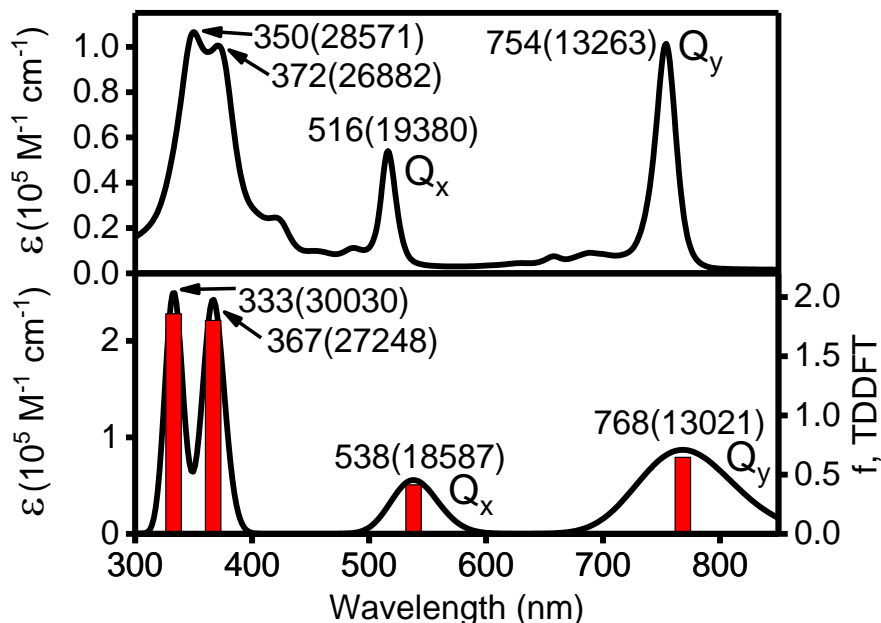


Figure 45. Experimental (top) and TDDFT-predicted (bottom) UV-vis spectra of **5.1** and **5.4**, respectively.

Overall, there is good correlation (less than 25 nm deviation in major bands) between the TDDFT-predicted spectrum and the experimental data. Specifically, four excited states (excited states 1, 2, 3, and 9) dominate the TDDFT-predicted spectrum. Table 10 shows that excited state 1 was predicted at 664 nm and correlates accurately with the experimentally observed Q_y -band at $\sim 750\text{ nm}$.

Table 10. Expansion coefficients, excitations, and excited state energies for the reference bacteriochlorin **5.4**.

<i>Excited State</i>	<i>Energy/nm(cm⁻¹)</i>	<i>Symmetry</i>	<i>Oscillator Strength</i>	<i>Contributions and Expansion Coefficients</i>
1	768(13021)	¹ B ₁	0.6456	H-1→L+1 -0.16366, H→L 0.69156
2	538(18587)	¹ B ₃	0.4136	H-1→L 0.66057, H→L+1 0.25024
3	367(27248)	¹ B ₃	1.8022	H-1→L -0.25666, H→L+1 0.66137
9	333(30030)	¹ B ₁	1.8591	H-1→L+1 0.68507, H→L 0.16842

The single electron HOMO to LUMO excitation dominates this band with the HOMO-1 to LUMO+1 single electron transition contributing weakly. The experimentally observed Q_x-band at ~515 nm correlates well with TDDFT-predicted excited state 2 occurring at 545 nm. A HOMO-1 to LUMO single electron transition dominates this excited state and is significantly complemented by a HOMO to LUMO+1 single electron excitation, as predicted by TDDFT. Significant splitting of the Soret band was also correctly predicted by TDDFT and was experimentally observed for **5.1-5.3**. As expected from Goutermann's model^{12,13}, two very strong transitions in the spectral region of excited states 3 and 9 were predicted by TDDFT. From TDDFT, excited state three occurs at 392 nm and is primarily composed of a single electron excitation from HOMO to LUMO+1 with small contributions from HOMO to LUMO+5 and HOMO-1 to LUMO excitations. Excited state nine is predicted at 362 nm and is largely comprised of the single electron contribution from HOMO-1 to LUMO+1 along with many low-magnitude single-electron excitations (Table 10). In general, the energies and intensities of all transitions were correctly predicted by TDDFT and could be described using Goutermann's four-orbital model with the exception of the slightly overestimated energy of the first excited state.

Nonetheless, this overestimation of about 1800 cm^{-1} falls within the range of expected error for TDDFT calculations of porphyrin, phthalocyanine, and similar extended π -systems^{67,126}.

Conclusions

This avenue of research has shown that the peripheral quaternized moieties of the water-soluble bacteriochlorins, which were formed upon quaternization of the nitrogen atom in free-base tetra-(3-pyridyl)bacteriochlorins, have negligible influence on their electronic structures. A split Soret band in the spectral region of 350-400 nm and large splitting between the Q_y - and Q_x -bands in the visible to NIR region were present in all bacteriochlorins studied. In the cases of **5.1-5.3**, the most important features of their experimental UV-vis and MCD spectra are explained by Goutermann's four-orbital model and were accurately predicted by the electronic structure calculations. The experimentally observed reversal of MCD sign sequence in the Vis-NIR spectral region correlates well with the DFT-predicted $\Delta\text{HOMO} < \Delta\text{LUMO}$ relationship. Also, correctly predicted by TDDFT, were the experimentally observed split Soret band and large splitting between the Q_y - and Q_x -bands. In general, the electronic structures and spectroscopy of these quaternized bacteriochlorins are nearly identical to those of earlier described *meso*-aryl bacteriochlorins.

Chapter 6: Summary of Electronic Structures of Core-Modified Porphyrins and Phthalocyanines

Throughout this thesis, the electronic structures of core-modified porphyrins and phthalocyanines were investigated. From structural manipulation, predictable electronic structure behaviours can be exploited to suit the needs of the designer, with the commonly possessed NIR-bands often being the focal point of study.

In chapter two, several oxochlorins were prepared and designed to mimic the physical structure of naturally occurring porphyrins and specifically, the chlorophylls. Two bacteriochlorins (**2.6** and **2.7**) were designed to combine the chlorophyll-like peripheral components with the previously successful (in terms of PDT application) bacteriochlorin scaffolding. The bacteriochlorin molecules were featured due to their strong absorbances in the NIR-region which were much more intense compared to the other studied oxochlorins.

The electronic structure analysis of these oxochlorins showed that all samples exhibited a $\Delta\text{HOMO} > \Delta\text{LUMO}$ relationship of their frontier π molecular orbitals which were of Goutermann's " a_{1u} ", " a_{2u} ", " b_{2g} ", and " b_{3g} " character and were comprised of the HOMO-1 to LUMO+1. All magnetic circular dichroism spectra showed a negative to positive MCD sign sequence, in terms of ascending energy, which was consistent with the DFT-predicted $\Delta\text{HOMO} > \Delta\text{LUMO}$ relationship. This $\Delta\text{HOMO} > \Delta\text{LUMO}$ relationship and MCD sign sequence is the opposite of those expected by naturally occurring porphyrin analogues. This very interesting result was rather unexpected and demonstrates that in the recreation of the electronic

structures of natural porphyrinoids, physical structure takes a backseat to electronic properties which can be manipulated with peripheral substitutions. Nonetheless, strong absorptions in the NIR region, which were well within the optical window of tissue, were observed for the bacteriochlorins **2.6** and **2.7** indicating a successful scaffolding on which to build.

Chapter three featured several hard chromophoric systems which were benzoannulated derivatives of tetraazaporphyrin. As the π -system was increased outwards via benzoannulation, the strongly absorbing λ_{\max} bands in the NIR region became increasingly red-shifted. A number of these metal-free samples, which were analyzed via electronic structure analysis, included electron donating groups at α -positions which were shown to further red-shift these λ_{\max} bands into the NIR region.

The computational focus of this project was to accurately and simultaneously predict (with TDDFT methods) the energies and splitting of the Q_x - and Q_y -bands, as well as the interligand charge transfer transitions region which was present in all the UV-vis spectra of the phthalocyanines and their derivatives which had been α -substituted with electron donating groups. The long-range corrected exchange correlation functionals (LC-wPBE and LC-BP86) provided the most accurate estimation of the energies of the Q_x - and Q_y -bands while the hybrid functionals modelled the ICT transitions region the best; however, neither of these modern approaches could accurately and simultaneously predict both of these spectral components.

The splitting (in terms of energy) of the Q_x - and Q_y -bands was the focal point of the investigation as previous authors and their work on similar systems had predicted that the splitting of the Q_x - and Q_y -components will decrease in a linear fashion with stepwise increase

in benzoannulation, collapse into a single band in the case of the naphthalocyanine (two benzoannulations) and remain collapsed for the anthracocyanine (three benzoannulations). The TDDFT calculations performed in this project show that there is a crossover point of the Q_x - and Q_y -band energies which occurs over the Nc and an inversion of the Q_x - and Q_y -bands in the case of the Ac.

In chapter four, bulky phthalocyanines were investigated in the form of octacarbazole-substituted zinc phthalocyanines. The peripheral bulk was enhanced with electron-donating and chromophoric carbazole groups which were further substituted with tBu groups to enhance solubility. The UV-vis and MCD spectra of both compounds showed very clear Faraday A-terms which were expected due to the higher degree of D_{4h} symmetry which was possessed by the molecules under study. Very broad interligand charge transfer transitions bands were observed between 450 and 550 nm which were derived from the transfer of electron density from the electron-donating carbazole groups to the electron-accepting zinc phthalocyanine core.

The electronic structure analysis of these systems uncovered a very strong electronic interaction of the carbazole groups as the TDDFT calculations predicted that Gouterman's four orbitals were of " a_{1u} ", " a_{2u} ", and " e_g " character and were comprised of the LUMO+1, LUMO, HOMO, and HOMO-25. DFT predicted that the HOMO-1 to the HOMO-24 have their electron density primarily situated over the carbazole groups. This result shows the strong interaction that the carbazole groups have with the phthalocyanine core, making for a very electronically interactive donor-acceptor system which could be used in photovoltaic applications.

Chapter five presented work on the electronic structure elucidation of bacteriochlorins which had been made water-soluble through the synthetic incorporation of cationic quaternary pyridinium moieties at the *meso*-positions of the bacteriochlorin core. Water-solubility is a critical structural feature which must be possessed by any potential photochemotherapeutic material as it must remain dissolved in the bloodstream which is considered an aqueous medium.

The electronic structures of these studied bacteriochlorin systems were similar to those found in naturally occurring porphyrinoids and also synthetic porphyrins which have been *meso*-substituted with aryl groups. The TDDFT calculations predicted a $\Delta\text{LUMO} > \Delta\text{HOMO}$ relationship of the frontier π molecular orbitals which was consistent with their positive to negative MCD spectral sign sequence in terms of ascending energy. There was a notable lack of spectral feature differences between the three bacteriochlorin samples and this was attributed to the negligible influence of the cationic arms on the electronic structure of these systems.

The TDDFT calculations predicted that the Goutermann's " a_{1u} ", " a_{2u} ", " b_{2g} ", and " b_{3g} " frontier π molecular orbitals were the HOMO-1 to LUMO+1 and they all featured electron density which was primarily situated over the bacteriochlorin core while no electron density was present over the cationic arms. Since Goutermann's four orbitals and the transitions that occur between them are responsible for nearly all of the spectral signals that are present in the optical absorption spectra, the fact that there is no electron density over the cationic arms correlates well with the lack of optical absorption spectral feature differences between the three studied bacteriochlorin samples.

The primary message that the electronic structure analysis in this thesis has demonstrated is that extension of the π -system outwards and incorporation of electron-donating groups at α -positions on porphyrin and phthalocyanine cores dramatically shifts their strongly absorbing bands, commonly possessed by these compounds, far into the NIR region (past 900 nm); however, these bulky compounds have poor solubility which is their major limiting structural flaw in terms of common applications. Peripheral and non-peripheral modification of porphyrins and phthalocyanines is currently the most commonly used canvas of photochemotherapeutic molecule design. Looking towards the future of photosensitizer design, water-soluble phthalocyanines, naphthalocyanines, and anthracocyanines should be seriously considered as synthetic targets for the advancement of photodynamic therapy photosensitizers.

References:

1. (a) Juzenas, P. *Trends Cancer Res.* **2005**, *1*, 93-110. (b) O'Riordan, K.; Akilov, O. E.; Hasan, T. *Photodiagn. Photodyn. Ther.* **2005**, *2*, 247-262.
2. (a) da Silva, R. N.; Cunha, A.; Tome, A. C. *Eur. J. Med. Chem.* **2018**, *154*, 60-67. (b) George, L.; Hiltunen, A.; Santala, V.; Efimov, A. *J. Inorg. Biochem.* **2018**, *183*, 94-100. (c) Sindelo, A.; Osifeko, O. L.; Nyokong, T. *Inorg. Chim. Acta* **2018**, *476*, 68-76.
3. (a) de la Torre, G.; Vazquez, P.; Agullo-Lopez, F.; Torres, T. *J. Mater. Chem.* **1998**, *8*, 1671-1683. (b) Chen, Y.; Hanack, M.; Blau, W. J.; Dini, D.; Liu, Y.; Lin, Y.; Bai, J. *J. Mater. Sci.* **2006**, *41*, 2169-2185. (c) Wrobel, D.; Dudkowiak, A. *Mol. Cryst. Liq. Cryst.* **2006**, *448*, 617-640.
4. Chen, M. J.; Fremgen, D. E.; Rathke, J. W. *J. Porphyrins Phthalocyanines.* **1998**, *2*, 473-482.
5. Owen, T. *Fundamentals of UV-visible spectroscopy: A Primer*, 1st ed.; Hewlett-Packard Company: Germany., 1996; p 40.
6. Nemykin, V. *Spectroscopic and Structural Methods in Inorganic Chemistry*, 2016.
7. Waluk, J.; Michl, J. *J. Org. Chem.* **1991**, *56*, 2729.
8. Michl, J. *J. Am. Chem. Soc.* **1978**, *100*, 6801.
9. Michl, J. *J. Am. Chem. Soc.* **1978**, *100*, 6812.
10. Michl, J. *J. Am. Chem. Soc.* **1978**, *100*, 6819.
11. Michl, J. *J. Am. Chem. Soc.* **1978**, *100*, 6824.
12. Gouterman, M. J. In *The Porphyrins*; Dolphin, D., Ed.; Academic Press: New York, 1978; Vol. III, pp 1-165.
13. (a) Seybold, P. G.; Gouterman, M. J. *Mol. Spectrosc.* 1969, *31*, 1-13. (b) Gouterman, M. *J. Mol. Spectrosc.* **1961**, *6*, 138-163.
14. Stillman, M. J.; Nyokong, T. *Phthalocyanines Properties and Applications*; Leznoff, C. C.; Lever, A. B. P., Ed.; VCH Publishers Inc: Weinheim, 1989; Vol. 1; p 133.
15. Rieger, P.H. *Electrochemistry*, 2nd ed.; Chapman & Hall: New York, NY., 1993; pgs 1-477.
16. Frisch, M. J.; Trucks, G. W.; Schlegel, H. B.; Scuseria, G. E.; Robb, M. A.; Cheeseman, J. R.; Scalmani, G.; Barone, V.; Mennucci, B.; Petersson, G. A.; et. al *Gaussian 09, Revision A.1*, Gaussian, Inc., Wallingford CT, 2009.
17. Dennington II, R. D.; Keith, T. A.; Milam, J. M. *GaussView 5.0*, SemiChem Inc. Wallingford CT, 2008.
18. McLean, A. D.; Chandler, G. S. *J. Chem. Phys.* **1980**, *72*, 5639-5648.
19. Ke, X. S.; Chang, Y.; Chen, J. G.; Tian, J.; Mack, J.; Cheng, X.; Shen, Z.; Zhang, J. L. *J. Am. Chem. Soc.* **2014**, *136*, 9598-9607.
20. Brückner, C.; Samankumara, L.; Ogikubo, J. Synthesis of Bacteriochlorins and Isobacteriochlorins. In *Handbook of Porphyrin Science*; World Scientific: River Edge, NY, 2012; Vol. 17; 1-112.
21. Baumler, W. In *Comprehensive Series in Photosciences (Vol. II)*; Elsevier, 2001; 83-98.

22. Chang, C.K.; *Biochemistry*. **1980**, 19, 1971-1976.
23. (a) Kobayashi, N.; Muranaka, A.; Mack, J. *Circular Dichroism and Magnetic Circular Dichroism Spectroscopy for Organic Chemists*; RSC: London, 2012; p 216. (b) Mason, W.R. *A practical Guide to Magnetic Circular Dichroism Spectroscopy*; John Wiley & Sons, Inc.: Hoboken, NJ, 2007; p 223.
24. Tao, J.; Perdew, J. P.; Staroverov, V. N.; Scuseria, G. E. *Phys. Rev. Lett.* **2003**, 91, 146401-146405.
25. Tenderholt, A. L. *QMForge, version 2.1*; Standord University: Stanford, CA, 2011.
26. Mack, J. *Chem. Rev.* **2017**, 117, 3444-3478.
27. Umetsu, M.; Wang, Z. Y.; Yoza, K.; Kobayashi, M.; Nozawa, T. *Biochim. Biophys. Acta.* **2000**, 1457, 106-117.
28. Umetsu, M.; Wang, Z. Y.; Kobayashi, M.; Nozawa, T. *Biochim. Biophys. Acta.* **1999**, 1410, 19-31.
29. Nonomura, Y.; Igarashi, S.; Yoshioka, N.; Inoue, H. *Chem. Phys.* **1997**, 220, 155-166.
30. Briat, B.; Schooley, D. A.; Records, R.; Bunnenberg, E.; Djerassi, C. *J. Am. Chem. Soc.* **1967**, 89(24), 6170-6177.
31. Keegan, J. D.; Stolzenberg, A. M.; Lu, Y. C.; Linder, R. E.; Barth, G.; Moscowitz, A.; Bunnenberg, E.; Djerassi, C. *J. Am. Chem. Soc.* **1982**, 104(16), 4305-4317.
32. Keegan, J. D.; Stolzenberg, A. M.; Lu, Y. C.; Linder, R. E.; Barth, G.; Moscowitz, A.; Bunnenberg, E.; Djerassi, C. *J. Am. Chem. Soc.* **1982**, 104(16), 4317-4329.
33. Keegan, J. D.; Stolzenberg, A. M.; Lu, Y. C.; Linder, R. E.; Barth, G.; Moscowitz, A.; Bunnenberg, E.; Djerassi, C. *J. Am. Chem. Soc.* **1981**, 103(11), 3201-3203.
34. Bracete, A. M.; Kadkhodayan, S.; Sono, M.; Huff, A. M.; Zhuang, C.; Cooper, D. K.; Smith, K. M.; Chang, C. K.; Dawson, J. H. *Inorg. Chem.* **1994**, 33, 5042-5049.
35. Huff, A. M.; Chang, C. K.; Cooper, D. K.; Smith, K. M.; Dawson, J. H. *Inorg. Chem.* **1993**, 32, 1460-1466.
36. Mack, J.; Asano, Y.; Kobayashi, N.; Stillman, M. J. *J. Am. Chem. Soc.* **2005**, 127, 17697-17711.
37. Huang, W. Y.; Wild, U. P. *J. Phys. Chem.* **1992**, 96, 6189-6195.
38. Menezes, J. C. J. M. D. S.; Faustino, M. A. F.; Oliveira, K. T. D.; Uliana, M. P.; Ferreira, V. F.; Hackbarth, S.; Roder, B.; Tasso, T. T.; Furuyama, T.; Kobayashi, N.; Silva, A. M. S.; Neves, M. G. P. M. S.; Cavaleiro, J. A. S. *Chem. Eur. J.* **2014**, 20, 13644-13655.
39. Rhoda, H.M.; Akhigbe, J.; Ogikubo, J.; Sabin, J. R.; Ziegler, C. J.; Bruckner, C.; Nemykin, V. N. *J. Phys. Chem. A.* **2016**, 120(29), 5805-5815.
40. (a) Krzywiecki, M.; Grzadziel, L.; Powroznik, P.; Kwoka, M.; Rechmann, J.; Erbe, A. *Phys. Chem. Chem. Phys.* **2018**, 20(23), 16092-16101. (b) Nar, I.; Atsay, A.; Altindal, A.; Hamuryudan, E.; Kocak, M. B.; Guel, A. *Chem. Eur. J.* **2018**, 24(27), 6946-6949. (c) Liang, Y.; Lv, W.; Luo, X.; He, L.; Xu, K.; Zhao, F.; Huang, F.; Lu, F.; Peng, Y. *Synth. Met.* **2018**, 240, 44-51.

41. (a) Ndiaye, A. L.; Delile, S.; Brunet, J.; Varenne, C.; Pauly, A. *Biosensors*. **2016**, 6(3), 46/1-46/12. (b) Sun, Q.; Feng, W.; Yang, P.; You, G.; Chen, Y. *New J. Chem.* **2018**, 42(9), 6713-6718.
42. (a) Elemans, J. A. A. W.; van Hameren, R.; Nolte, R. J. M.; Rowan, A. E. *Advanced Materials* **2006**, 18, 1251-1266. (b) Rao, C. N. R.; Govindaraj, A. *Acc. Chem. Res.* **2002**, 35, 998-1007.
43. Leznoff, C. C.; Lever, A. B. P., Eds. *Phthalocyanines: Properties and Applications*; VCH Publishers: New York, 1990-1996; Vol. 1-4.
44. Kobayashi, N.; Nakajima, S.; Ogata, H.; Fukuda, T. *Chem. Eur. J.* **2004**, 10, 6294-6312.
45. Fukuda, R.; Ehara, M.; Nakatsuji. *J. Chem. Phys.* **2010**, 133, 144316.
46. Somashekarappa, M. P.; Keshavayya, J.; Sherigara, B. S. *Spectrochim. Acta, Part A.* **2003**, 59A(4), 883-893.
47. Zhong, A.; Zhang, Y.; Bian, Y. *J. Mol. Graphics Modell.* **2010**, 29, 470-480.
48. Kobayashi, N.; Sasaki, N.; Higashi, Y.; Osa, T. *Inorg. Chem.* **1995**, 34, 1636-1637.
49. Kobayashi, N.; Ogata, H.; Nonaka, N.; Luk'yanets, E. A. *Chem. Eur. J.* **2003**, 9, 5123-5134.
50. Yamamoto, S.; Kuribayashi, K.; Murakami, T. N.; Kwon, E.; Stillman, M. J.; Kobayashi, N.; Segawa, H.; Kimura, M. *Chem. Eur. J.* **2017**, 23, 15446-15454.
51. Freyer, W.; Neacsu, C. C.; Raschke, M. B. *J. Lumin.* **2008**, 128, 661-672.
52. Bedworth, P. V.; Perry, J. W.; Marder, S. R. *Chem. Comm.* **1997**, 15, 1353-1354.
53. Christie, R. M. *Dyes Pigments.* **1995**, 27(1), 35-43.
54. (a) Zhang, L.; Qi, D.; Zhao, L.; Bian, Y.; Li, W. *J. Mol. Graphics Modell.* **2012**, 35, 57-65. (b) Baerends, E. J.; Ricciardi, G.; Rosa, A.; van Gisbergen, S. J. A. *Coord. Chem. Rev.* **2002**, 230, 5-27.
55. Majeed, S. A.; Ghazal, B.; Nevenon, D. E.; Goff, P. C.; Blank, D. A.; Nemykin, V. N.; Makhseed, S. *Inorg. Chem.* **2017**, 56, 11640-11653.
56. Armarego, W. L. F.; Perrin, D. D. *Purification of Laboratory Chemicals*; Reed Educational and Professional Publishing: Oxford, 1996, pp 1-544.
57. Cook, M. J.; Dunn, A. J.; Howe, S. D.; Thomson, A. J. *J. Chem. Soc., Perkin Trans. 1.* **1988**, 1, 2453-2458.
58. Galinato, M. G. I.; Spolidak, T.; Ballou, D. P.; Lehnert, N. *Biochemistry* **2011**, 50, 1053-1069.
59. Frisch, M. J.; Trucks, G. W.; Schlegel, H. B.; Scuseria, G. E.; Robb, M. A.; Cheeseman, J. R.; Montgomery, Jr., J. A.; Vreven, T.; Kudin, K. N.; Burant, J. C.; Millam, J. M.; Iyengar, S. S.; Tomasi, J.; Barone, V.; Mennucci, B.; Cossi, M.; Scalmani, G.; Rega, N.; Petersson, G. A.; Nakatsuji, H.; Hada, M.; Ehara, M.; Toyota, K.; Fukuda, R.; Hasegawa, J.; Ishida, M.; Nakajima, T.; Honda, Y.; Kitao, O.; Nakai, H.; Klene, M.; Li, X.; Knox, J. E.; Hratchian, H. P.; Cross, J. B.; Bakken, V.; Adamo, C.; Jaramillo, J.; Gomperts, R.; Stratmann, R. E.; Yazyev, O.; Austin, A. J.; Cammi, R.; Pomelli, C.; Ochterski, J. W.; Ayala, P. Y.; Morokuma,

- K.; Voth, G. A.; Salvador, P.; Dannenberg, J. J.; Zakrzewski, V. G.; Dapprich, S.; Daniels, A. D.; Strain, M. C.; Farkas, O.; Malick, D. K.; Rabuck, A. D.; Raghavachari, K.; Foresman, J. B.; Ortiz, J. V.; Cui, Q.; Baboul, A. G.; Clifford, S.; Cioslowski, J.; Stefanov, B. B.; Liu, G.; Liashenko, A.; Piskorz, P.; Komaromi, I.; Martin, R. L.; Fox, D. J.; Keith, T.; Al-Laham, M. A.; Peng, C. Y.; Nanayakkara, A.; Challacombe, M.; Gill, P. M. W.; Johnson, B.; Chen, W.; Wong, M. W.; Gonzalez, C.; and Pople, J. A.; *Gaussian 03, Revision C.02*, Gaussian, Inc., Wallingford CT, 2004.
60. Hay, P. J.; Wadt, W. R. *J. Chem. Phys.* **1985**, *82*, 270-83.
61. Nemykin, V. N.; Basu, P. VModes: Virtual Molecular Orbital description program for Gaussian, GAMESS, and HyperChem, Revision A 7.2; A8.1 University of Minnesota, Duluth, MN, 2003-2010.
62. Freyer, W.; Mueller, S.; Teuchner, K. *J. Photochem. Photobiol., A* **2004**, *163*, 231-240.
63. Chen, Y.; Fang, W.; Wang, K.; Liu, W.; Jiang, J. *Inorg. Chem.* **2016**, *55*, 9289-9296.
64. Sakamoto, K.; Yoshino, S.; Takemoto, M.; Furuya, N. *J. Porphyrins Phthalocyanines*. **2013**, *17*, 605-627.
65. Ghosh, A. *Acc. Chem. Res.* **1998**, *31*, 189-198.
66. (a) Novakova, V.; Reimerova, P.; Svec, J.; Suchan, D.; Miletin, M.; Rhoda, H. M.; Nemykin, V. N.; Zimcik, P. *Dalton Trans.* **2015**, *44*(29), 13220-13233. (b) Nemykin, V. N.; Hadt, R. G. *J. Phys. Chem.* **2010**, *114*(45), 12062-12066.
67. Nemykin, V. N.; Hadt, R. G.; Belosludov, R. V.; Mizuseki, H.; Kawazoe, Y. *J. Phys. Chem. A* **2007**, *111*(50), 12901-12913.
68. Nyokong, T.; Antunes, E. In *Handbook of Porphyrin Science (Vol. 7)*; World Scientific, 2010; 247-357.
69. (a) Makhseed, S.; Samuel, J.; Ibrahim, F. *Tetrahedron*. **2008**, *64* (37), 8871-8877; (b) Makhseed, S.; Ghazal, B.; Abdelmoniem, A. M.; Novakova, V.; Zimcik, P. *RSC Adv.* **2015**, *5* (72), 58854-58864; (c) Rajput, C. S.; Singhal, S. *J. Pharm.* **2013**, *2013*, 907525.
70. (a) Zhang, F.-F.; Gan, L.-L.; Zhou, C.-H. *Bioorg. Med. Chem. Lett.* **2010**, *20* (6), 1881-1884; (b) Guo, S.; Tipparaju, S. K.; Pegan, S. D.; Wan, B.; Mo, S.; Orjala, J.; Mesecar, A. D.; Franzblau, S. G.; Kozikowski, A. P. *Bioorg. Med. Chem.* **2009**, *17* (20), 7126-7130; (c) Maneerat, W.; Phakhodee, W.; Ritthiwigrom, T.; Cheenpracha, S.; Promgool, T.; Yossathera, K.; Deachathai, S.; Laphookhieo, S. *Fitoterapia*. **2012**, *83* (6), 1110-1114.
71. (a) de la Torre, G.; Vazquez, P.; Agullo-Lopez, F.; Torres, T. *Chem. Rev.* **2004**, *104* (9), 3723-50; (b) Vagin, S.; Barthel, M.; Dini, D.; Hanack, M. *Inorg. Chem.* **2003**, *42* (8), 2683-94; (c) Emmelius, M.; Pawlowski, G.; Vollmann, H. W. *Angew. Chem., Int. Ed. Engl.* **1989**, *28* (11), 1445-1471; (d) K. Nazeeruddin, M.; Humphry-Baker, R.; Gratzel, M.; A. Murrer, B. *Chem. Comm.* **1998**, (6), 719-720; (e) Groothues, H.; Kremer, F.; Schouten, P. G.; Warman, J. M. *Adv. Mater.* **1995**, *7* (3), 283-286; (f) Ohmori, M.; Uno, T.; Nakatani, M.; Nakano, C.; Fujii, A.; Ozaki, M. *Appl. Phys. Lett.* **2016**, *109* (15), 153302; (g) Chauhan, S. M. S.; Kumar, A.; Srinivas, K. A. *Chem. Comm.* **2003**, (18), 2348-2349; (h) Asahi, T.; Yoshikawa, H. Y.; Yashiro, M.; Masuhara, H. *Appl. Surf. Sci.* **2002**, *197-198*, 777-781; (i) Zimcik, P.; Miletin, M.; Ponec, J.; Kostka, M.; Fiedler, Z. *J. Photochem. Photobiol., A* **2003**, *155* (1-3), 127-131; (j) Agostinis, P.; Berg, K.; Cengel, K. A.; Foster, T. H.; Girotti, A. W.; Gollnick, S. O.; Hahn, S. M.; Hamblin, M. R.; Juzeniene, A.; Kessel, D.; Korbelik, M.; Moan,

- J.; Mroz, P.; Nowis, D.; Piette, J.; Wilson, B. C.; Golab, J. *Ca-Cancer J. Clin.* **2011**, *61* (4), 250-281; (k) Tuhl, A.; Makhseed, S.; Zimcik, P.; Al-Awadi, N.; Novakova, V.; Samuel, J. *J. Porphyrins. Phthalocyanines.* **2012**, *16*, 817-825.
72. Isago, H. *Optical Spectra of Phthalocyanines and Related Compounds*; Springer: Japan, 2015.
73. Ough, E. A.; Stillman, M. J.; Creber, K. A. M. *Can. J. Chem.* **1993**, *71* (11), 1898-1909.
74. Makhseed, S.; Machacek, M.; Alfadly, W.; Tuhl, A.; Vinodh, M.; Simunek, T.; Novakova, V.; Kubat, P.; Rudolf, E.; Zimcik, P. *Chem. Comm.* **2013**, 49(95), 11149-11151.
75. Sabin, J. R.; Varzatskii, O. A.; Voloshin, Y. Z.; Starikova, Z. A.; Novikov, V. V.; Nemykin, V. N. *Inorg. Chem.* **2012**, *51* (15), 8362-8372.
76. Bottari, G.; Kahnt, A.; Guldi, D. M.; Torres, T. *ECS J. Solid State Sci. Technol.* **2013**, *2* (10), M3145-M3150.
77. Bottari, G.; Kahnt, A.; Guldi, D. M.; Torres, T. *ECS J. Solid State Sci. Technol.* **2013**, *2*(10), M3145-M3150.
78. Pandit, P.; Yamamoto, K.; Nakamura, T.; Nishimura, K.; Kurashige, Y.; Yanai, T.; Nakamura, G.; Masaoka, S.; Furukawa, K.; Yakiyama, Y.; Kawano, M.; Higashibayashi, S. *Chem. Sci.* **2015**, *6*(7), 4160-4173.
79. Safonova, E. A.; Martynov, A. G.; Nefedov, S. E.; Kirakosyan, G. A.; Gorbunova, Y. G.; Tsvadze, A. Y. A. *Inorg. Chem.* **2016**, *55*(5), 2450-2459.
80. Ayhan, M. M.; Altinbas-Ozpinar, G.; Durmus, M.; Gurek, A. G. *Dalton Trans.* **2013**, 42(41), 14892-14904.
81. (a) Rosa, A.; Ricciardi, G. *Can. J. Chem.* **2009**, *87* (7), 994-1005; (b) Mack, J.; Kobayashi, N.; Stillman, M. J. *J. Porphyrins. Phthalocyanines.* **2006**, *10* (10), 1219-1237.
82. Dudkin, S. V.; Makarova, E. A.; Slivka, L. K.; Lukyanets, E. A. *J. Porphyrins Phthalocyanines.* **2014**, *18*, 107-114.
83. Morgan, A. R. In *Photodynamic Therapy: Basic Principles and Clinical Applications*, Marcel Dekker Inc., NY, 1992; 157-172.
84. Bonnett, R. In *Chemical Aspects of Photodynamic Therapy*, Gordon and Science Publisher, Amsterdam, 2000; 177-198.
85. Mironov, A. F. In *Advances in Porphyrin Chemistry*, The Scientific Research Institute of Chemistry, St-Petersburg University, St-Petersburg, 2004; Vol. 4; 271-292.
86. Chen, Y.; Li, G.; Pandey, R. K. *Curr. Org. Chem.* **2004**, *8*, 1105-1134.
87. Wainwright, M. In *Photosensitizers in Biomedicine*, John Wiley & Sons Ltd, Oxford, 2009; 113-146.
88. Ali, H.; van Lier, J. E. In *Handbook of Porphyrin Science: With Applications to Chemistry, Physics, Materials Science, Engineering, Biology, and Medicine*, World Scientific Publishing, Singapore, 2010; Vol. 2; 1-119.
89. Huang, L.; Huang, Y. Y.; Mroz, P.; Tegos, G. P.; Zhiyentayev, T.; Sharma, S. K.; Lu, Z.; Balasubramanian, T.; Kraymer, M.; Ruzie, C.; Yang, E.; Kee, H. L.; Kirmaier, C.; Diers, J. R.; Bocian, D. F.; Holten, D.; Lindsey, J. S.; Hamblin, M. R. *Anitmicrob. Agents Chemother.* **2010**, *54*, 3834-3841.
90. Kim, H. J.; Lindsey, J. S. *J. Org. Chem.* **2005**, *70*, 5475-5486.
91. Borbas, K. E.; Ruzie, C.; Lindsey, J. S. *Org. Lett.* **2008**, *10*, 1931-1934.

92. Ruzie, C.; Krayner, M.; Balasubramanian, T.; Lindsey, J. S. *J. Org. Chem.* **2008**, *73*, 5806-5820.
93. Krayner, M.; Ptaszek, M.; Kim, H. J.; Meneely, K. R.; Fan, D. Secor, K.; Lindsey, J. S. *J. Org. Chem.* **2010**, *75*, 1016-1039.
94. Krayner, M.; Yang, E. K.; Diers, J. R.; Bocian, D. F.; Holten, D.; Lindsey, J. S. *New J. Chem.* **2011**, *35*, 587-601.
95. Mass, O.; Lindsey, J. S. *J. Org. Chem.* **2011**, *76*, 9478-9487.
96. Cavaleiro, J. A. S.; Neves, M. G. P. M. S.; Tome, A. C. *ARKIVOC.* **2003**, *14*, 107-130.
97. Cavaleiro, J. A. S.; Tome, A. C.; Neves, M. G. P. M. S. In *Handbook of Porphyrin Science: With Applications to Chemistry, Physics, Materials Science, Engineering, Biology, and Medicine*, World Scientific Publishing, Singapore, 2010; Vol. 2; 193-294.
98. Chang, C. K.; Sotiriou, C. *J. Org. Chem.* **1985**, *50*, 4989-4991.
99. Bonnett, R.; Nizhnik, A. N.; Berenbaum, M. C. *J. Chem. Soc., Chem. Comm.* **1989**, 1822-1823.
100. Brückner, C.; Dolphin, D. *Tetrahedron Lett.* **1995**, *36*, 3295-3298.
101. Brückner, C.; Dolphin, D. *Tetrahedron Lett.* **1995**, *36*, 9425-9428.
102. Samankumara, L. P.; Zeller, M.; Krause, J. A.; Brückner, C. *Org. Biomol. Chem.* **2010**, *8*, 1951-1965.
103. Hyland, M. A.; Morton, M. D.; Brückner, C. *J. Org. Chem.* **2012**, *77*, 3038-3048.
104. Whitlock, H. W. Jr.; Hanauer, R.; Oester, M. Y.; Bover, B. K. *J. Am. Chem. Soc.* **1969**, *91*, 7485-7489.
105. Pineiro, M. d' A.; Rocha Gonsalves, A. M.; Pereira, M. M.; Formosinho, S. J.; Arnaut, L. G. *J. Phys. Chem. A*, **2002**, *106*, 3787-3795.
106. Pereira, M. M.; Monteiro, C. J. P.; Simoes, A. V. C.; Pinto, S. M. A.; Arnaut, L. G.; Sa, G. F. F.; Silva, E. F. F.; Rocha, L. B.; Simoes, S.; Formosinho, S. J.; *J. Porphyrins. Phthalocyanines.* **2009**, *13*, 567-573.
107. Dabrowski, J. M.; Arnaut, L. G.; Pereira, M. M.; Monteiro, C. J. P.; Urbanska, K.; Simoes, S.; Stochel, G. *ChemMedChem.* **2010**, *5*, 1970-1980.
108. Pereira, M. M.; Monteiro, C. J. P.; Simoes, A. V. P.; Pinto, S. M. A.; Abreu, A. R.; Sa, G. F. F.; Silva, E. F. F.; Rocha, L. B.; Dabrowski, J. M.; Formosinho, S. J.; Simoes, S.; Arnaut, L. G. *Tetrahedron.* **2010**, *66*, 9545-9551.
109. Nascimento, B. F. O.; Rocha, d' A.; Gonsalves, M.; Pineiro, M. *Inorg. Chem. Comm.* **2010**, *13*, 395-398.
110. Pereira, M. M.; Abreu, A. R.; Goncalves, N. P. F.; Calvete, M. J. F.; Simoes, A. V. C.; Monteiro, C. J. P.; Arnaut, L. G.; Eusebio, M. E.; Canotilho, J. *Green Chem.* **2012**, *14*, 1666-1672.
111. Dorough, G. D.; Miller, J. R. *J. Am. Chem. Soc.* **1952**, *74*, 6106-6108.
112. Inhoffen, H. H.; Buchler, J. W.; Thomas, R. *Tetrahedron Lett.* **1969**, *10*, 1141-1144.
113. Schastak, S.; Shulga, A.; Berr, F.; Wiedemann, P. *US Patent* 6410568. **2002**.
114. Oertel, M.; Schastak, S. I.; Tannapfel, A.; Hermann, R.; Sack, U.; Mössner, J.; Berr, F. *J. Photochem. Photobiol., B.* **2003**, *71*, 1-10.
115. Schastak, S.; Jean, B.; Handzel, R.; Kostenich, G.; Hermann, R.; Sack, U.; Orenstein, A.; Wang, Y.; Wiedemann, P. *J. Photochem. Photobiol. B.*, **2005**, *78*, 203-213.

116. Schastak, S.; Yafai, Y.; Geyer, W.; Kostenich, G.; Orenstein, A.; Wiedemann, P. *Methods Find. Exp. Clin. Pharmacol.* **2008**, 30, 17-23.
117. Dabrowski, J. M.; Urbanska, K.; Arnaut, L. G.; Pereira, M. M.; Abreu, A. R.; Simoes, S.; Stochel, G. *ChemMedChem.* **2011**, 6, 465-475.
118. Schastak, S.; Gitter, B.; Handzel, R.; Hermann, R.; Wiedemann, P. *Methods Find. Exp. Clin. Pharmacol.* **2008**, 30, 129-133.
119. Schastak, S.; Ziganshyna, S.; Gitter, B.; Wiedemann, P.; Claudepierre, T. *PLoS One.* **2010**, 5: e11674.
120. Bonnet, R. In *Comprehensive Coordination Chemistry II*; Elsevier: Amsterdam, 2003; Vol. 9; 945-1005.
121. Yerushalmi, R.; Ashur, I.; Scherz, A. In *Chlorophylls and Bacteriochlorophylls: Biochemistry, Biophysics, Function and Applications*; Springer: Dordrecht, 2006; 495-506.
122. Pavani, C.; Uchoa, A. F.; Oliveira, C. S.; Yammamoto, Y.; Babtista, M. S. *Photochem. Photobiol. Sci.* **2009**, 8, 233-240.
123. Scherz, A.; Salomon, Y.; Brandis, A.; Scheer, H. *US Patent.* 6569846, **2003**.
124. Nevonen, D. N.; Kaesmann, E.; Li, R.; Bruckner, C.; Nemykin, V. N. (*In Preparation*). **2018**.
125. Fukuda, T.; Makarova, E. A.; Luk'yanets, E. A.; Kobayashi, N. *Chem. Eur. J.* **2004**, 10, 117-133.
126. Gao, Y.; Nemykin, V. N. *J. Mol. Graph. Model.* **2013**, 42, 73-80.